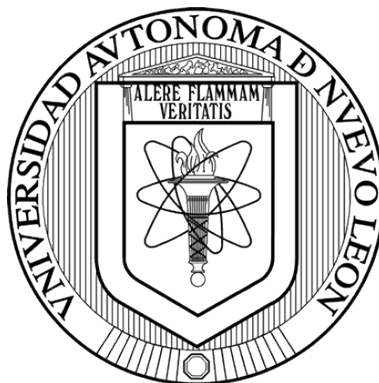# UNIVERSIDAD AUTÓNOMA DE NUEVO LEÓN

FACULTAD DE CIENCIAS QUÍMICAS

DYE SENSITIZED SOLAR CELLS BASED ON ZnO NANOFLOWERS AND TiO$_2$: EFFICIENCY ENHANCEMENT BY GOLD NANOSPHERES

Por

SUSANA BORBÓN ROJAS

**Como requisito parcial para obtener el Grado de
MAESTRÍA EN CIENCIAS con Orientación en
Química de los Materiales**

Agosto, 2019

DYE SENSITIZED SOLAR CELLS BASED ON ZnO NANOFLOWERS AND

TiO$_2$: EFFICIENCY ENHANCEMENT BY GOLD NANOSPHERES

Aprobación de la Tesis:

Dr. Israel Alejandro López Hernández
Presidente

Dr. Alejandro Vázquez Dimas
Secretario

Dra. Nora Aleyda García Gómez
Vocal

DRA. MA. ARACELI HERNÁNDEZ RAMÍREZ
Sub-Directora de Posgrado

DYE SENSITIZED SOLAR CELLS BASED ON ZnO NANOFLOWERS AND

TiO$_2$: EFFICIENCY ENHANCEMENT BY GOLD NANOSPHERES

Revisión de la Tesis:

Dra. Shadai Lugo Loredo
Co-directora

Dra. Nora Aleyda García Gómez
Tutor 1

Dr. Alejandro Vázquez Dimas
Tutor 2

Dra. Yolanda Peña Méndez
Tutor 3

DRA. MA. ARACELI HERNÁNDEZ RAMÍREZ
Sub-Directora de Posgrado

RESUMEN

Susana Borbón Rojas   Fecha de graduación: Agosto, 2019

Universidad Autónoma de Nuevo León

Facultad de Ciencias Químicas

Título de la tesis: DYE SENSITIZED SOLAR CELLS BASED ON ZnO NANOFLOWERS AND TiO$_2$: EFFICIENCY ENHANCEMENT BY GOLD NANOSPHERES

Número de páginas: 101   Candidato para el título de Maestro en Ciencias con Orientación en Química de los Materiales

Área de estudio: Materiales Funcionales

Propósito y método del estudio: Para obtener mejores celdas solares sensibilizadas con colorante (DSSC) es de interés el fusionar las propiedades del TiO$_2$ y el ZnO para su uso como fotoánodo. En este trabajo se reporta el aumento en el voltaje de circuito abierto (V$_{OC}$) de una DSSC con un electrodo compuesto por nanopartículas de TiO$_2$ y nanoflores de ZnO sintetizadas por método hidrotermal. Además, para incrementar la densidad de corriente (J$_{SC}$) fueron incorporadas nanopartículas de Au. Las DSSC fueron caracterizadas por la obtención de sus curvas corriente-potencial y espectroscopías de impedancia electroquímica y de fotovoltaje y fotocorriente moduladas en intensidad.

Contribuciones y conclusiones: Se desarrolló una ruta hidrotermal para la síntesis de nanoflores de ZnO sin el uso de aditivos en tiempos de reacción cortos. Las mejores DSSC obtuvieron una eficiencia de conversión de energía de 2.79% con un V$_{OC}$ de 886 mV.

Firma del Asesor:_____

iv

ABSTRACT

Susana Borbón Rojas   Graduation date: August, 2019

Universidad Autónoma de Nuevo León

Facultad de Ciencias Químicas

Title of the study: DYE SENSITIZED SOLAR CELLS BASED ON ZnO NANOFLOWERS AND TiO$_2$: EFFICIENCY ENHANCEMENT BY GOLD NANOSPHERES

Number of pages: 101   Candidate to the degree of Master of Science in Materials Chemistry

Area of study: Functional Materials

Purpose and method of the study: To obtain improved dye-sensitized solar cells (DSSC) is of interest to fuse the properties of TiO$_2$ and ZnO for its use as a photoanode. In this work is reported the enhancement of the open circuit voltage (V$_{OC}$) of a DSSC with an electrode composed by TiO$_2$ nanoparticles and hydrothermally synthesized ZnO nanoflowers. In addition, to further increase the short circuit current (J$_{SC}$) we incorporated Au nanoparticles. The DSSC were characterized by the obtention of its current-voltage curves, electrochemical impedance and light intensity modulated photocurrent and photovoltage spectroscopies.

Contributions and conclusions: It was developed a hydrothermal route for the synthesis of ZnO nanoflowers without the use of additives in short reaction times. The best DSSC achieved an efficiency of 2.79% with a V$_{OC}$ of 886 mV.

Advisor's signature:_____

ACKNOWLEDGMENTS

CONTENT TABLE

LIST OF TABLES

LIST OF FIGURES

NOMENCLATURE

5Z-95T	DSSC with an electrode composed of 5% of ZnO nanoflowers and 95% of TiO$_2$ nanoparticles
10Z-90T	DSSC with an electrode composed of 10% of ZnO nanoflowers and 90% of TiO$_2$ nanoparticles
15Z-85T	DSSC with an electrode composed of 15% of ZnO nanoflowers and 85% of TiO$_2$ nanoparticles
12A	ZnO nanoflowers decorated with 12,016 parts per million of Au nanoparticles
10A	ZnO nanoflowers decorated with 10,991 parts per million of Au nanoparticles
8A	ZnO nanoflowers decorated with 8,366 parts per million of Au nanoparticles
A	Active area
A.M.	Air Mass
a.u.	Arbitrary units
AC	Alternating current
ALD	Atomic layer deposition
C_μ	Chemical capacitance
DC	Direct current
D_n	Chemical diffusion coefficient
DRS	Diffuse reflectance spectroscopy
DSSC	Dye sensitized solar cell
Ec	Inferior limit of the conduction band

EDS	Energy dispersive spectroscopy
Eg	Bang gap (eV)
EIS	Electrochemical impedance spectroscopy
Ev	Superior limit of the valence band
FE-SEM	Field emission scanning electron microscopy
FF	Fill factor
FT-IR	Fourier transformed infrared spectroscopy
FTO	Fluorine-doped tin oxide
ICP-AES	Inductively coupled plasma atomic emission spectroscopy
IMPS	Intensity modulated photocurrent spectroscopy
IMVS	Intensity modulated photovoltage spectroscopy
ITO	Indium tin oxide
J-V	Current voltage
J	Current density (mA cm^{-2})
J_{max}	Maximum current density (mA cm^{-2})
J_{SC}	Short circuit current density (mA cm^{-2})
K	Dimensionless shape factor
Ksp	Solubility product constant
LABE	Low angle backscattered electron
LED	Light emitting diode
LSPR	Localized surface plasmon resonance
LUMO	Lowest unoccupied molecular orbital
PCE	Power conversion efficiency

P_{max}	Maximum power (W)
P_{sun}	Light intensity per unit area (mW cm^{-2})
QDSSC	Quantum dot sensitized solar cell
R	Reflectance
R_{CT}	Recombination resistance (Ω)
R_d	Diffusion impedance in the electrolyte
Rpm	Revolutions per minute
R_{Pt}	Transfer resistance in the counter electrode (Ω)
R_{rec}	Recombination resistance at the interface of the semiconductor, the electrolyte and the chemical capacitance (Ω)
R_s	Conductive substrate resistance (Ω)
SPR	Surface plasmon resonance
T	DSSC with an electrode composed of 100% of TiO$_2$ nanoparticles
$T_{1/2}$	Electron lifetime (s)
UV-Vis	Ultraviolet-visible
V	Voltage (mV)
V_{OC}	Open circuit voltage (mV)
XRD	X-ray diffraction
β	Light broadening at half the maximum intensity
θ	Bragg angle
λ	Wavelength (nm)
τ	Crystallite size

CHAPTER 1

INTRODUCTION

One of the major challenges' mankind must cope within this century is the transition from the use of non-renewable resources, principally fossil fuels, to the use of renewable energy while supplying the current energy demand.

Renewable energies originate from sources that are constantly replenished by nature. Among these sources we can name wind energy, geothermal energy, hydroelectric power and solar radiation, being the former the most auspicious. Solar radiation is the most abundant of the mentioned, being that 174,000 TW are provided yearly to the Earth [1], and the fact that its use does not produce emissions. Furthermore, Mexico is geographically located between latitudes 14° N and 33° N, this means it is within one of the most favorable four sunbelts according to worldwide intensity, which gives solar radiation levels of 5.35 kW h/m^2 [2].

1.1 Photovoltaic Cells

To help us to convert the solar radiation into electric energy, researchers have developed photovoltaic cells. A photovoltaic cell, also known as solar cell, is an

electrical device based on the photovoltaic effect which transforms sunlight into electricity [3].

To date, three generation of solar cells have been developed. First generation solar cells, based on crystalline silicon, although being expensive to fabricate are still the most commercially available, this is due to its high efficiency, which have reached values over 26% [4]. The second generation consists of thin film solar cells based on amorphous and hybrid silicon, cadmium telluride (CdTe), gallium arsenide (GaAs) or copper indium-gallium selenide (CIGS), being its major drawback their toxicity as well as their complex fabrication process [5]. The third generation can be subclassified in solar cells based on organic macromolecules, inorganic nanoparticles and hybrids [1]. Among the subclassification of solar cells based on inorganic nanoparticles the most popular are dye-sensitized solar cells (DSSC), quantum dot-sensitized solar cells (QDSSC) and perovskite solar cells, each of these having its own advantages and disadvantages [3]. In Figure 1 it is presented a scheme showing where the DSSC are located among the solar cells' generations. Among the advantages of DSSC are its simple structure, its inexpensive production, the fact that they are highly efficient even under diffuse light and they can be assembled on flexible substrates [1-6].
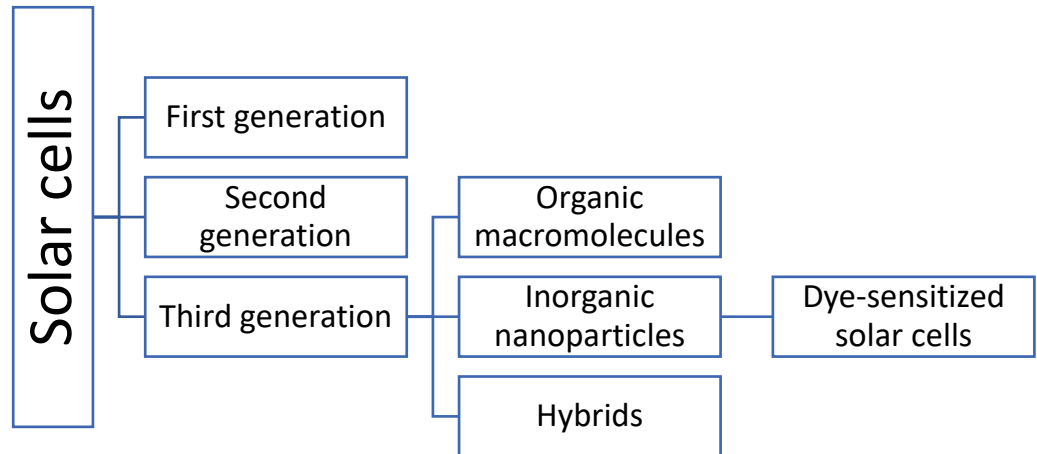
Figure 1. Scheme of solar cells generations.

1.2 Dye-sensitized Solar Cells (DSSC)

DSSC constitute a photoelectrochemical system, hence its principle, inspired by the phenomenon of photosynthesis, is different to the traditional silicon-based solar cell which has its basis on the photoelectrical effect. A traditional DSSC (Fig. 2) has the following components; a transparent conductive glass substrate, a photoanode composed by semiconductor nanoparticles, a monolayer of dye, an electrolyte and a counter electrode with a catalyst [7].

1.2.1 Transparent conductive glass substrates

Transparent conductive oxide substrates used in DSSC, must have low electrical resistivity and high transparency in visible spectral region to allow the flow of electrons [8]. The most used in DSSC are indium doped tin oxide (ITO) and fluorine doped tin oxide (FTO), each of them with specific parameters. ITO has a

transmittance of 80% and sheet resistance of 18 Ω/cm^2, while FTO has 75% and 8.5 Ω/cm^2 respectively. It is also noteworthy that throughout the sintering process the sheet resistance of FTO remains constant while ITO's increases substantially [9].

1.2.2 Photoanode

The purpose of the photoanode is to support the dye molecules and receive the photogenerated electrons from the excited dye. An optimal photoanode or electron transport layer, besides considering its economic and environmental factors, should have high surface area to boost dye loading, be transparent to visible light to evade photon loss to the substrate, possess a conduction band minor to the lowest unoccupied molecular orbital (LUMO) of the sensitizer, have high electron mobility, be inert to the redox electrolyte and possess hydroxyl groups or defects to chemisorb dye molecules [10].

1.2.3 Sensitizers

The mechanism of DSSC is based on the sensitization of wide band gap semiconductor using the dye molecules [11]. Therefore, to absorb photons, it is necessary to use dyes (sensitizers) with broad absorption spectra.

Various inorganic and organic dyes have been employed as sensitizers in DSSC, including metal complex dyes produced from heavy transition metals, due to its efficient metal-to-ligand charge transfer spectra, long excited lifetime and high redox properties [12]. The most studied metal complex dyes are polypyridyl

ruthenium dyes, from which the most used in DSSC are cis-di(thiocyanato)-bis(4,40-dicarboxy-2,20-bipyridine)-Ru(II) known as N3, cis-bis(isothiocyanato)bis(2,2′-bipyridyl-4,4′-dicarboxylato)-ruthenium(II) bis-tetrabutylammonium known as N719, and tri-thiocyanato-4,40,400-tricarboxy-2,20:60,200-terpyridine)-Ru(II) known as N749. DSSC having a ruthenium-based sensitizer have yielded a power conversion efficiency (PCE) value of 11.9% [13].

1.2.4   Electrolyte

The electrolyte is the compound that provides ionic conductivity between the electrodes in an electrochemical device, it functions as the medium for transportation of charge carriers in the form of ions. In a DSSC, the interaction between the electrolyte and the electrode will affect its photovoltaic parameters, consequently determining its efficiency. In addition, the electrolyte regenerates the dye during the DSSC operation.

To be used in a DSSC, an electrolyte must be able to transport the charge carriers between the photoanode and counter electrode, guarantee fast diffusion of charge carriers (high conductivity) and have long-term stability. Electrolytes used in DSSC can be classified in three categories; liquid, quasi-solid and solid conductors [1]. The most used liquid electrolyte is iodide/triiodide (I^-/I_3^-), because of its kinetic properties, excellent infiltration, relative high stability, low-cost and easy preparation [6].

1.2.5 Counter Electrode

The task of the counter electrode in a DSSC is to gather electrons from the external circuit and to catalyze the reduction of the electrolyte. It should have low resistance and high electrocatalytic activity for I^-/I_3^- redox reaction to decrease overvoltage and charge recombination [14].

The most common counter electrode in DSSC is a Pt-coated FTO, because of its high electrical conductivity, catalytic activity towards I^-/I_3^- and high reflecting properties [15].
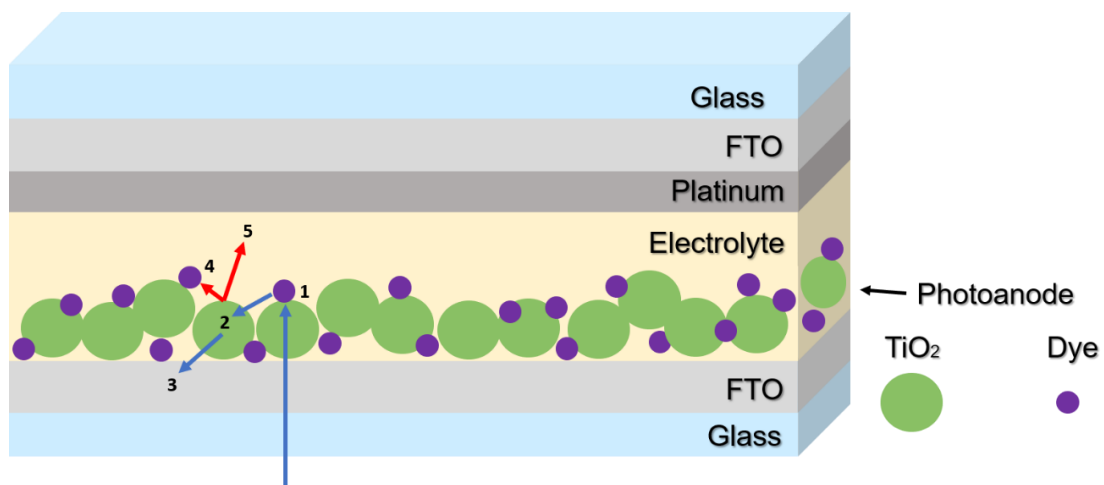
Figure 2. Structure of a DSSC composed of TiO_2. When a dye molecule absorbs a photon (1), it is elevated to an excited state, thus releasing an electron. The electron is injected into the semiconductor (2) and travels to the back contact (3). The electron can travel backwards and regenerate the dye (4) or the electrolyte (5).

1.2.6 Working Principle

The phenomenon of photosynthesis alike the working principle of DSSC involves light-dependent and light-independent reactions. In photosynthesis, plants go through a chain of reactions to produce sugar molecules and oxygen from sunlight. Upon sunlight irradiates onto the leaves, which have chlorophyll pigments with an absorption peak between 680 nm and 700 nm, the pigments are excited to their high energy state releasing two electrons, thus becoming an oxidative specie. The now free electrons are injected into protein complexes and into an enzyme, which initiates light-independent reactions. To regenerate the oxidized chlorophyll, plants split water molecules to obtain free electrons, then the enzyme is also regenerated into its original state [16].

Alike photosynthesis generates sugar molecules, DSSC generate electric power from sunlight without suffering permanent chemical transformations. When sunlight hits onto the DSSC, the dye adsorbed onto the semiconductor absorbs a photon and it is excited (Eq. 1), thus releasing an electron, and the dye becomes an oxidative specie (Eq. 2). The now free electron is injected into the semiconductor, through which it travels to the conductive substrate and through the external load to the counter electrode. Once in the counter electrode, the electron reduces the redox mediator (Eq. 3), which regenerates the dye (Eq. 4) completing the circuit [17]. However, the injected electron could travel backwards, reaching the oxidized dye (Eq. 5) or the electrolyte and regenerating them (Eq. 6) process that is known as recombination.

$$S_{(adsorbed)} + hv \rightarrow S^*_{(adsorbed)} \tag{1}$$

$$S^*_{(adsorbed)} \rightarrow S^+_{(adsorbed)} + e^-_{(injected)} \tag{2}$$

$$I_3^- + 2e^-_{(cathode)} \rightarrow 3I^-_{(cathode)} \tag{3}$$

$$S^+_{(adsorbed)} + \frac{3}{2}I^- \rightarrow S_{(adsorbed)} + \frac{1}{2}I_3^- \tag{4}$$

$$S^+_{(adsorbed)} + e^-_{(semiconductor)} \rightarrow S_{(adsorbed)} \tag{5}$$

$$I_3^- + 2e^-_{(semiconductor)} \rightarrow 3I^-_{(anode)} \tag{6}$$
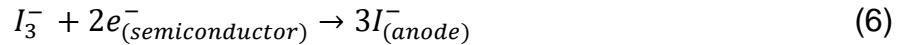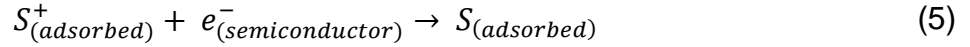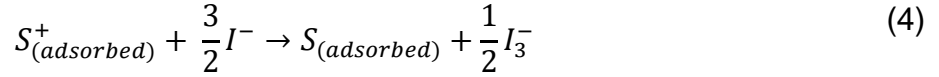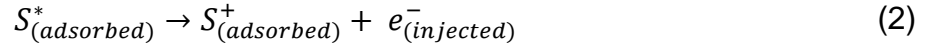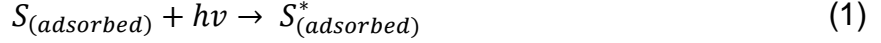
1.3 Semiconductors

Semiconductor materials have been the raw material that has allowed the development of electronic and optoelectronic devices [18-20]. Their band gap energy ranges between those of conductors and insulators and, are highly sensitive to the temperature and the content of impurities. As a matter of fact the best semiconductors are almost perfect crystalline structures [19]. There exist basically two types of semiconductors:

- Intrinsic: Elements as silicon and germanium who possess conductivities that are inherent of the pure element or material.
- Extrinsic: Semiconductors where the conductivity depends completely of the impurities. We can subclassify them in type n and type p. Type n are generated when the material is doped by an impurity with five valence electrons, like arsenic, antimony, phosphorus, which are called donors. Type p are doped by elements with three valence electrons, like aluminum, boron, gallium, which are called acceptors.

The electrical current through a section of a material is defined as the charge going through that section per time unit. Thus, in order current exists, it must exist particles transporting the charge; those mobile particles are called charge carriers. In semiconductors exist two types of charge carriers: conduction electrons, with negative charge and holes, with positive charge [20].

The most important energy bands in semiconductors correspond to the outer shell, completely full, and the unfilled shell. The first is represented by an energy band called valence band; the other is called conduction band [21]. The energies of the valence electrons are grouped in an interval called valence band, which superior limit is Ev. The energies that the free electrons can have are also grouped in an interval called conduction band, being Ec its inferior limit. Between both bands extends the band gap energy; any electron can have an energy within that margin. The amplitude of the band gap is called Eg and is one of the most important parameters of a semiconductor. That energy, defined as Eg = Ec - Ev, is the minimum energy that must be given to a valence electron to set it free from the covalent bond. The bigger is the value of Eg, the stronger is the covalent bond and less electrons can break it; thus, the material is less conducting [22].

1.3.1 Semiconductors in DSSC

In DSSC, the most used semiconductor is TiO_2 in anatase phase because of its large band gap and high conduction band edge, although the mobility of electrons through the nanoparticles is low (0.1-4 cm^2Vs^{-1}) [23]. Therefore, multiple oxides have been used as transport layer in DSSC, among these oxides are ZnO

9

[24], SnO$_2$ [25] and Nb$_2$O$_5$ [26], being ZnO the one that has shown the best performance.

1.3.2 Zinc Oxide (ZnO)

ZnO is a wide band gap semiconductor with unique properties; it exhibits an electron mobility close to 1000 cm^{2}Vs^{-1} for single-crystal nanowires and 200-300 cm^{2}Vs^{-1} for bulk material, it has a band gap energy of 3.37 eV for bulk materials [10,27] that can be easily tuned, it has high exciton binding energy (60 meV), it has good photostability, as well as high carrier mobility and conductivity and high piezoelectric reaction . Also, its preferential growth can be easily controlled to obtain diverse morphologies [28,29]. Thus far, ZnO has been synthesized in the shape of nanowires [30], nanorods [31], nanoflakes, nanotubes, three-like branched structures [23,32] and nanoflowers [33] among others. It has been used in many applications such as light emitting diodes (LEDs) [34], gas sensors [35], optical biosensors [36], photocatalysis [37], piezoelectric generators [38] and photovoltaic cells [24].

ZnO nanostructures have been synthesized by various methods as electrodeposition [39], chemical vapor deposition [40], thermal evaporation [41], sol-gel [42], microwave assisted [43], and hydrothermal methods [44], being the last named the most used. Hydrothermal method is the simplest of the mentioned for the synthesis of ZnO, due to the straightforward use of equipment or reactors and its short reaction times, which results in less energy consumption compared to other methods. Also, it is eco-friendly because it does not need hazardous

solvents. On the other hand, also by hydrothermal method it is possible to obtain different morphologies by adjusting various reaction parameters, such as pH, temperature and reaction time [45]. Although the hydrothermal synthesis of ZnO offers several advantages, it also presents improvement opportunities. For example, to synthesize ZnO nanoflowers the reaction time range between 45 min to 48 h, plus most synthetic routes require the use of hazardous additives to control the crystal growth [32,46,47], which do not agree with the principles of green chemistry [48].

Recently, new reactors have been developed and commercialized for solvothermal/hydrothermal synthesis, like the Monowave 50 from Anton Paar. This conductively heated sealed-vessel reactor allows reaction times up to 60 min, temperatures up to 250 °C and 20 bar, with a control of the temperature and pressure through the total reaction time. Besides, the equipment provides stirring velocities from 0 to 1200 rpm. The heating and cooling mechanism of this reactor allows the achievement of the desired temperature in matter of minutes. It presents several advantages over traditional hydrothermal/solvothermal methods; with the Monowave 50 the heating is achieved a lot faster, while with traditional equipment the thermal equilibrium between the surrounding media and the inside of the reactor can take hours. The equipment provides the desired temperature inside the vial and can support a pressure build-up up to 20 bar, both can be seen on the temperature and pressure profiles provided on real time and displayed on the screen. Deceivingly, when using traditional equipment, we cannot support the pressure build-up nor stirring, and we cannot know the exact temperature inside

11

the reactor. As an additional advantage, products synthesized by traditional method will need less reaction time if synthesized in the Monowave 50. As a matter of fact, studies have been realized and have proved that the performance of the Monowave 50 can be compared to that of a microwave reactor [49].

To date, multiple morphologies of ZnO nanostructures have been used as a photoanode in DSSC including nanotubes, nanowires, nanotips, nanoflowers and nanosheets to name a few [50]. Although they haven't surpassed the performance of TiO_2 devices [27], they are still considered a promising alternative. Specifically, ZnO nanoflowers have contributed to the obtention of better efficiencies by its large superficial area for more dye absorption, efficient scattering centers for more light collection and direct transport pathways [51].

1.4 Nanotechnology

The concept of nanotechnology was envisioned by Richard Feynman, who in 1959 gave a lecture called *There´s plenty of room at the bottom* [52]. In this lecture he talked about the manipulation of matter at an atomic scale and its possible applications, but nanotechnology started to be developed until the decade of 1980's.

When we talk about technology that involves materials at the nanoscale, we refer to nanotechnology. Scientists define nanomaterials as materials which have at least one dimension below 100 nm. When a material is changed from bulk scale to nanoscale, its chemical, thermal, mechanical, optical, electrical and magnetic properties differ, due to quantum confinement effects [53]. Nowadays, it has

12

applications in medicine, electronics, fuels, batteries, chemical sensors and solar cells, among others [54].

1.4.1 Plasmonics

Plasmonics is the field of study that fuses the size of nanoelectronics and the speed of dielectric photonics. Its prime objective is to apply the optical properties presented by metallic structures, thereupon allowing the guidance and manipulation of light at a nanometric scale. A plasmon is the excitation of a collective electron motion inside the metal particle, phenomena that befalls when an individual noble metal nanoparticle interacts with visible light.

Ag and Au nanoparticles exhibit a unique spectral response, which is due to the phenomenon of surface plasmon resonance (SPR). SPR occurs when specific wavelengths of light can lead the conduction electrons in the metal to collectively oscillate, but because these electrons cannot propagate, localized surface plasmon resonance (LSPR) occurs [55].

CHAPTER 2

BACKGROUND

In 1991 O'Regan and M. Grätzel developed the first DSSC [56]. Using low to medium-purity materials through low-cost processes, they created a photovoltaic cell which exhibited a good energy-conversion efficiency. Their solar cell, which had a coating of 10 μm and was composed of nanoparticles of TiO_2 impregnated by a charge-transfer dye, yielded a light-to-electric energy conversion of 7.1-7.9%, a current density (J_{SC}) of 1.15-1.3 mA cm^{-2}, open circuit voltage (V_{OC}) of 650-670 mV and fill factor (FF) of 0.685-0.7. The high efficiency of the DSSC was attributed to the high surface area of the coating of TiO_2 and the spectral characteristics of the dye. This breakthrough challenged conventional solid-state photovoltaic technologies by functioning at molecular and nanometric scale. Ever since, the primary structure of DSSC have remained the same, while the components' materials have varied.

In 2014, A. Chandiran et al. [10] made a comparison of the photovoltaic performances and the electron transfer dynamics in DSSC, between anatase TiO_2 and wurtzite ZnO as photoanodes. They deposited different thickness of these semiconductors by atomic layer deposition (ALD) on a mesoporous insulating

template and used them as photoanodes. The best performing device they reported, with 4.4% of efficiency, had a 5 nm ZnO or TiO₂ layer films, but other parameters varied. For ZnO DSSC the J_{SC} was 5.9 mA cm⁻², the V_{OC} was 896.4 mV and the FF was 0.68, while for the TiO₂ DSSC the obtained values were 7.0 mA cm⁻², 930.2 mV and 0.68. Though their results showed that at an optimal thickness ZnO exhibits a performance like that of TiO₂, the internal electron transfer properties differed. For the DSSC with a photoanode composed of ZnO the higher photogenerated electron transport rate enhanced the performance, while in the case of TiO₂ the low recombination rate, the higher dye loading, and fast electron injection contributed to the efficiency. Their work confirmed that ZnO is beneficial for systems demanding faster electron transport.

Thus far, ZnO has been employed as a photoanode in diverse morphologies as Jiang et al. did in 2007 [57]. They developed a DSSC with a photoanode composed of wurtzite ZnO and made a study of the impact that the morphology of the semiconductor has on the overall solar cell efficiency. They grew ZnO nanoflowers and nanorods by a hydrothermal method directly onto the FTO coated glass substrate and used N719 dye and I⁻/I₃⁻ electrolyte in the DSSC. Their results showed that the DSSC with a photoanode composed of ZnO nanoflowers, with a tip diameter of 200 nm, had an efficiency of 1.9%, J_{SC} of 5.5 mA cm⁻², V_{OC} of 650 mV and FF of 0.53, which was higher than the device composed of ZnO nanorods, which obtained 1.0% efficiency, J_{SC} of 4.5 mA cm⁻², V_{OC} of 630 mV and FF of 0.36. The higher efficiency was attributed to a better dye loading and light harvesting of the ZnO nanoflowers related to its larger superficial area.

In 2014, B. Kilic et al. [58] developed a DSSC using ZnO nanoflowers, N719 dye and I^-/I_3^- electrolyte, and as a reference they developed a solar cell with ZnO nanowires using the same dye and electrolyte. It is important to mention that the immersion time in the ethanolic dye solution was only of 30 min, this to prevent the dissolution of ZnO and the formation of Zn^{2+} agglomerates. The ZnO nanoflowers were grown on FTO substrate by hydrothermal method at a pH of 10, while ZnO nanowires were grown at a pH of 11. Their results showed an enhancement from 2.22% efficiency (J_{SC} of 0.336 mA cm^{-2}, V_{OC} of 748 mV and FF of 0.796) to 5.11% (J_{SC} of 3.404 mA cm^{-2}, V_{OC} of 756 mV and 0.497 as FF) when replacing the nanowires by nanoflowers. They associated the efficiency increase to the larger surface area of the nanoflowers, which had an average diameter of 1-1.5 µm, because they provided more dye loading, thus enhancing electron injection and charge-transfer efficiency. Moreover, nanowires have gaps which results in lower internal surface area, leading to incomplete absorption of photons, while nanoflowers have branches that fill these gaps, bringing a direct pathway for electron transport.

Although the DSSC based on ZnO haven't reached the efficiency of TiO$_2$-based devices, they are still considered a promising alternative because of its easy crystallization and the facile synthesis of different morphologies. With the purpose of improving individual and combined properties, heterogeneous TiO$_2$-ZnO materials have been used in photocatalytic reactions and photovoltaic processes. Due to the combination of the high activity of TiO$_2$ and the high electron mobility of ZnO, TiO$_2$-ZnO nanocomposites can provide improved performance. Moreover,

the alignment of the band gaps favors the separation of electrons and holes, hence suppressing the electron-hole recombination [59].

In 2016, H. Cai et al. [60] synthesized ZnO-coated TiO_2 nanotubes by ALD. The TiO_2 nanotubes exhibited anatase phase while the ZnO were wurtzite phase. They varied the thickness of the ZnO coating to study if it had any influence in the electrochemical and photoelectrochemical results, and their results showed indeed a variation of the properties. The highest increase in photoelectrochemical activity that they obtained was 60%, and it was achieved when TiO_2 nanotubes, with a wall thickness of 15 nm were coated by 2 nm of ZnO, this is 11% of ZnO. This improvement was attributed to the enhanced charge separation in the structure and the better crystallization of the ZnO and the TiO_2 nanostructures due to its annealing. With a thicker coating of ZnO the improvement on the electrochemical and photoelectrochemical properties was not as high as with a thinner coating.

In 2018, Sajjad et al. [61] synthesized TiO_2 and ZnO nanoparticles (with a diameter of 30 nm) by sol-gel method, and by chemical impregnation they combined both materials in different weight ratios (10, 15, 30 and 50%). The final heterostructures were used as photoanodes in DSSC, in conjunction with N719 dye and I^-/I_3^- as electrolyte. Even though, all the proportions of ZnO/TiO_2 showed an increased device efficiency when compared to bare TiO_2, the most efficient DSSC had 15% of ZnO with an efficiency of 2.8% (J_{SC} of 8.4 mA cm^{-2}, V_{OC} of 450 mV and FF of 0.75). The better performance was attributed to the linkage of Ti-O-Zn, which was probed by Fourier-transformed infrared spectroscopy (FT-IR). They

concluded that the ZnO performed as a passivation layer which reduced the electron recombination and enhanced the electron transport.

Khan et al. [62] , in 2018, assembled DSSC with stacked layers of ZnO/TiO₂ nanoparticles prepared by sol-gel method. They varied the layers in one, two and three spin-coating repetitions, which after being thermally treated were immersed in N719 dye. Its most efficient DSSC was the device with double layer of ZnO/TiO₂, having a V_{OC} of 730 mV, J_{SC} of 2.89 mA cm⁻², FF of 0.64 and efficiency of 1.36%. Its better performance was attributed to the blocking layer behavior between the FTO and the electrolyte of the ZnO, which aided to reduce the electron recombination rate and facilitated its transport. However, the device with three layers showed worse performance (V_{OC} of 750 mV, J_{SC} of 2.31 mA cm⁻², FF of 0.59 and efficiency of 1.03%) due to its larger thickness which affected the movement of the electrons through the ZnO/TiO₂ interfaces, thus resulting in more electron recombination.

In 2018, Bechelany et al. [63] synthesized by ALD ordered multilayers of urchin-like ZnO nanowires, which were grown over polystyrene spheres of 1 and 5 μm. They varied the layers of ZnO from two to four layers. Finally, also by ALD they coated the structures with a 9-14 μm coating of TiO₂, thus obtaining core-shell ZnO/TiO₂ nanostructures. The final structures were used as a photoanode in a DSSC, using N719 dye as sensitizer and I⁻/I₃⁻ as electrolyte. Even though, a larger content of ZnO increased the photon absorption, the photovoltaic performance of the device decreased. The decreased efficiency was attributed to the long distance traveled by the electrons, hence the device with one layer of ZnO (synthesized with

5 μm polystyrene spheres) was the most efficient with a V_{OC} of 670 mV, J_{SC} of 2.26, FF of 0.45 and efficiency of 1.38%. Regarding the polystyrene spheres used for the synthesis of the urchin-like ZnO nanostructures, it was proved that with 5 μm spheres higher DSSC efficiency was achieved, due to a higher electrical connection between the urchin layers.

Above have been mentioned some of the most important reports on the incorporation of ZnO/TiO$_2$ nanostructures in a DSSC, however in Table 1 are summarized more references. Herein are mentioned the morphology of the semiconductor nanoparticles, photovoltaic parameters of the device and the listed reference. It is important to mention that all the references listed below assemble the DSSC using N719 dye and I$^-$/I$_3^-$ as electrolyte.

Table 1. Photovoltaic parameters of DSSC composed of TiO$_2$ and ZnO.

Nanostructures	V_{OC} (mV)	J_{SC} (mA cm^{-2})	FF	Efficiency %	Ref.
TiO$_2$ nanotube/ TiO$_2$/ ZnO	820	10.80	0.65	5.80	[64]
ZnO nanowires/TiO$_2$ core-shell	800	4.78	0.59	2.27	[65]
Coaxial TiO$_2$/ZnO nanotubes	650	7.28	0.60	2.80	[66]
TiO$_2$ nanotubes/ZnO nanoparticles	720	6.77	0.65	3.17	[67]
TiO$_2$/ZnO core-shell	750	13.46	0.65	6.62	[68]
TiO$_2$/ZnO nanodonuts	780	16.70	0.69	9.00	[69]
ZnO/TiO$_2$ core-shell	760	6.30	0.60	3.10	[70]

Recent researches have employed the LSPR from metallic nanoparticles with the objective of improving the performance of the DSSC by enhancing the light-harvesting capacity of absorbers over a broader range of wavelengths. Among the metallic nanostructures that have been used are Au [55], Ag [71], and Al [72]. Here are summarized some of these works.

In 2012, S. Muduli et al. [73] compared two DSSC, one had a photoanode of TiO$_2$-Au, while the other had TiO$_2$. The DSSC characterization showed that the solar cell with TiO$_2$-Au had an efficiency of 6.0%, J_{SC} of 13.2 mA cm^{-2}, V_{OC} of 700 mV and FF of 0.56, being the efficiency and the J_{SC} higher than in the solar cell with TiO$_2$ (5.0% efficiency, 12.6 mA cm^{-2}, 700 mV and FF of 0.61). They also characterized the DSSC by electrochemical impedance spectroscopy (EIS) to study the electron transport and charge recombination, obtaining a minor electron transfer resistance for the DSSC with Au NPs (11 Ω) compared to the reference DSSC (14.2 Ω). They concluded that the efficiency enhancement was due to a lower charge transfer resistance, as the results proved, including lower electron recombination between the TiO$_2$/electrolyte interface in the solar cell with a Au nanoparticles-decorated photoanode.

N. Chander et al. [74] conducted a research to achieve the best performance of a DSSC based on a TiO$_2$-Au photoanode in 2014. They varied the size and concentration of the Au nanoparticles to find the best combination. They synthesized Au nanoparticles that varied in size from 5 nm to 85 nm. Subsequently, they mixed TiO$_2$ nanoparticles with different concentrations of Au nanoparticles (0.1 to 0.25 wt%). Their results showed that the best performing DSSC had 0.24

wt% of 36 nm Au nanoparticles, achieving photovoltaic parameters of 640 mV, 16.7 mA cm^{-2}, FF of 0.68 and efficiency of 7.35%. They also proved that smaller (5 nm) and larger (85 nm) nanoparticles do not have a positive performance.

In 2014, S. Lim et al. [75] synthesized TiO$_2$ nanoparticles decorated with Ag nanoparticles (2-4 nm) by simple chemical reduction method. The composites that they prepared were employed as photoanodes in a DSSC to determine if its presence lead to an enhancement. They prepared five photoanodes with different contents of Ag nanoparticles (0, 1, 2.5, 10, 20 wt%). The solar cell with 2.5 wt% Ag showed an efficiency of 4.86% (V_{OC} of 770 mV, J_{SC} of 12.19 mA cm^{-2} and FF of 0.52), higher than one without it which achieved an efficiency of 2.57% (V_{OC} of 710 mV, J_{SC} of 6.71 mA cm^{-2} and FF of 0.54). They confirmed that the incorporation of the Ag nanoparticles significantly influenced the optical properties in the region of 400-500 nm due to the surface plasmon resonance effect.

In 2008, V. Dhas et al. [76] assembled a DSSC based on ZnO nanoflowers loaded with Au nanoparticles. They integrated the Au nanoparticles on ZnO nanoflowers by hydrothermal method. Structural and morphological characterization showed wurtzite phase and uniformly sized (3 μm) multiple branched structures, while Au nanoparticles whereupon 10 nm. They used N3 dye as sensitizer and I$^-$/I$_3^-$ as electrolyte. The results from their photovoltaic characterization showed that the incorporation of Au nanoparticles enhanced the DSSC efficiency from 1.6% (V_{OC} of 580 mV, J_{SC} of 8.75 mA cm^{-2} and FF of 0.32) to 2.5% (V_{OC} of 500 mV, J_{SC} of 15 mA cm^{-2} and FF of 0.33). The incorporation of Au nanoparticles was seen to reduce the recombination centers present in the

oxygen vacancies of ZnO, also the LSPR of the metallic nanoparticles overlaps that of the dye, increasing the photon absorption.

1.5 Background of Hydrothermal Synthesis of ZnO Nanoflowers

P. Fageria et al. [77] synthesized ZnO/Au and ZnO/Ag nanoparticles in 2014. Their objective was to modify the ZnO nanoflower surface with Au and Ag nanoparticles and prove if its incorporation enhanced the photocatalytic activity of the material. Their results showed that upon modification with noble metals the photocatalytic activity of ZnO significantly increases, this is due to the metallic sites acting as an electron trap on the semiconductor surface. To obtain the nanoparticles, first ZnO nanoflowers were obtained by a surfactant assisted method, followed by Ag and Au deposition using hydrazine hydrate as reducing agent. The nanoflowers were composed by petals with a diameter of 600 nm and width of 220 nm and presented wurtzite phase.

In 2012, Kochuveedu et al. [78] synthesized ZnO nanoflowers by a simple hydrothermal method using zinc acetate and NaOH as reagents and without using surfactants. They investigated the influence of the temperature on the morphology while the reaction time (45 min) was kept constant. The results showed that a morphological change occurred when the reaction temperature was changed among 140, 160 and 180 °C. As the reaction temperature increased, the flower diameter increased as well, while the petal length decreased. At 140 °C the nanoflowers had an average diameter of 8-9 μm. Their structural characterization showed that the ZnO nanoflowers had wurtzite phase. Also, they tuned the Eg of

the ZnO by a surface-plasmon-mediated approach by its decoration with Au nanoparticles. To decor the ZnO first the Au nanoparticles were synthesized by citrate reduction method, then the ZnO nanoflowers were dispersed and stirred in the Au nanoparticle solution for a given time.

1.6 Hypothesis

The incorporation of Au nanospheres in combination with ZnO nanoflowers into the photoanode of a DSSC composed of TiO_2, enhances its efficiency due to the plasmonic properties of the Au nanospheres in conjunction with the large superficial area of the ZnO nanoflowers.

1.7 General Objective

To enhance the performance of a DSSC based on TiO_2 with ZnO nanoflowers, incorporating Au nanospheres.

1.8 Specific objectives

1. To synthesize flower-like ZnO nanostructures via hydrothermal method.
2. To characterize ZnO nanostructures by X-ray diffraction (XRD), diffuse reflectance spectroscopy (DRS), field-emission scanning electron microscopy (FE-SEM) and four-point probe.
3. To decorate the ZnO nanoflowers with Au nanospheres.
4. To characterize the ZnO nanoflowers decorated with Au nanospheres by FE-SEM/energy dispersive spectroscopy (EDS) and inductively coupled plasma atomic emission spectroscopy (ICP-AES).

5. To synthesize a paste of commercial TiO_2 and ZnO nanoflowers decorated with Au nanospheres.

6. To deposit the paste in the FTO by screen-printing to create a coating.

7. To characterize the coating by mechanical profilometry, FE-SEM and XRD.

8. To characterize the solar cell by: the obtention of its characteristic J-V curve obtaining the open-circuit voltage (V_{OC}), short-circuit photocurrent (J_{SC}), fill factor (FF) and efficiency. Furthermore, by electrochemical impedance (EIS) and intensity modulated photovoltage and photocurrent (IMVS/IMPS) spectroscopies.

9. To evaluate the enhancement in the efficiency of a DSSC with Au nanospheres.

10. To determine the proportion of ZnO nanoflowers/TiO_2 with and without Au nanospheres exhibiting the best performance.

CHAPTER 3

METHODOLOGY

3.1 Hydrothermal synthesis of ZnO nanoflowers

For the synthesis of ZnO nanoflowers two different approaches were conducted:

For the first method, a 0.3 mol/L zinc acetate dihydrate ($Zn(CH_3COO)_2 \cdot 2H_2O$, J.T. Baker, 99.8%) solution and a 3 mol/L NaOH (DEQ, 99%) solution were prepared. Next, 25 mL of the zinc acetate solution were mixed with 7.7 mL of the NaOH solution to obtain a pH of 13.2, the mixing was done under stirring at 300 rpm. 5 mL of this mixture were transferred to a vial, a magnetic stirrer was added, and the vial was sealed with a cap to be treated in a conductively heated sealed-vessel reactor model Monowave 50 (Anton Paar) at a temperature of 90 °C for 30 min. The obtained powder was centrifuged and washed with ethanol three times, and once with water before being dried at 100 °C for 2 h.

For the second method, two aqueous solutions were prepared: a 0.012 mol/L zinc acetate dihydrate ($Zn(CH_3COO)_2 \cdot 2H_2O$, J.T. Baker, 99.8%) solution, which was stirred for 5 min under 360 rpm, and a 6.9 mol/L NaOH (DEQ, 99%) solution.

Next, 5 mL of the zinc acetate solution and 0.2 mL of the NaOH solution were mixed in a vial. A magnetic stirrer was added to the vial and it was sealed with a cap to be treated in a conductively heated sealed-vessel reactor model Monowave 50 (Anton Paar) at a temperature of 140 °C and 2 bar for 5, 10, 15, and 30 min. The obtained powder was centrifuged and washed with ethanol three times, and once with water before being dried at 100 °C for 2 h.

3.2 ZnO characterization

XRD was performed using a Bruker D2 Phaser powder diffractometer at room temperature with Cu Kα radiation (1.5405 Å) within Bragg angle 2θ from 5° to 90° to determine the crystalline structure of the ZnO nanoflowers. Also, the crystallite size was obtained applying the Scherrer equation (Eq. 7) [79] using the data from the patterns.

$$\tau = \frac{K\,\lambda}{\beta\cos\theta} \tag{7}$$

where τ is the mean size of the crystal domains, K is a dimensionless shape factor (0.94), λ is the wavelength of the X-ray irradiation, β is the line broadening at half the maximum intensity and θ is the Bragg angle.

Also, FE-SEM micrographs were obtained using a FEI Nova NanoSEM 200 microscope operated at 12 kV using a Helix detector to examine the morphology of the ZnO nanoflowers. In addition, the data obtained from a diffuse reflectance UV-Vis spectrophotometer in DRS mode (Nicolet Evolution 300 PC) were used to calculate the band gap energy of ZnO nanoflowers through the Kulbelka-Munk equation (Eq. 8) [80]:

$$F(R) = \frac{(1 - R_\infty)^2}{2R_\infty} \tag{8}$$

where R is the absolute reflectance.

After XRD, FE-SEM and DRS, the ZnO powders were introduced into a paste to deposit a coating over a glass substrate and perform a four-point probe test to obtain the sheet resistance of the material. The procedure for the paste synthesis was the next: 0.0200 g of ethylcellulose (Aldrich, viscosity 100 cP, 48% ethoxyl) were dissolved in 0.4060 g of terpineol (Aldrich 99.5%, mixture of isomers, anhydrous), under vigorous stirring and a temperature of 90 °C. Then, 0.0500 g of ZnO were dispersed in 1 mL of ethanol. Both mixtures were combined and stirred. The resulting mixture was heated in a 90 °C heating bath and stirred under 60 rpm until constant volume. The pastes were coated glass substrates which were previously cleaned in successive ultrasonic baths of acetone, isopropanol and deionized water for 10 min each, and they were let dry in air. When the substrates were dry, the pastes were deposited by doctor blade method using a tape mask to obtain an area of 1 cm^2. Thereafter, the glass substrates were thermally treated at 450 °C for 40 min to eliminate the organic compounds of the paste. The four-point probe was conducted on the coatings with a Hewlett Packard multimeter 3478A to obtain the sheet resistance.

3.3 Decoration of ZnO nanoflowers with Au nanoparticles

For the decoration of ZnO nanoflowers three methods were tested; impregnation, *in situ* synthesis in Monowave 50 and *in situ* synthesis in hot plate.

3.3.1 Impregnation method

For the impregnation method, first the Au nanoparticles were synthesized by citrate reduction method: a 5 mL of a 0.25 mmol/L $HAuCl_4$ (Aldrich, hydrogen tetrachloroaurate trihydrate ≥99%) solution was heated until boiling temperature under stirring. When boiling 250 μL of a 1 w/v% sodium citrate (Aldrich, $Na_3C_6H_5O_7 \cdot 2H_2O$ ≥99%, FG) solution were added. The mixture was left boiling under stirring for 20 min and let cool before being diluted to 5 mL. Next, 0.0083 g of ZnO nanoflowers were dispersed in the Au nanoparticles solution using an ultrasonic bath, a stirring bar was added, and the dispersion was stirred in darkness for 4 h. The dispersion was centrifuged, and the obtained powders were washed once with distilled water and dried at 100 °C for 90 min.

3.3.2 Synthesis *in situ* in Monowave 50

The synthesis of Au nanoparticles in presence of ZnO nanoflowers was first essayed in the Monowave 50 as follows: 5 mL of a 0.25 mmol/L $HAuCl_4$ (Aldrich, hydrogen tetrachloroaurate trihydrate ≥99%) solution and 0.0083 g of ZnO nanoflowers were introduced into the vessel and dispersed using an ultrasonic bath. Next, 250 μL of 1 w/v% sodium citrate (Aldrich, $Na_3C_6H_5O_7 \cdot 2H_2O$ ≥99%, FG) solution and a stirring bar were added, the vessel was sealed and introduced into the reactor. The conditions of the conductively heated sealed-vessel reactor were 100 °C for 20 min with a stirring of 600 rpm. The obtained dispersion was centrifuged, and the powders were washed once with distilled water and dried at 100 °C for 90 min.

3.3.3 Synthesis *in situ* in hot plate

For the *in situ* synthesis in a hot plate, different weights of ZnO nanoflowers were decorated to maintain the total amount of Au nanoparticles similar in all the DSSC. For the DSSC containing 5% of ZnO, 0.0051 g of ZnO were dispersed in 5 mL of a 0.25 mmol/L $HAuCl_4$ (Aldrich, hydrogen tetrachloroaurate trihydrate ≥99%) solution and heated to boil under stirring. When the boiling temperature was reached, 250 µL of 1 w/v% sodium citrate (Aldrich, $Na_3C_6H_5O_7 \cdot 2H_2O$ ≥99%, FG) solution were added, and the mixture was left at boiling temperature and stirring for 20 min. The dispersion was centrifuged and washed with distilled water once before being dried at 100 °C for 2 h. For the others DSSC the same procedure was followed but the content of ZnO varied, thus the quantity of $HAuCl_4$ and sodium citrate also changed. For the DSSC containing 10% of ZnO 0.0051 g were decorated in 2.5 mL of $HAuCl_4$ 0.25 mmol/L and 125 µL of 1 w/v% sodium citrate solution were added, and for the one containing 15% of ZnO 0.0061 g, 2 mL of $HAuCl_4$ and 100 µL of sodium citrate were needed.

3.4 Characterization of ZnO/Au nanoflowers

The morphology of the ZnO nanoflowers decorated with Au nanoparticles was obtained by FE-SEM in a FEI Nova NanoSEM 200 microscope, operated at an accelerating voltage of 15 kV using a Helix detector. The elemental composition was obtained by EDS using an INCA X-Sight detector coupled to the microscope. The Au nanoparticles concentration was measured by ICP-AES in a Thermo Electron-ICAP 6500 spectrometer. The samples for ICP-AES were prepared

dissolving 21 mg of sample in 12 mL of aqua regia (HCl/HNO$_3$, 3:1), using open vessels in a hot plate (70-85 °C) for the acid digestion.

3.5 Synthesis of TiO$_2$ and ZnO or ZnO/Au nanoflowers paste

To prepare the paste first 0.15 g of ethylcellulose (Aldrich, viscosity 100 cP, 48% ethoxyl) were mixed with 10 mL of ethanol and the mixture was treated in an ultrasonic bath for 1 h to dissolve the solid. The powder mixture (0.5 g) was also mixed with 10 mL of ethanol and it was dispersed in an ultrasonic bath also for 1 h. Next, 4.1 g of terpineol (Aldrich 99.5%, mixture of isomers, anhydrous) were added to the dispersion of the powders in ethanol and again it was treated for 1 h in an ultrasonic bath. Both mixtures, the dissolution of ethylcellulose in ethanol and the dispersion of the powders with terpineol and ethanol, were combined and again treated in an ultrasonic bath for 1 h, before being reduced in a rotary evaporator (Buchi R-210) with a heating bath (Buchi B-491) at 45 °C and a vacuum pump (Buchi V-700) at 175 mPa. 15 mL of ethanol were removed from the paste. In Table 2 are specified the name of the sample and its proportion of ZnO nanoflowers, TiO$_2$ nanoparticles and Au nanoparticles.

Table 2. Specification of proportion of ZnO nanoflowers, TiO$_2$ nanoparticles and Au nanoparticles for each sample.

Name of the sample	Proportion of ZnO nanoflowers (wt%)	Proportion of TiO$_2$ nanoparticles (wt%)	Amount of Au nanoparticles (ppm)
T	0	100	0
5Z-95T	5	95	0
5Z-95T-601A	5	95	601
5Z-95T-550A	5	95	550
5Z-95T-418A	5	95	418
10Z-90T	10	90	0
10Z-90T-1099A	10	90	1099
15Z-85T	15	85	0
15Z-85T-1255A	15	85	1255

3.6 Counter electrode preparation

The counter electrode of each DSSC was a platinum coated FTO (8 Ω/sq). First, two holes were drilled in the substrate with a rotary tool (Dremmel), this is to inject the electrolyte during the DSSC assembly. Next, a drop of precursor of platinum, Platisol T (Solaronix), was applied to an area of 0.5 cm^2. The procedure was repeated 3 times, letting dry between each deposition. To activate the platinum coating, the FTO was thermally treated at 450 °C for 30 min.

3.7 Paste deposition

FTO substrates (15 Ω/sq) were washed in ultrasonic baths of distilled water and ethanol for 10 min each, and in isopropanol for 20 min and let dry in air. The pastes were deposited by screen printing method using an ATMA AT-25PA printer and a screen of mesh 90 (mesh opening 62 μm). Several layers were deposited to obtain a final thickness of 11 μm (measured with a profilometer KLA Tencor D-120 with a speed of 0.40 mm/s, range of 100 μm and a force of 0.03 mg). Between each layer of paste the substrate was heated at 120 °C for 10 min in a hot plate, and when cooled another layer was deposited. When the desired thickness was reached, the substrates were thermally treated to eliminate the organic compounds in the paste as depicted in Table 3.

Table 3. Steps of thermal treatment of the electrodes.

Initial temperature (°C)	Final temperature (°C)	Time the temperature was reached (min)	Time the temperature was hold (min)
25	325	105	10
325	375	20	10
375	450	20	10
450	530	30	60
530	80	120	Overnight

3.8 Electrolyte preparation

The electrolyte consisted of 0.1 mol/L LiI (Aldrich, 99.9%), 0.1 mol/L GuSCN (Aldrich, ≥97%), 0.05 mol/L I_2 (Aldrich, ≥99.8), 0.5 mol/L 4-tert-butylpyridine (TBP, Aldrich 96%) and 0.6 mol/L 1,2-dimethyl-3-propylimidazolium iodide (DMPII, Solaronix) which were added to a mixture 15:85 v/v% of valeronitrile (Aldrich, 99.5%) and acetonitrile (Aldrich, 99.8%) respectively. The solution was sonicated in an ultrasonic bath for 15 min.

3.9 DSSC assembly

After the thermal treatment, the substrates (at 80 °C) were immersed in a 0.3 mmol/L ethanolic solution of N719 dye (Aldrich, 95%) for 24 h. After the time had passed, the substrates were rinsed with ethanol to eliminate any excess dye molecules. A sandwich configuration was made using the photoelectrode and counter electrode, putting a frame of Surlyn (60 μm, Dupont) and they were clamped together. The DSSC was introduced in an oven at 215 °C for 100 s to seal the electrode and counter electrode. When cooled, the electrolyte was injected through the holes in the counter electrode, and then they were sealed using Surlyn and a glass slide. The conductive side of the substrates was painted with a conductive Ag paint (SPI Supplies).

3.10 Electrode characterization

To obtain the crystalline structure of the semiconductor oxide in the electrodes, they were characterized by XRD using a Siemens D-5000 diffractometer at room

temperature with Cu Kα radiation (1.5405 Å) within Bragg angle 2θ from 20° to 80°. To determine the coupling of the materials in the electrode its FE-SEM images were obtained with a Jeol JSM 7600F microscope operated at 5 kV using a secondary electron detector (SEI) and at 15 kV using a low-angle backscattered detector (LABE). The larger accelerating voltage was used to identify the Au nanoparticles.

3.11 DSSC characterization

The photovoltaic characterizations were done under a set-up consisting of a 450 W ozone-free Xe-lamp (Newport corporation) with a water filter, calibrated to an irradiance of 100 mW cm^{-2} on the surface of the solar cell using an Air Mass 1.5 Global (AM 1.5 G) optical filter (Newport Corporation). The intensity was calibrated using a certified 4 cm^2 monocrystalline silicon reference cell with incorporated KG-5 filter. The J-V curves were obtained using a Gamry potentiostat/galvanostat/ZRA 3000. From the data of the J-V curves were obtained the V_{OC} and J_{SC}, and were calculated the FF and efficiency through the Eq. 9 and 10 [81]:

$$FF = \frac{P_{max}}{J_{sc}V_{oc}}$$
(9)

$$Efficiency = \frac{J_{sc}V_{oc}FF}{A\,P_{sun}} \times 100$$
(10)

Where P_{max} is defined as the product of J_{max} and V_{max} is the maximum power, A is the active area of the solar cell and P_{sun} is the light intensity per unit area (100 mW cm^{-2} in standard conditions).

To obtain information about the internal processes of the solar cell EIS, IMVS and IMPS measurements were performed in an Autolab PGSTAT302N/FRA2 set-up. The EIS measurements were obtained in dark with an applied DC bias voltage set at the V_{OC} of the DSSC and an AC amplitude of 10 mV and the frequency ranged from 10^{-1} to 10^5 Hz. The resulting EIS spectra (Nyquist plots) were analyzed using Z-View software to simulate an equivalent electrical circuit, obtaining the recombination resistance (R_{CT}) and chemical capacitance (C_μ), and the electron lifetime ($T_{1/2}$) which were calculated through the Eq. 11 [82]. IMVS measurements were obtained at modulation frequencies ranging from 1 mHz to 10 kHz, using a red LED (625 nm) to illuminate the DSSC, which also served as the bias illumination and the small sinusoidally modulated probe beam. IMPS spectra were also obtained under the illumination of a red LED. The Eq. 12 [83] was used to calculate the $T_{1/2}$ using the data from the IMVS spectra, and Eq. 13 [84] allow the calculation of the chemical diffusion coefficient:

$$T_{1/2} = R_{CT}C_\mu \tag{11}$$

$$w_{max} = T_{1/2}^{-1} \tag{12}$$

$$D_n = \frac{L^2 w_{max}}{2.35} \tag{13}$$

Being w_{max} the top of the obtained arc in IMVS and IMPS and L the thickness of the semiconductor coating.

CHAPTER 4

RESULTS AND DISCUSSION

4.1 First synthesis method of ZnO nanoflowers

4.1.1 FE-SEM

Since a specific morphology was desired, the first characterization for the samples was FE-SEM followed by XRD and DRS.

The first synthesis method essayed for the obtention of flower-like morphology, method 1, was based on the report by Shin et al. [85]. Since they used a three-necked refluxing pot, it had heating and stirring as the conductively heated sealed-vessel reactor (Monowave 50), that was the reason this method was chosen for its reproduction. Their method was reproduced, using the same time and temperature they reported, 30 min and 90 °C, the only variation was the equipment used. The Fig. 3 shows the FE-SEM micrographs of the nanoflowers obtained by the method 1. The nanoflowers are composed of thin layers forming a rose-dessert like morphology with a diameter of 800 nm. This first experiment probed that already established synthetic routes, even though they use simultaneous heating and stirring, are not reproducible in the conductively heated sealed vessel-reactor due to the mechanism of the reactor.
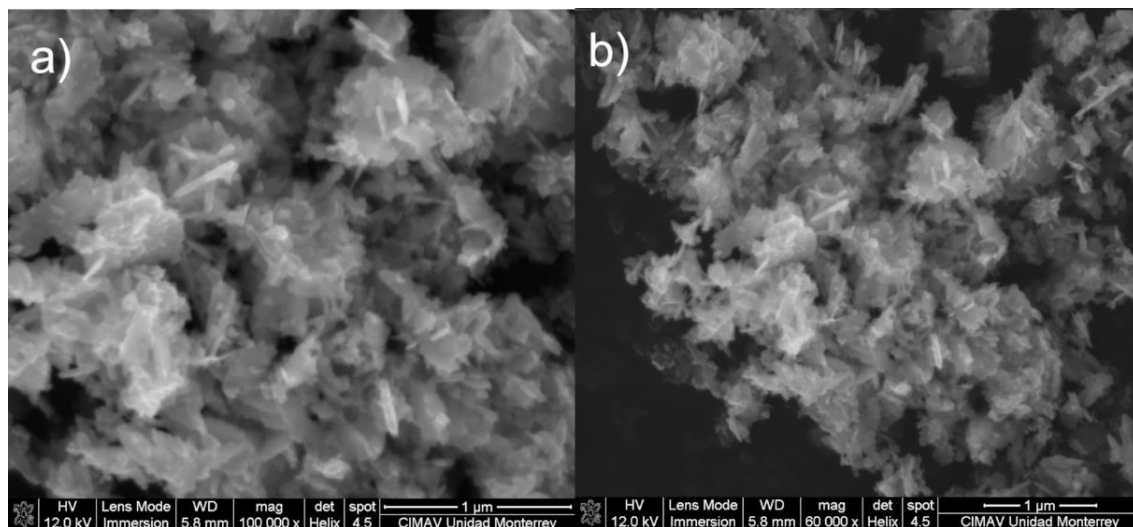
Figure 3. a) 100,000X and b) 60,000X FE-SEM micrographs of ZnO rose-desert nanoflowers.

Even though the morphology was not the desired XRD, DRS and four-point probe were performed to know the structural, optical and electrical properties of the material.

4.1.2 XRD

Fig. 4 shows the XRD pattern obtained, as observed all the diffraction peaks agree with the JCPDS card 00-036-1451 corresponding to wurtzite structure (hexagonal), without displacements and showing high crystallinity. No others diffraction peaks are visible, therefore there are not impurities detectable by XRD in the sample. Also, its crystallite size was obtained using the Scherrer equation (Eq. 7), giving a result of 26.9 nm.
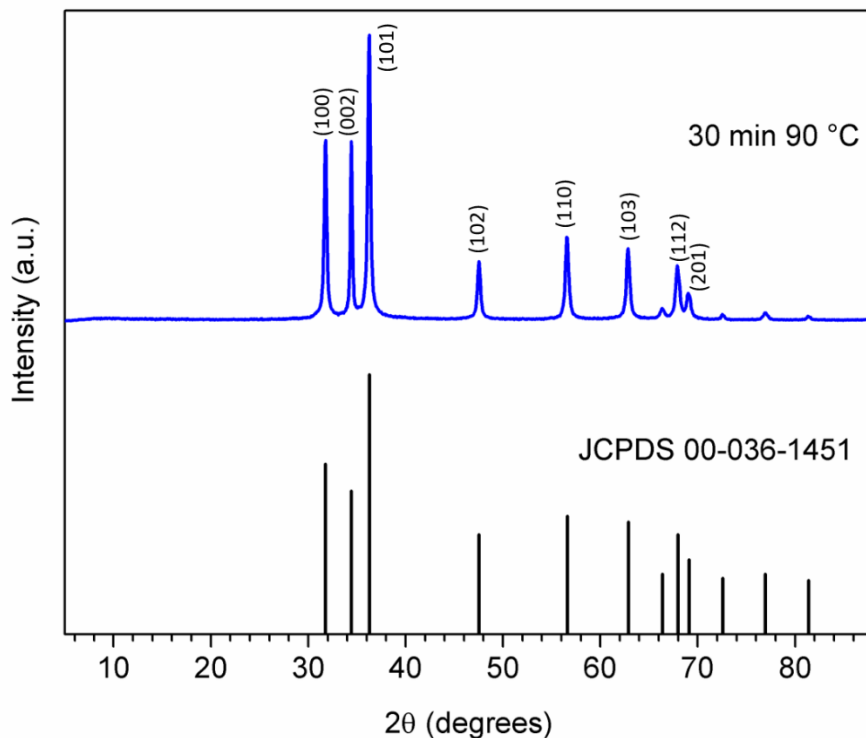
Figure 4. XRD pattern of ZnO rose-desert nanoflowers and JCPDS 00-036-1451 correspondent to wurtzite phase.

4.1.3 DRS and four-point probe

In the Fig. 5a we can observe the DRS of the sample, which data serve to obtain the band gap energy of the sample through the Kubelka-Munk function (Fig. 5b) (Eq. 8) obtaining a value of 3.21 eV, which agrees with the values reported for ZnO nanostructures [86].
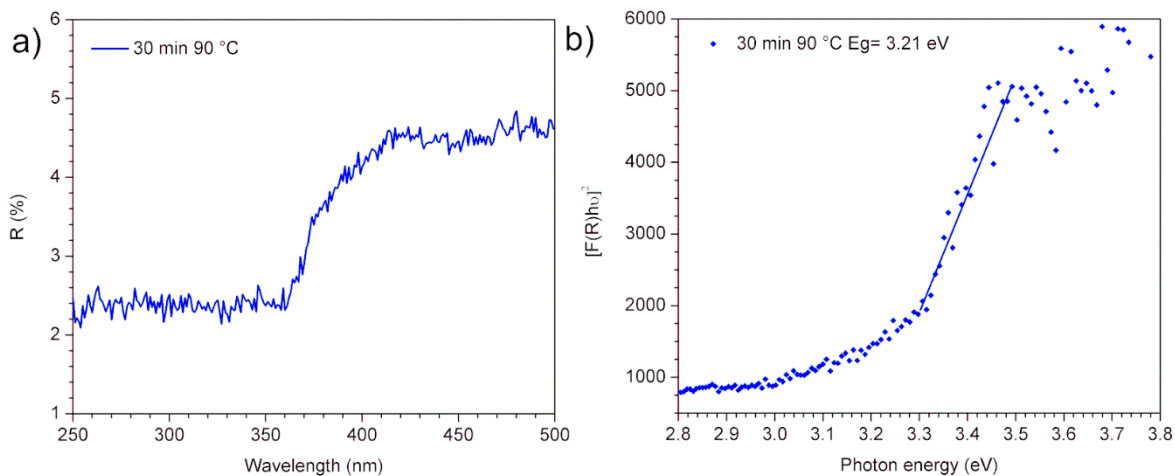
Figure 5. a) DRS spectra of ZnO rose-desert nanoflowers and b) Tauc plot of ZnO rose-desert nanoflowers.

Finally, the sheet resistance of an electrode composed of this nanoflowers was obtained through a four-point probe, obtaining a result of 45 MΩ/sq.

4.2 Second synthesis method of ZnO nanoflowers

For the method 2, a higher temperature was chosen, 140 °C, but the initial time remained the same (30 min). The reaction temperature was chosen based on the formation mechanism, explained below, previously reported by various authors [37,78,87–90], which suggest the need of a high temperature to obtain nanoflowers composed of rods.

40

4.2.1 FE-SEM

The Fig. 6 shows FE-SEM micrographs in low and high magnifications. As probed by the Fig. 6a the nanoflowers are grown in high quantity and in a homogeneous form, due to the stirring mechanism of the conductively heated sealed vessel reactor. As seen in Fig. 6b (high-magnification) the nanoflowers are composed of eight uniform petals, six petals in the same plane and two orthogonal to it, all growing from a nucleus. The petals have the shape of rods with pyramidal tips, each petal having a width of 370 ± 50 nm and a length of 770 ± 80 nm, and the total flower ensemble has a length of 1780 ± 150 nm.

Figure 6. a) 15,000X and b) 100,000X FE-SEM micrographs of ZnO nanoflowers synthesized for 30 min at 140 °C. Adapted from [91] Copyright Elsevier 2019.

Next, to shorten the reaction times and to find out the minimum time needed to obtain ZnO nanoflowers, three more synthesis were carried out at the same temperature (140 °C) with reaction times of 5, 10 and 15 min.

In the Fig. 7, 8 and 9, we can observe the FE-SEM micrographs corresponding to these experiments. As observed from the high-magnification micrographs (Fig. 7b, 8b and 9b) all the nanoflowers are composed by eight petals, six in the same plane and two orthogonal to it, so the morphology does not change along the reaction time. In the Table 4 are summarized the dimensions of the nanoflowers, which were obtained with the software ImageJ. As observed in the Table 4, the petals composing the nanoflowers grow along the reaction time, going from a length of 714 ± 81 nm and a width of 288 ± 27 nm at 5 min to 772 ± 85 nm and 370 ± 50 nm in length and width respectively at 30 min, which agrees with the formation mechanism explained below. In the Fig. 8b we can observe a nanoflower that has grown from a twin nucleus, therefore two rods with pyramidal tips have grown from the center instead of one. As seen in Fig. 7a, 8a and 9a (low magnification micrographs), in all cases the nanoflowers are grown in high quantity as well as the ones synthesized for 30 min.
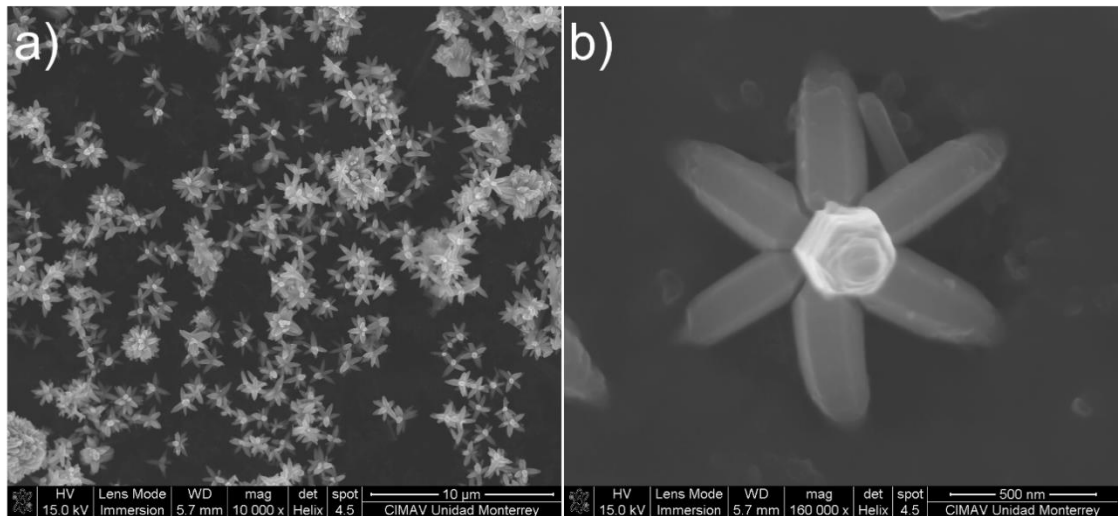
Figure 7. a) 10,000X and b) 160,000X FE-SEM micrographs of ZnO nanoflowers synthesized for 5 min. Adapted from [91] Copyright Elsevier 2019.
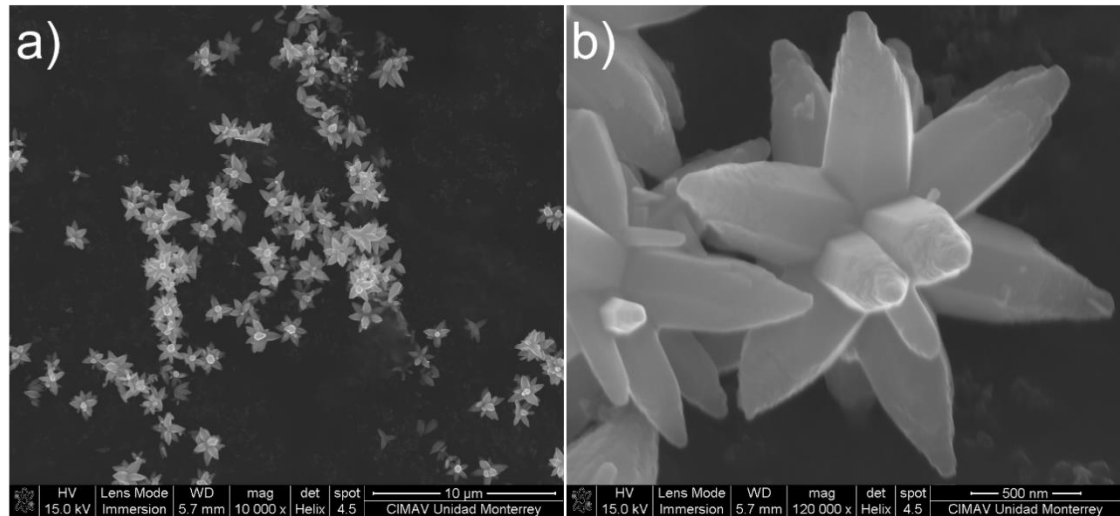
Figure 8. a) 10,000X and b) 120,000X FE-SEM micrographs of ZnO nanoflowers synthesized for 10 min. Adapted from [91] Copyright Elsevier 2019.
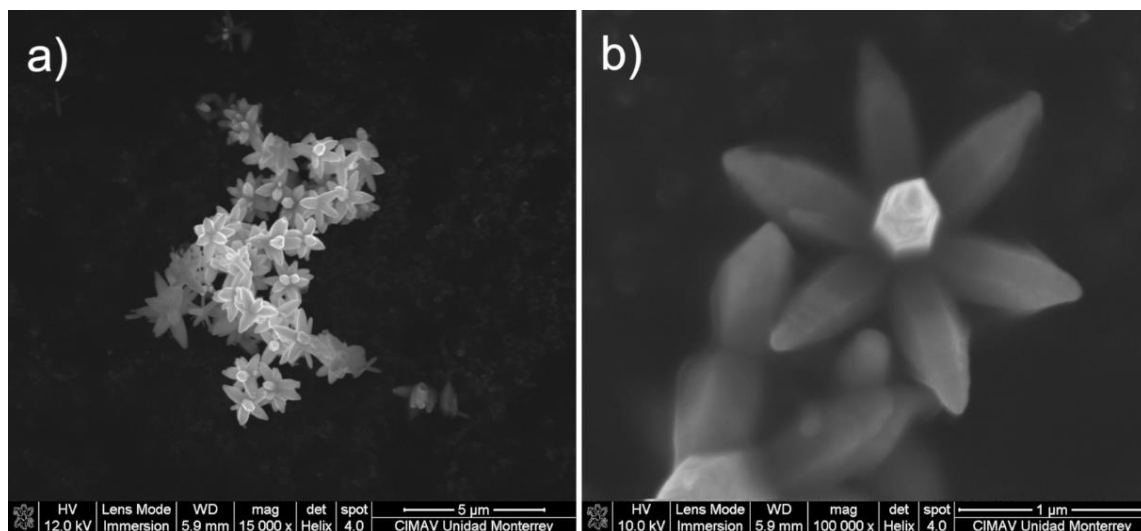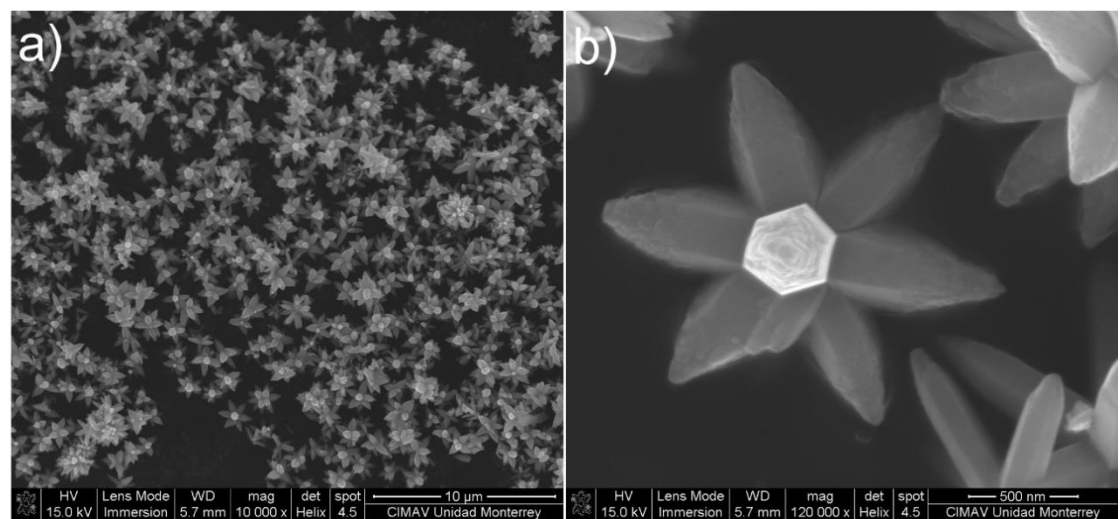

Figure 9. a) 10,000X and b) 120,000X FE-SEM micrographs of ZnO nanoflowers synthesized for 15 min. Adapted from [91] Copyright Elsevier 2019.

4.2.2 Formation mechanism

The formation mechanism of the ZnO nanoflowers starts with the Zn^{2+} and OH^- ions, provided by the $Zn(OAc)_2$ and the NaOH, respectively. The next step is the formation of $Zn(OH)_2$ (Eq. 13), which needs a strong alkaline medium to form, that

is why the molarity of NaOH must be high to supply enough OH⁻ ions. When the supersaturation exceeds the critical value a hexagonal nucleus composed by $Zn(OH)_2$ is formed. With the aid of the high temperature, active sites form in each corner of the hexagonal nucleus, attracting $Zn(OH)_4^{2-}$ ions, which eventually agglomerate and form the petals (Eq. 14). Thus, the $Zn(OH)_2$ ion and the $Zn(OH)_4^{2-}$ ions became the nucleus and the building block respectively. Finally, upon decomposition of the $Zn(OH)_4^{2-}$ ion, ZnO forms (Eq. 15) [37,78,87–90]. As seen by the FE-SEM micrographs, within 5 min of reaction time the nucleation and petal growth has already happened, but the crystal growth continues along the reaction time, as depicted by the scheme of Fig. 10.

$$Zn^{2+} + 2OH^- \rightarrow Zn(OH)_2 \tag{13}$$

$$Zn(OH)_2 + 2OH^- \rightarrow Zn(OH)_4^{2-} \tag{14}$$

$$Zn(OH)_4^{2-} \rightarrow ZnO + H_2O + 2OH^- \tag{15}$$
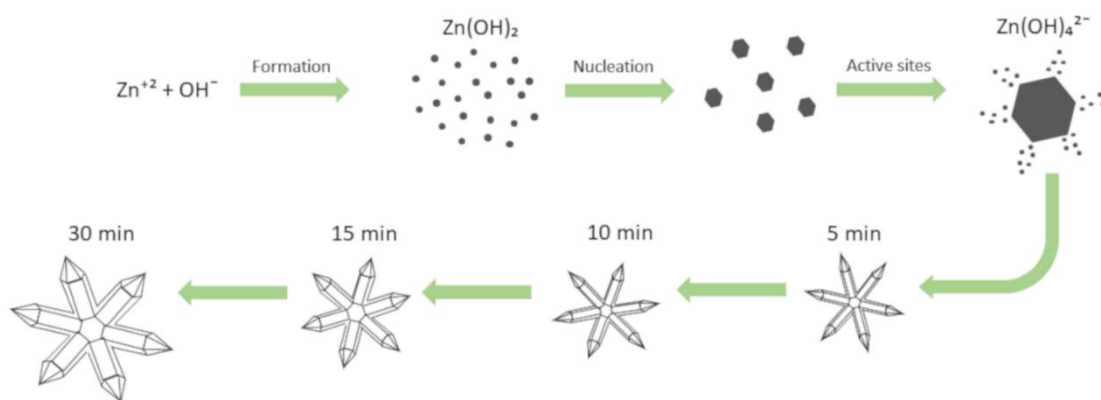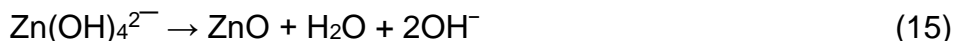
Figure 10. Formation scheme of ZnO nanoflowers.

4.2.3 XRD

The XRD patterns of all the samples synthesized at 140 °C are shown in Fig. 11. As observed, the diffraction peaks of all the samples agree with the JCPDS card 00-036-1451 corresponding to wurtzite (hexagonal) structure. All the patterns exhibit its principal diffraction peaks at 31.7°, 34.4° and 36.2°, corresponding to the (100), (002) and (101) crystallographic planes, respectively. In any pattern we observe diffraction peaks non-corresponding to the wurtzite structure, therefore there are not impurities detectable by XRD analysis. Also, there are not displacements of the peaks, indicating there are not distortions in the crystalline structure [92]. Nonetheless, the pattern of the sample synthesized for 5 min exhibits wider peaks than the others, this is due to its minor size, as confirmed by FE-SEM analysis. Also, the crystallite size of all the samples was obtained through the Scherrer equation (Eq. 7), obtaining a crystallite size of 14.7 nm for the sample synthesized for 5 min, 22.2 nm for the 10 min sample, 24.1 for the 15 min sample, and 24.0 for the 30 min sample. These results indicate that after 15 min of reaction time the crystallite growth stops, and they corroborate the minor crystallite size predicted for the 5 min sample by the wider peaks in XRD.
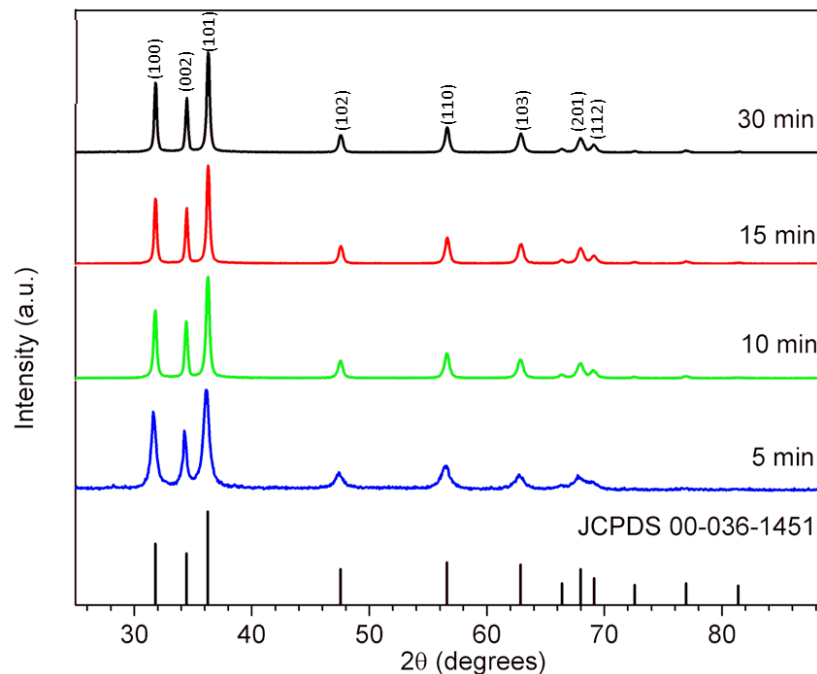
Figure 11. XRD patterns of ZnO nanoflowers synthesized at different times and JCPDS 00-036-1451 correspondent to wurtzite phase. Reproduced from [91] Copyright Elsevier 2019.

4.2.4 DRS

The DRS spectra of all the samples synthesized at 140 °C was obtained (Fig. 12), and its data was used to obtain the optical band gap energy. In the Fig. 13 are observed the Tauc plots $(ahv)^2$ vs hv calculated through the Kubelka-Munk function (Eq. 8). The graphs shown in Fig. 13 have been normalized for better visualization, and the factors used are indicated in the inset.
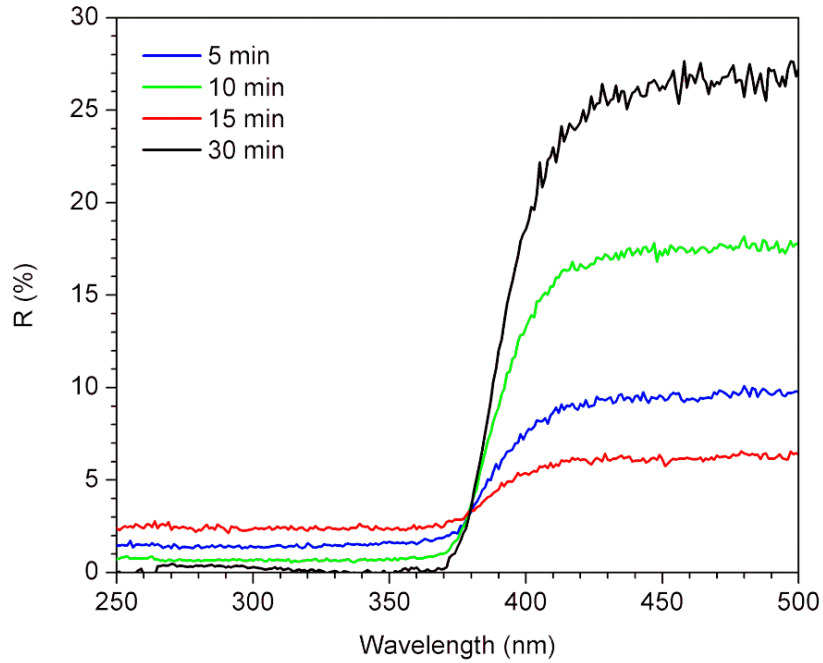
Figure 12. DRS spectra of ZnO nanoflowers synthesized at different times.
Adapted from [91] Copyright Elsevier 2019.
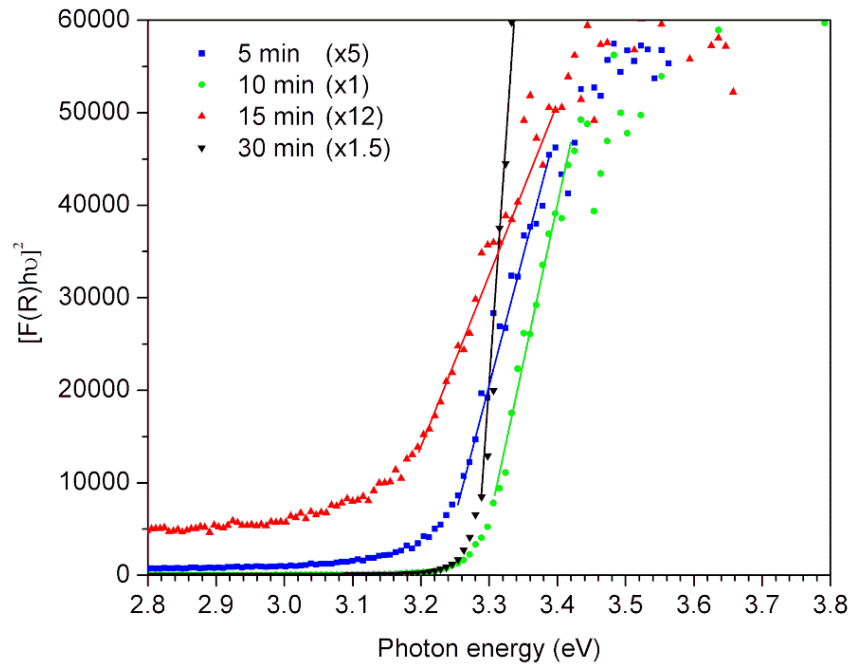
Figure 13. Tauc plots of ZnO nanoflowers synthesized at different times
multiplied by a specific factor (shown in the inset) to normalize. Adapted from [91]
Copyright Elsevier 2019.

The optical band gaps of the ZnO nanoflowers varies between 3.10 to 3.28 eV, which is different from the value reported for bulk ZnO (3.37 eV) [93], nonetheless, the reported optical band gaps for ZnO nanostructures most of the times are minor to the value reported for bulk structures [94]. The variation in the band gap energy of ZnO nanostructures has been attributed to crystallographic defects, such as oxygen vacancies, zinc interstitial sites and dislocations, also to doping and even quantum confinement effects [95]. In our case, the variation in the band gap energy cannot be attributed to quantum confinement effects, since the material dimensions are bigger than the radius of Wannier-Mott exciton for the ZnO (2.34 nm) [95], nor to doping elements, so the narrowing could be attributed to oxygen vacancies.

4.2.5 Four-point probe

Since only one ZnO nanoflower had to be chosen for the DSSC assembly, it was decided to perform an electrical characterization to decide which one to use. The selected method was four-point probe to obtain the sheet resistance of an electrode composed of each sample. The one with the minor sheet resistance would be the selected. The results are shown in Table 4, and they show a decrease in the sheet resistance along the reaction time, going from 38.5 to 0.00344 MΩ/sq from 5 to 30 min respectively. As it is known, the n-type conductivity of ZnO is due to its practically unavoidable point defects. Even the smallest quantity of defects, such as oxygen vacancies or interstitial sites of zinc, alter the carrier-hole equilibrium, thus affecting the conductivity. The decrease in the sheet resistance

could be attributed to a better crystallinity as the reaction time goes on, a smaller quantity of point defects altogether with a bigger crystallite size, which agrees with the XRD results.

Therefore, the ZnO nanoflower synthesized for 30 min was chosen for further experiments, although its reaction time is not the shortest, it presents the desired properties for its application in a DSSC.

Table 4. Dimensions, band gap energy and sheet resistance of ZnO nanoflowers synthesized at different times.

Reaction time (min)	Crystallite size (nm)	Petal width (nm)	Petal length (nm)	Flower length (nm)	Band gap energy (eV)	Sheet resistance (MΩ/sq)
5	14.7	288 ± 27	714 ± 81	1523 ± 151	3.21	38.5
10	22.2	345 ± 45	740 ± 90	1674 ± 180	3.27	18.5
15	24.1	327 ± 48	772 ± 57	1653 ± 154	3.10	0.0102
30	24.0	370 ± 50	772 ± 85	1785 ± 150	3.28	0.00344

4.3 ZnO nanoflowers decoration with Au nanoparticles

Three methods of decoration of the ZnO nanoflowers with Au nanoparticles were tested; decoration by impregnation and synthesis *in situ* of the Au nanoparticles in ZnO nanoflowers using the Monowave 50 and in hot plate.

The first method tested was the impregnation one. For this method the Au nanoparticles were synthesized by citrate reduction method, and its UV-Vis spectrum is shown in Fig. 14. The UV-Vis spectrum is characteristic of Au nanoparticles with a diameter of 40 nm, and the wide band is due to the nanometric size of the particles [96]. To decorate the ZnO nanoflowers an specific quantity of

ZnO was mixed with a certain quantity of the Au nanoparticles, and the dispersion was stirred for 4 h, as further explained in the methodology chapter.
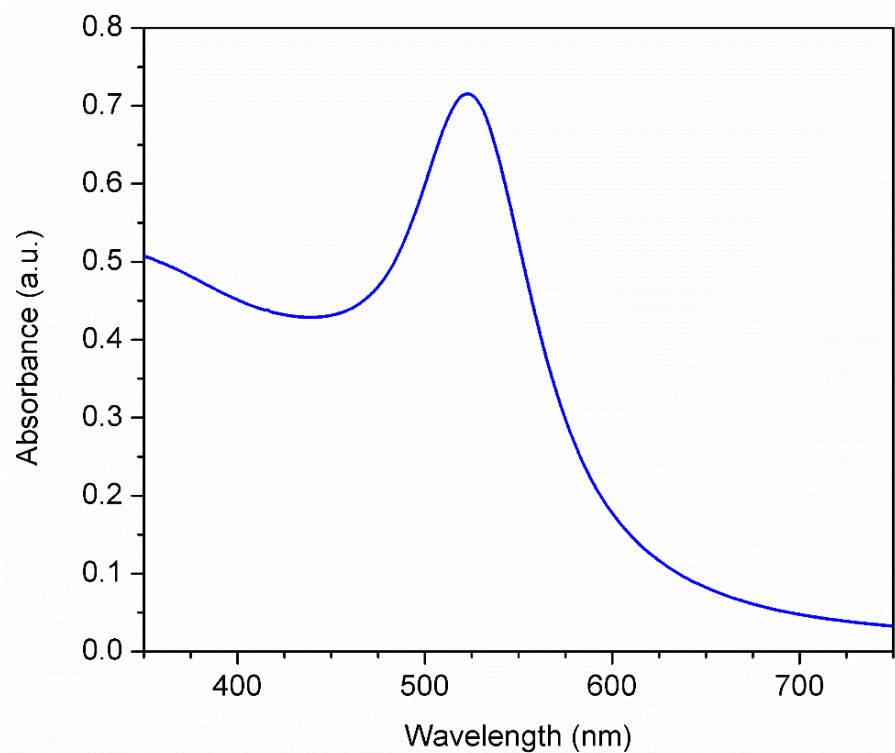
Figure 14. UV-Vis spectrum of Au nanoparticles synthesized by citrate reduction method.

The Fig. 15 shows a photograph of the obtained powder and the remaining solution of Au nanoparticles after the stirring time. As seen in Fig. 15 the powders do not have a strong color, this in an indication that the impregnation method is not highly effective, also the Au nanoparticles solution presents almost the same color it had before the stirring.

Figure 15. Photographs of the ZnO nanoflowers after the stirring in Au nanoparticles solution (left) and Au nanoparticles solution (right).

Therefore, the second and third method were tested. These methods were tested in the conductively heated sealed-vessel reactor (Monowave 50) and in conventional synthesis in hot plate. For the experiment carry out in the reactor the Au nanoparticles adsorption on the ZnO nanoflowers was lower than the conventional synthesis. In the Fig. 16 it is shown the color difference between both experiments, the ZnO nanopowders are precipitated and the liquid is the supernatant. Based on the color difference of the Au nanoparticles solution, it is inferred that with the conventional synthesis the Au nanoparticles are grown onto the surface of the material.

Figure 16. Photographs of the dispersion of ZnO nanoflowers and Au nanoparticles synthesized in the Monowave 50 (left) and in hot plate (right).

As seen in the bottom of the right tube in Fig. 16, the obtained ZnO powders have purple color after the decoration, color given by the wavelength absorption of the LSPR of Au nanoparticles, while the supernatant is colorless. This means that most of the Au nanoparticles are grown in the surface of the ZnO nanoflowers. Even though the color of Au nanoparticles in dispersion goes from red to wine, when absorbed onto the ZnO, the powders do not present the same characteristic color, this phenomenon is due to the dielectric constant of the surrounding media [97].

Since the desired parameter to vary in the DSSC was the percentage of ZnO nanoflowers, not the percentage of Au nanoparticles, and only the ZnO would be decorated with Au nanoparticles, it was decided to vary the quantity of ZnO that was introduced into each *in situ* synthesis of Au nanoparticles. Therefore, the overall quantity of Au nanoparticles would remain similar in the DSSC. Thus, the ZnO nanoflowers meant for the DSSC containing 5% of ZnO/Au, would have more adsorbed Au than the ones meant to the DSSC with 15% of ZnO/Au. These resulting samples were characterized by ICP-AES and EDS.

4.3.1 ICP-AES

To determine the amount of Au nanoparticles grown into the ZnO nanoflowers an ICP-AES analysis was performed. The results showed that as the quantity of ZnO present in the chemical reduction process (synthesis of the Au nanoparticles) increased, the concentration of Au was minor, as expected. Therefore, the results were 12,016 (sample 12A); 10,991 (sample 10A) and 8,366 (sample 8A) mg/Kg (ppm) for the three samples prepared. Since the ZnO/Au nanoparticles were added in 5, 10 and 15% respectively in the DSSC, the final concentration of Au in the DSSC was 601, 1099 and 1255 mg/Kg (ppm), respectively.

4.3.2 FE-SEM/EDS

In the Fig. 17, 18 and 19 are shown high-magnification FE-SEM micrographs for the samples 12A, 10A and 8A, respectively. As expected, the Au nanoparticles are grown into the surface of the ZnO dispersedly without agglomerations. The average diameters of the Au nanoparticles were obtained using ImageJ software,

and the results showed that the particles decreased in size from 26.15 ± 4.74 nm

for the sample 12A, to 17.28 ± 2.83 nm for the 10A sample and 14.12 ± 2.45 nm

for the 8A sample. Besides being smaller, the Au nanoparticles also are present in

minor concentration as observed in the FE-SEM micrographs. The size diminution

is attributed to the larger concentration of ZnO nanoflowers in the synthesis

dispersion, thus the proportion of $HAuCl_4$ is diminished causing smaller and fewer

particles. Due to the LSPR wavelength of the Au nanoparticles, the ZnO/Au

nanoflowers shift their color from white to violet also, and as the quantity of Au

increases also does the color intensity.
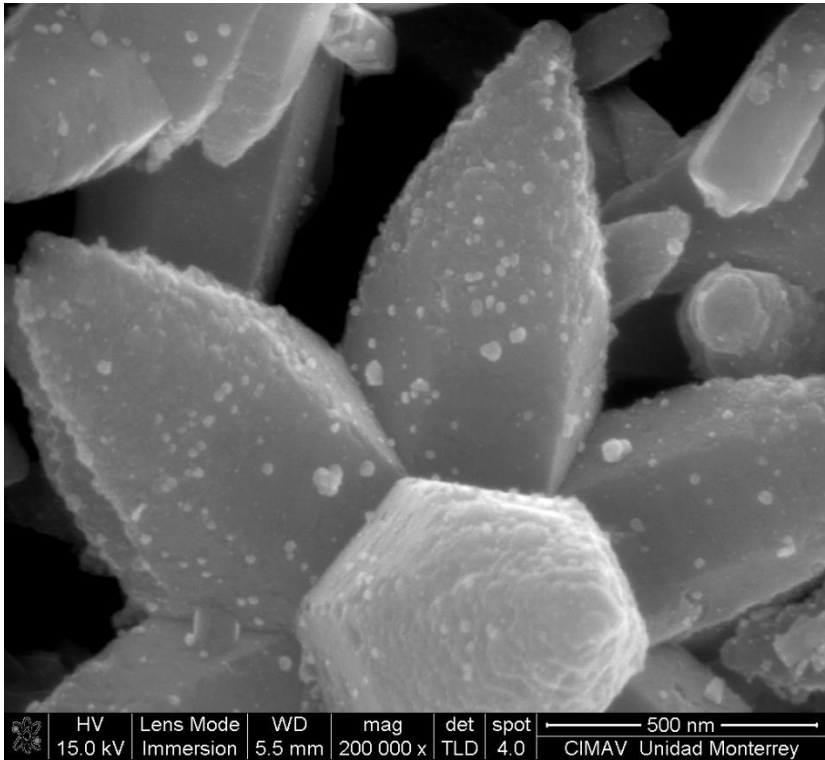
Figure 17. 200,000X FE-SEM micrograph of sample 12A.
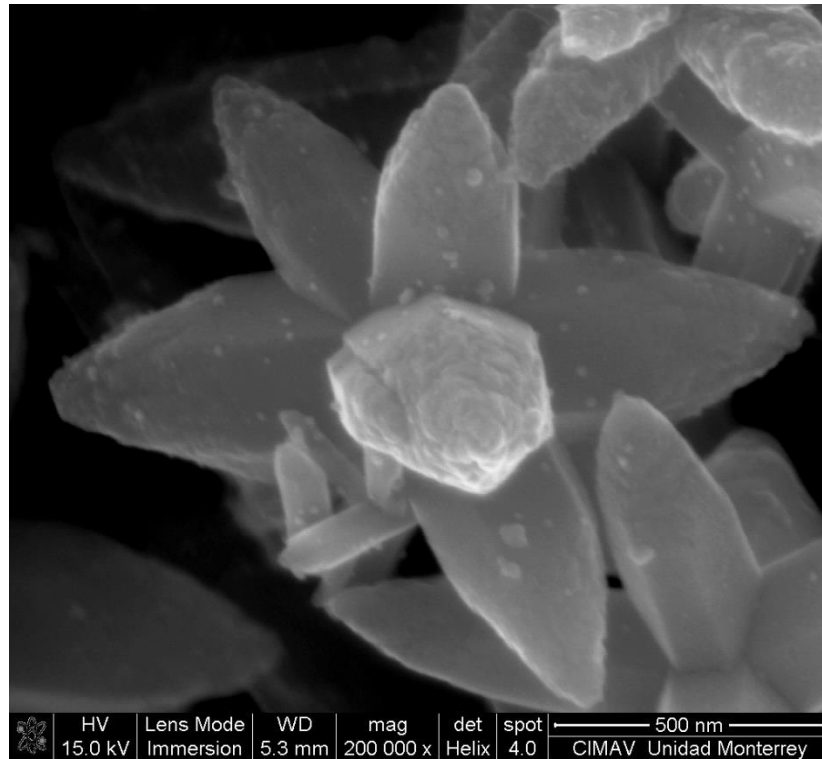
Figure 18. 200,000X FE-SEM micrograph of sample 10A.
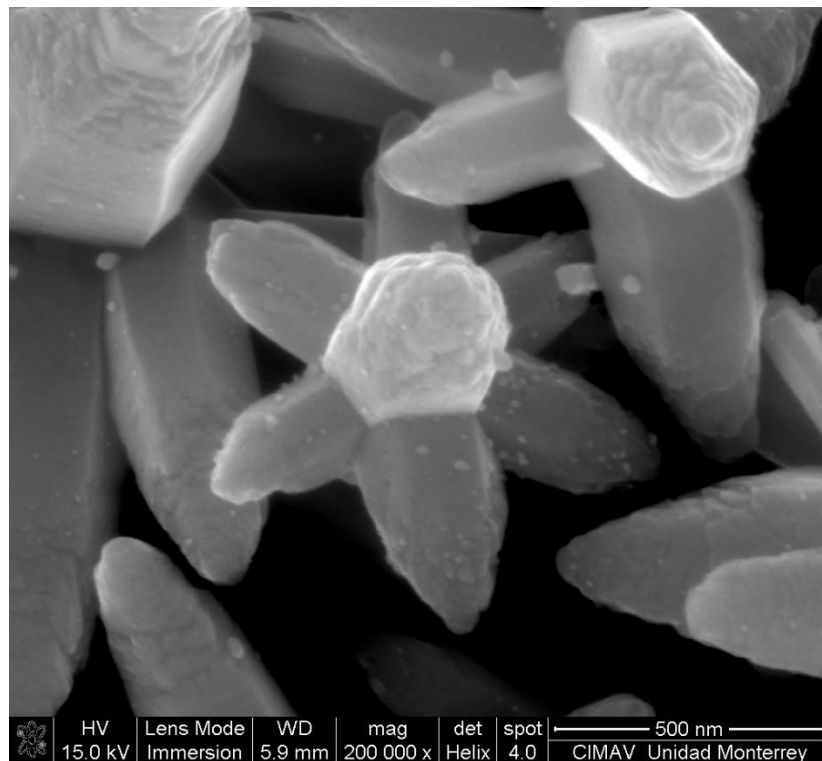
Figure 19. 200,000X FE-SEM micrograph of sample 8A.

In the Fig. 20a, 21a and 22a are shown the high magnification FE-SEM images of the selected area of samples 12A, 10A and 8A for EDS analysis. As seen, all the samples have well distributed Au nanoparticles adsorbed, as confirmed by Au mappings (Fig. 20b, 21b and 22b). As expected, as the quantity of ZnO increases, the quantity of Au nanoparticles decreases, as confirmed by ICP-AES.
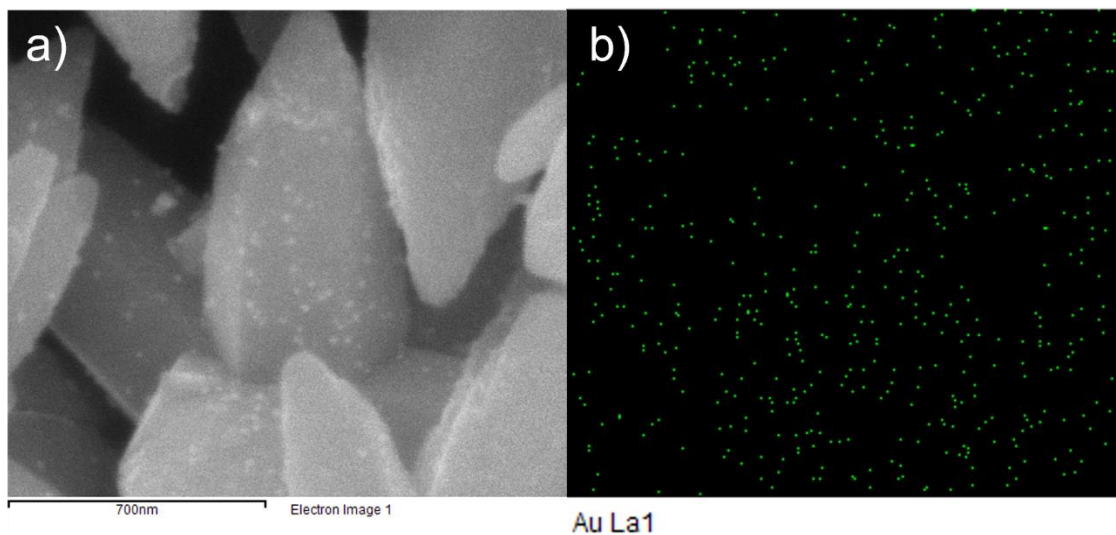
Figure 20. a) Selected area for the EDS analysis and b) Au mapping of sample 12A.
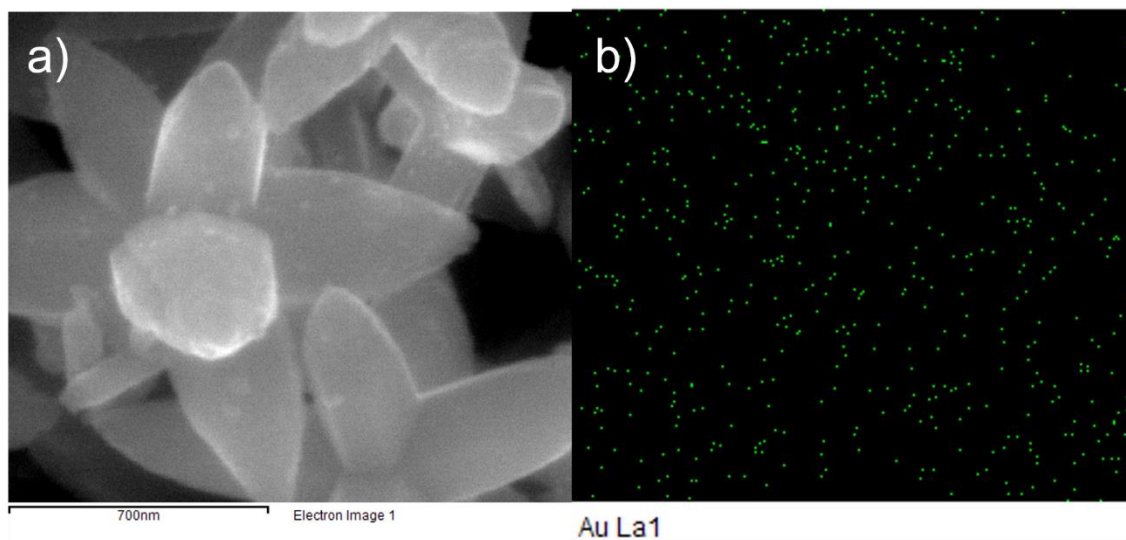
Figure 21 a) Selected area for the EDS analysis and b) Au mapping of sample 10A.
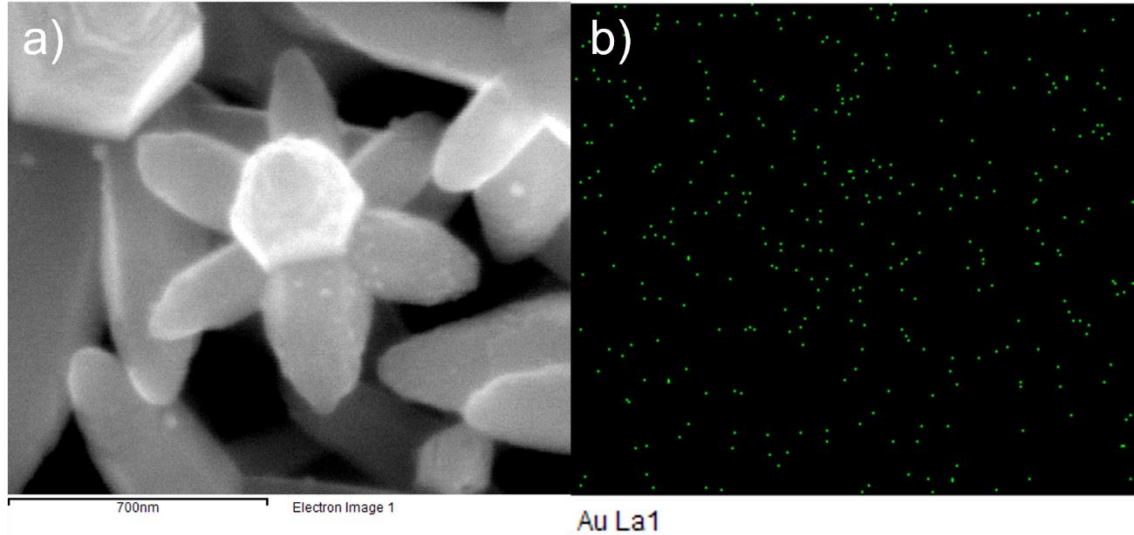
Figure 22. a) Selected area for EDS analysis and b) Au mapping of sample 8A

As observed in the EDS spectra (Fig.23, 24 and 25), the present elements are Zn, O an Au. All the spectra shown the characteristic X-rays energy peaks produced by the elements; Au has the ionization energies of 2.120 eV and 9.712 eV for Lα and Mα respectively, Zn has 8.630 eV and 1.012 eV for Kα and Lα respectively, while O has 0.525 eV for Kα. The atomic percentage results obtained were 0.38, 0.46 and 0.15 for samples 12A, 10A and 8A respectively. But, since the EDS analysis is performed on a specific area of the sample, the atomic percentage results are not reliable.
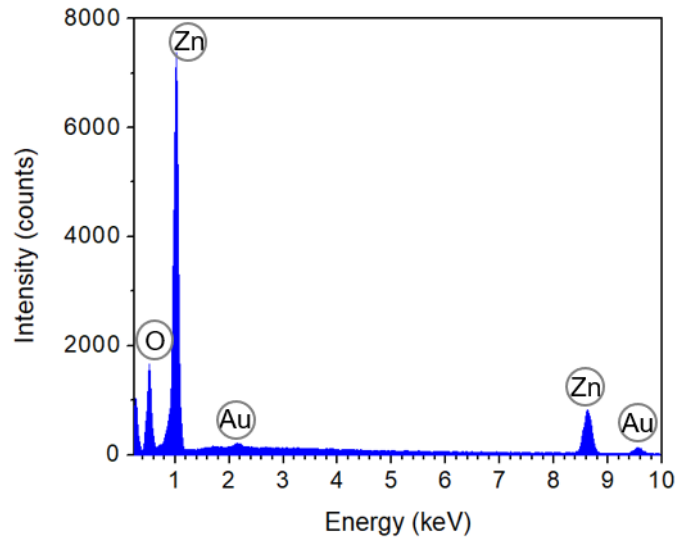
Figure 23. EDS spectrum of sample 12A.
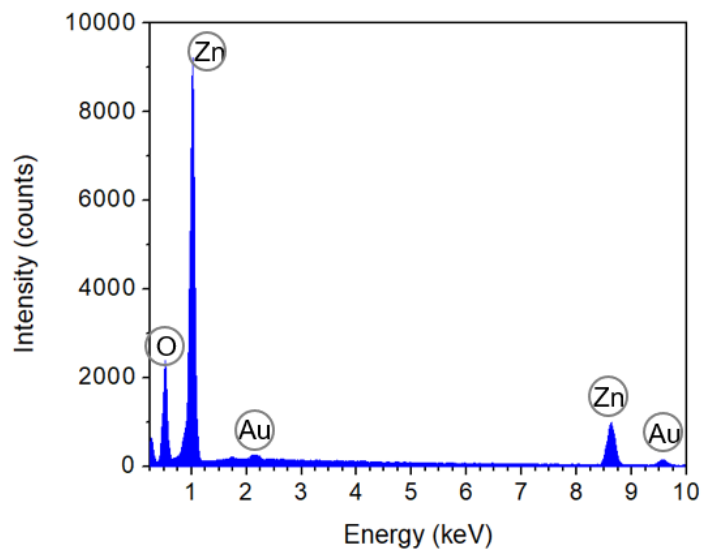
Figure 24. EDS spectrum of sample 10A.

.
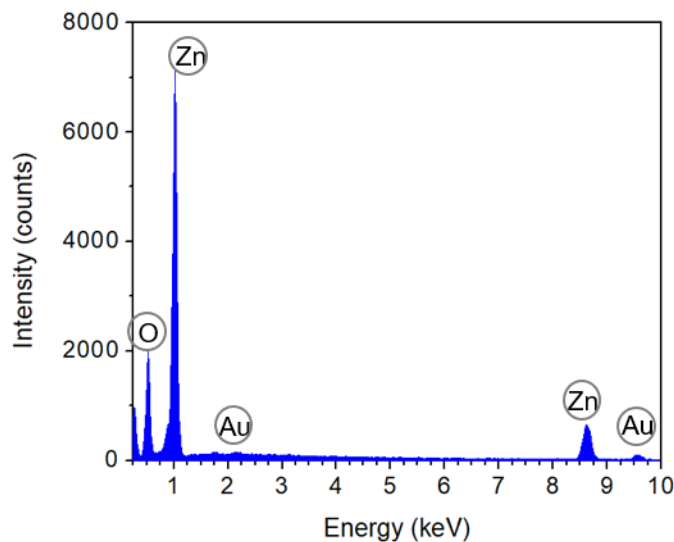
Figure 25. EDS spectra of sample 8A.

4.4 Electrode characterization

4.4.1 Coating thickness

It has been proved that 10-12 μm is the thickness of the semiconductor coating that offers the best DSSC efficiency results [81], thus the thickness of the screen-printed coatings was measured with a mechanical profilometer to obtain a thickness within this range. The results of each sample are presented in Table 5. It can be observed that all the samples are 11 μm thick, nonetheless the screen-printing method does not provide the desired thickness in one layer, so several layers were needed for each sample. The number of layers needed to reach the desired thickness vary for each sample (as shown in Table 5), due to the viscosity of each paste and the pressure applied by the screen-printer. The sample T corresponds to the DSSC with 100% TiO_2, 5Z-95T to the DSSC with 5% ZnO, 10Z-

90T to 10% ZnO and 15Z-85T to 15% ZnO, while the sample 5Z-95T-601A corresponds to the device with 5% of sample 12Au, and so on.

Table 5. Mechanical profilometry results of the electrodes.

Sample	Number of layers deposited	Thickness before thermal treatment (μm)
T	7	11.22 ± 0.23
5Z-95T	7	11.59 ± 0.15
10Z-90T	9	11.20 ± 0.22
15Z-85T	10	11.17 ± 0.18
5Z-95T-601A	8	11.04 ± 0.05
10Z-90T-1099A	10	11.55 ± 0.18
15Z-85T-1255A	10	11.42 ± 0.12

4.4.2 FE-SEM

To investigate the coupling of the materials in the electrode FE-SEM micrographs were obtained. Since the size of the ZnO nanoflowers and the TiO_2 nanoparticles varies from 1.3 μm to 25 nm respectively, we expected to observe ZnO nanoflowers surrounded by nanospheres of TiO_2. We have selected to analyze the electrodes 15Z-85T and 15Z-85T-1255A, whose micrographs are shown in Fig. 26. As observed, the coupling of the materials is as expected, thus providing a direct path for the electrons to travel; and, since the proportion of ZnO is small there are parts of the electrode where the ZnO is not in contact with the TiO_2. Due to the size difference between the structures, the morphology of the ZnO is not affected, therefore maintaining its large superficial area for dye adsorption. In Fig. 27 is shown a high magnification image of the sample T. It is observed that the nanoparticles of TiO_2 are smaller than 25 nm as indicated by the supplier (Sigma Aldrich), however they agglomerate forming larger particles thus

decreasing the available superficial area for dye adsorption. It can also be seen that the deposit is porous due to the thermal treatment where all the organic compounds of the paste are eliminated, this agrees with the reported in literature for these coatings.
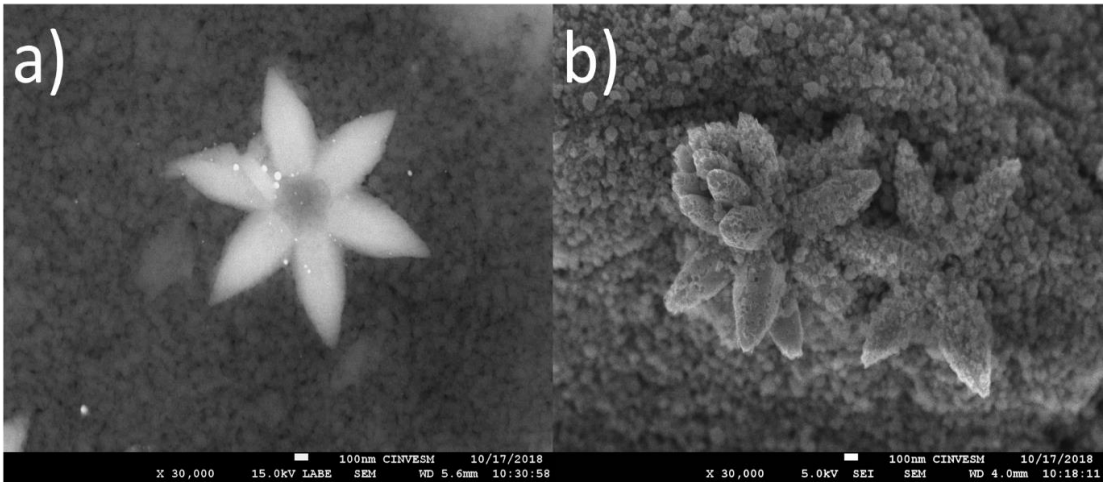
Figure 26. FE-SEM micrographs of the samples a) 15Z-85T-1255A and b) 15Z-85T.
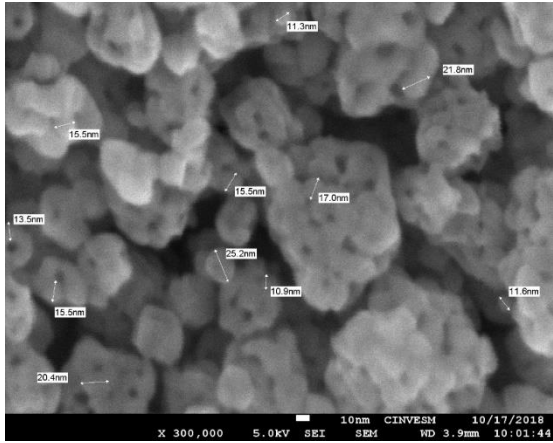
Figure 27. 300,000X FE-SEM micrograph of the sample T.

4.4.3 XRD

Due to the thermal treatment performed to the electrodes, XRD analysis was performed to the samples to confirm that the materials do not change its crystalline phase. In Fig. 28 are presented all the XRD spectra. Since a phase should be present in the material in a percentage larger than 5% to be detected by XRD, the Au nanospheres crystallographic planes would not be detected, therefore only the samples 5Z-95T, 10Z-90T, 15Z-85T and T were analyzed by this technique. In the sample T can be identified the principal diffraction peaks corresponding to the (101), (200) and (105) crystallographic planes in the angles 25.3°, 48.0° and 53.9°, respectively, which correspond with the JCPDS card No. 21-1272 for TiO_2 anatase phase (tetragonal). The mentioned diffraction peaks are present in all the samples. Although they do not present displacements, the ample width of the peaks is attributed to the nanoscale dimensions of the particles. Regarding to the ZnO, in the sample 5Z-95T, its characteristic diffraction peaks cannot be clearly distinguished since its percentage in the sample is in the detection limit, therefore the signals could be lost through the noise. However, in the samples with larger proportion of ZnO the diffraction peaks corresponding to the (100), (002), (101) and (110) crystallographic planes of the wurtzite phase are present (JCPDS card No.00-036-1451) in the angles 31.7°, 34.4°, 36.2° and 56.6°, respectively. Between the samples 10Z-90T and 15Z-85T is observed from the XRD spectra that as the content of ZnO increases its diffraction peaks present a larger intensity, since a longer content of ZnO represents an increased probability of having a diffracted X-ray that can be detected by the equipment. Between 62° and 64° there

are two diffraction peaks that overlap due to its proximity, they correspond to the (204) and (103) crystallographic planes for anatase and wurtzite, respectively.
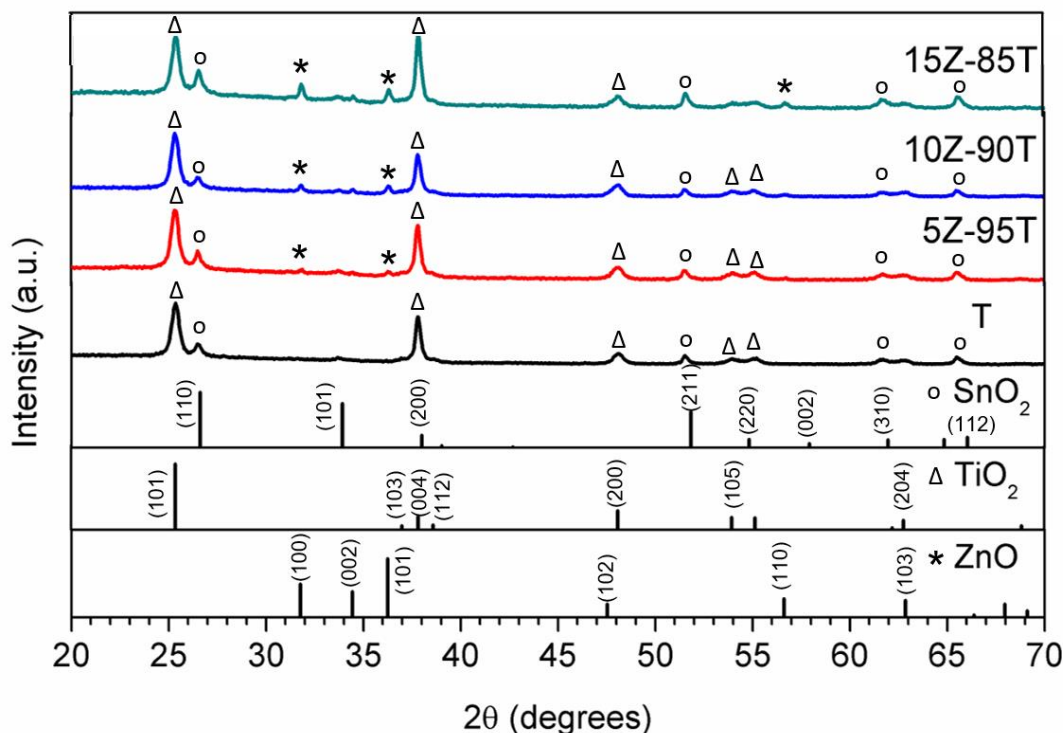
Figure 28. XRD patterns of samples T, 5Z-95T, 10Z-90T and 15Z-85T, and JCPDS card of wurtzite ZnO (JCPDS card No. 00-036-1451) and anatase TiO_2 (JCPDS card No. 21-1272).

Additionally, there are some diffraction peaks that do not agree with any of the patterns. Because the analysis was performed on the electrode, the additional peaks belong to the cassiterite phase (tetragonal) of SnO_2 present in the FTO. In the angles 26.6°, 33.9°, 51.8° and 66.0° are present the signals for the (110), (101), (211) and (301) crystallographic planes of cassiterite, respectively. Furthermore, four diffraction peaks of TiO_2 and SnO_2 are combined due to its proximity; (004) and (200) crystallographic planes in the angle 38°, and (211) and (220) at 55°, corresponding to anatase and cassiterite, respectively.

4.5 DSSC characterization

4.5.1 First set of experiments of DSSC

With the obtention of the J-V curve it is possible to identify the J_{SC} and the V_{OC}. The J_{SC} is defined as the maximum current that can be obtained from the solar cell. It can be found in the y-axis of the J-V curve when the V equals to 0 mV. The V_{OC} represents the maximum voltage given by a solar cell and can be obtained in the x-axis of the J-V curve when the value of J is 0 mA cm^{-2}. With Eq. 9 and 10 is possible to calculate more photovoltaic parameters of the solar cell, as the FF and the efficiency. The FF is a parameter that measures the ideality of a solar cell, the closer it is to 1, the closer the J-V curve is to a perfect square shape and the DSSC is to a better performance. And finally, the efficiency is perhaps the most important photovoltaic parameter, because it represents the relation between the power output of the solar cell and the light power that irradiates it.

After the obtention of the J-V curves and the photovoltaic parameters it was possible to determine the performance of the devices. Even though the V_{OC} significantly increased for all the cells (about 100 mV), as well as the FF, the overall efficiency of the DSSC with ZnO or ZnO/Au nanoflowers decreased, as can be seen in Fig. 29 and Table 6. The increase in V_{OC} could be attributed to the coupling of ZnO and TiO$_2$, due to the high electron mobility in ZnO which facilitates the electron-hole transfer and improves the charge carrier separation [60]. However, the J_{SC} decreases as the content of ZnO increases and it is even more affected by the presence of Au nanoparticles, as seen in the J-V curves (Fig. 29). Even though

ZnO has a larger electron transport mobility its electron injection is not as fast as in TiO2 [98] resulting in decreased J_{SC}. In DSSC the J_{SC} relates to the light harvesting, electron injection and regeneration as well as the electron collection efficiency [10], which depends on the dye used. Furthermore, it is known that ZnO dissolves under acidic conditions due to its solubility product constant (Ksp) $(3.86\text{x}10^{-10})$, like is the ethanolic solution of N719 dye, forming Zn^{2+}-dye complexes, which block the electron transport [99]. Therefore, the use of N719 dye could be the reason of the lower J_{SC} of the devices. Unfortunately, it does not exist yet a commercial sensitizer that is effective for both TiO2 and ZnO but, due to the high performance of devices with N719 dye, it was chosen as sensitizer for the cells. From the J-V curves, the most efficient DSSC is the sample 5Z-95T, even though its counterpart with Au nanoparticles has a larger V_{OC}.
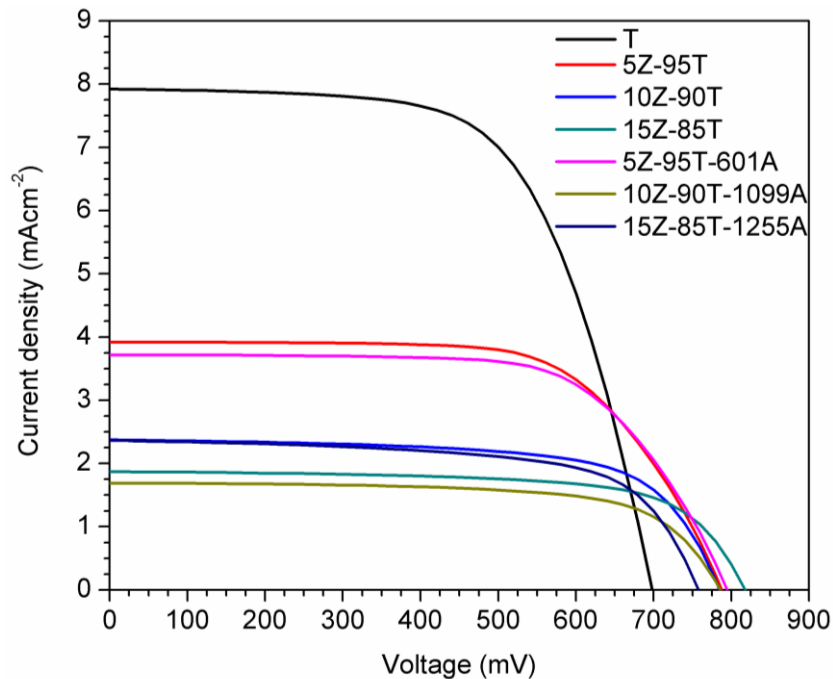
Figure 29. J-V curves of DSSC with different proportions of ZnO or ZnO/Au and TiO2.

Table 6. Photovoltaic parameters of DSSC with different proportions of ZnO or ZnO/Au and TiO$_2$.

Sample	V_{OC} (mV)	J_{SC} (mA cm^{-2})	V_{max} (mV)	J_{max} (mA cm^{-2})	FF	Efficiency (%)
T	706.61 ± 11.52	7.20 ± 0.67	506.89 ± 11.54	6.15 ± 0.73	0.61 ± 0.01	3.12 ± 0.34
5Z-95T	786.58 ± 41.58	2.86 ± 1.44	600.14 ± 20.06	2.55 ± 1.29	0.68 ± 0.04	1.96 ± 0.08
10Z-90T	799.75 ± 0.01	2.74 ± 1.10	626.70 ± 11.54	2.38 ± 1.01	0.68 ± 0.02	1.49 ± 0.61
15Z-85T	819.76 ± 0.01	2.12 ± 0.35	660.00 ± 0.01	1.82 ± 0.34	0.69 ± 0.01	1.20 ± 0.22
5Z-95T-601A	813.13 ± 11.51	2.91 ± 0.74	626.74 ± 41.52	2.61 ± 0.71	0.69 ± 0.03	1.62 ± 0.33
10Z-90A-1099A	779.82 ± 19.98	1.47 ± 0.26	613.40 ± 11.58	1.20 ± 0.25	0.64 ± 0.02	0.74 ± 0.16
15Z-85T-1255A	773.25 ± 11.55	2.08 ± 0.24	620.13 ± 0.04	1.68 ± 0.16	0.65 ± 0.01	1.04 ± 0.10

To obtain information about the internal processes of the DSSC electrochemical methods were used:

- EIS to obtain the R_{CT}, C_μ, and $T_{1/2}$. The equivalent electrical circuit (shown in Fig. 30) was used in ZView software to simulate the data obtained from the Nyquist plots (Fig. 31). In Fig. 31 the symbols correspond to the experimental data, while the line corresponds to the model data. Once the simulation in ZView gave the values of R_{CT} and C_μ, the $T_{1/2}$ was calculated through the Eq. 11. Commonly, the Nyquist plots have 3 semicircles; the high frequency is related to the charge transfer resistance in the counter electrode (R_{Pt}), the second is related to the recombination resistance at the

interface of the semiconductor and the electrolyte and the C_μ (R_{rec}), and the low frequency is related to the diffusion impedance in the electrolyte (R_d) but in good electrolytes it can be dismissed (as it does in I⁻/I₃⁻), finally the displacement from the origin corresponds to the conductive substrate resistance (R_s) [83].

- IMVS to obtain the $T_{1/2}$ and corroborate the results from EIS, and IMPS to calculate the chemical diffusion coefficient (D_n) with the Eq. 12 and 13, respectively [100].
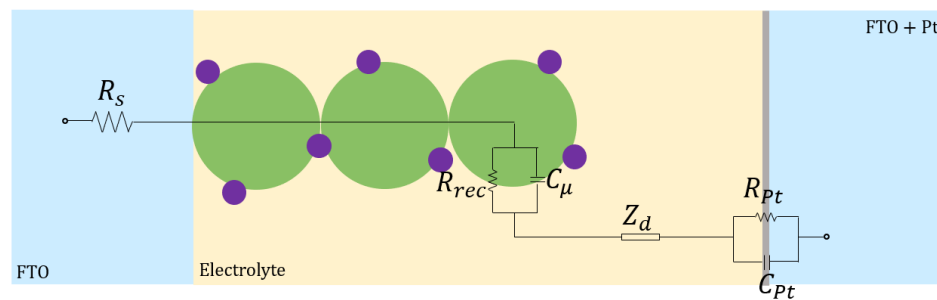
Figure 30. Equivalent electrical circuit used to simulate EIS data in ZView software.
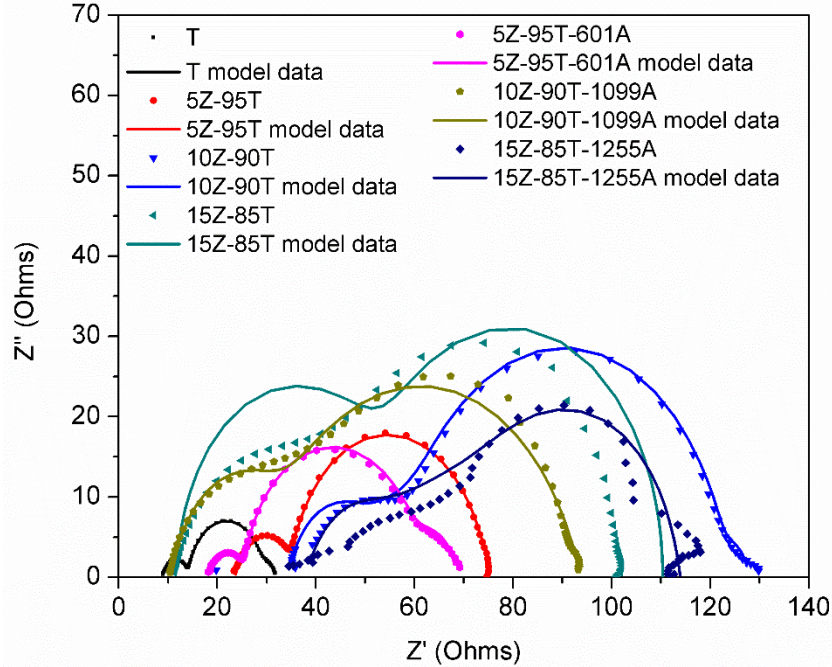
Figure 31. Nyquist plots of DSSC with different proportions of ZnO or ZnO/Au and TiO$_2$.

The EIS measurements were done under 6 different light filters; no filter, 0.1, 0.3, 0.5, 0.6 and 0.9, each one diminishing the DSSC V$_{OC}$. For each cell, 6 different spectra were obtained and the R_{CT}, C_μ and $T_{1/2}$ were obtained for the 6 different V$_{OC}$. Thereafter, the V$_{OC}$ vs. R_{CT}, C_μ and $T_{1/2}$ were graphed to compare the different devices as explained below. In the Fig. 22 are shown the Nyquist plots obtained with no light filter for the samples T, 5Z-95T, 10Z-90T, 15Z-85T, 5Z-95T-601A, 10Z-90T-1099A and 15Z-85T-1255A, and its model data. The Nyquist plots of all the samples obtained under the different light filters are available in the Appendix.

Even though the cell efficiency of the sample T is higher than all the other cells, its R_{CT} is minor as shown in Fig. 32, which indicates it has the highest recombination rate among all the DSSC. As the proportion of ZnO increases, also

68

does the R_{CT}, thus they are more likely to travel through the semiconductor, this means it is more difficult for the electrons to reach the oxidized dye or electrolyte and regenerate them. The enhancement of the R_{CT} could be attributed to the coupling of ZnO and TiO₂ as previously mentioned. Contrary to the efficiency, in the R_{CT} the content of Au nanoparticles is beneficial, since its presence further increases it, although the mechanism of how this happens has not been elucidated yet [101]. Since the C_μ decreases as the ZnO content is increased (Fig. 33), we can assume that ZnO diminishes the presence of surface traps in the oxide layer [50].
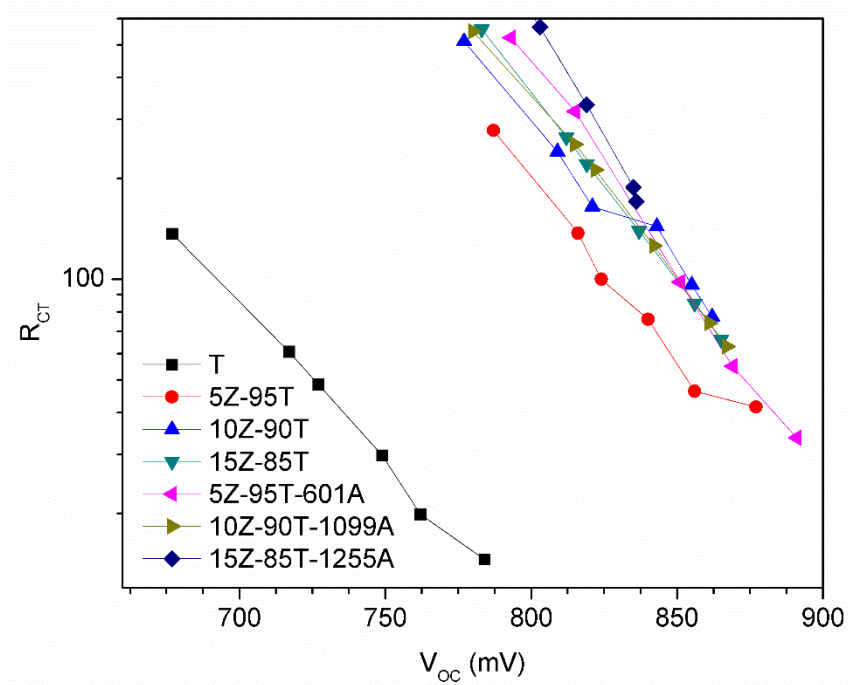
Figure 32. V₀c vs R_{CT} curves for DSSC with different proportions of ZnO or ZnO/Au and TiO₂.
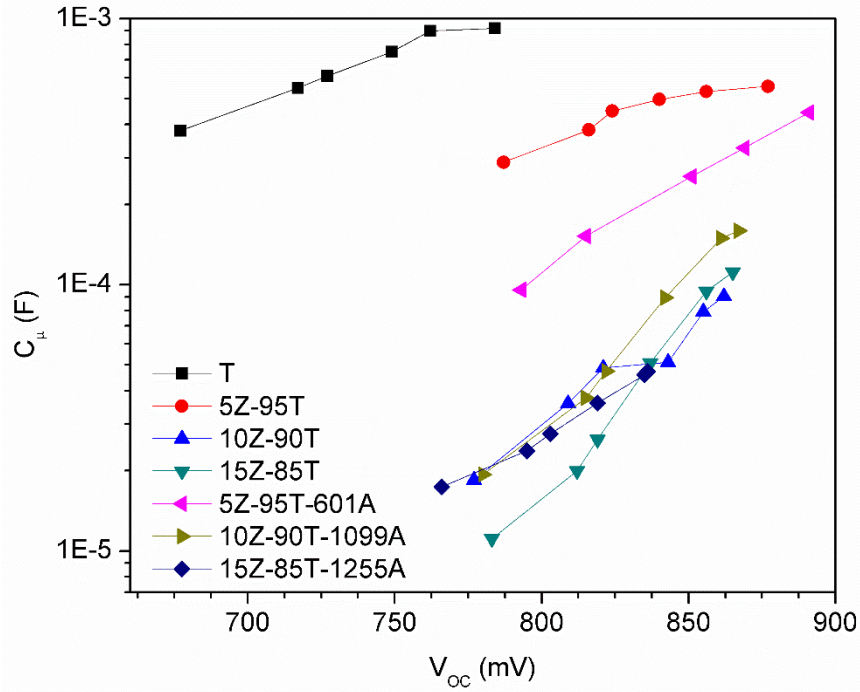
Figure 33. V_{OC} vs C_μ curves for DSSC with different proportions of ZnO or ZnO/Au and TiO$_2$.

In Fig. 34 are shown the V_{OC} vs. $T_{1/2}$ curves, whose results agree with those of R_{CT}, since a longer $T_{1/2}$ relates to a minor recombination rate. Unfortunately, in this case no trend is appreciated with the presence of Au nanoparticles. If the trend for T is extended to larger voltages, after 840 mV its $T_{1/2}$ will be minor than all the other cells.
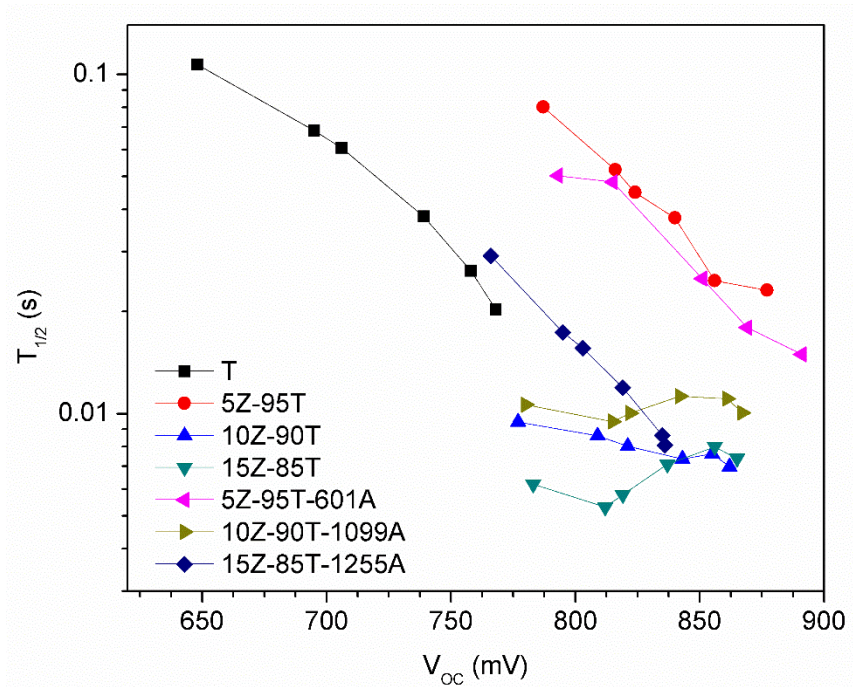
Figure 34. V_{OC} vs $T_{1/2}$ curves obtained by EIS for DSSC with different proportion of ZnO or ZnO/Au and TiO_2.

In Fig. 35 are shown the Nyquist type plots obtained from IMVS for the sample T. Each semicircle represents a measurement taken with a different filter (no filter, 0.1, 0.3, 0.5, 0.6 and 0.9). The value of the top of the arc (w_{max}) is then obtained for each semicircle in ZView software and, the $T_{1/2}$ is calculated with equation 12. Lastly each value of $T_{1/2}$ is plotted and the Fig. 36 is obtained, there different samples can be compared. The values of w_{max} obtained for each sample under different filters, the V_{OC} and the $T_{1/2}$ are shown on Table 7. $T_{1/2}$ from IMVS was calculated to corroborate the results of $T_{1/2}$ obtained from EIS, shown in Fig. 36, obtaining similar results being in both cases the sample 5Z-95T and 5Z-95T-601A the ones with larger $T_{1/2}$.
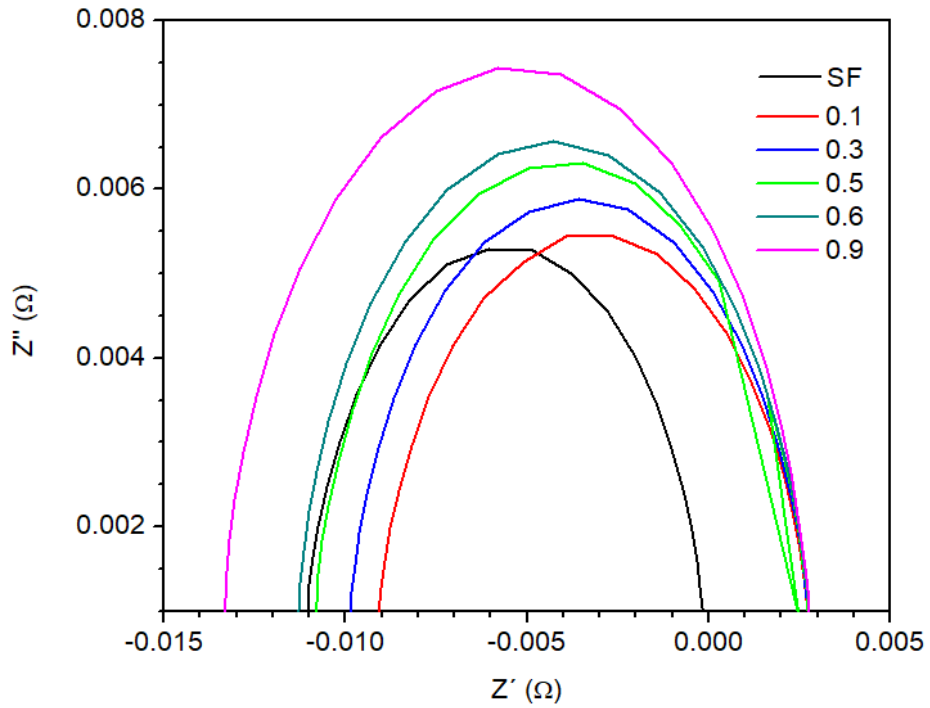
Figure 35. IMVS Nyquist type plots measured at different light filters of sample T.
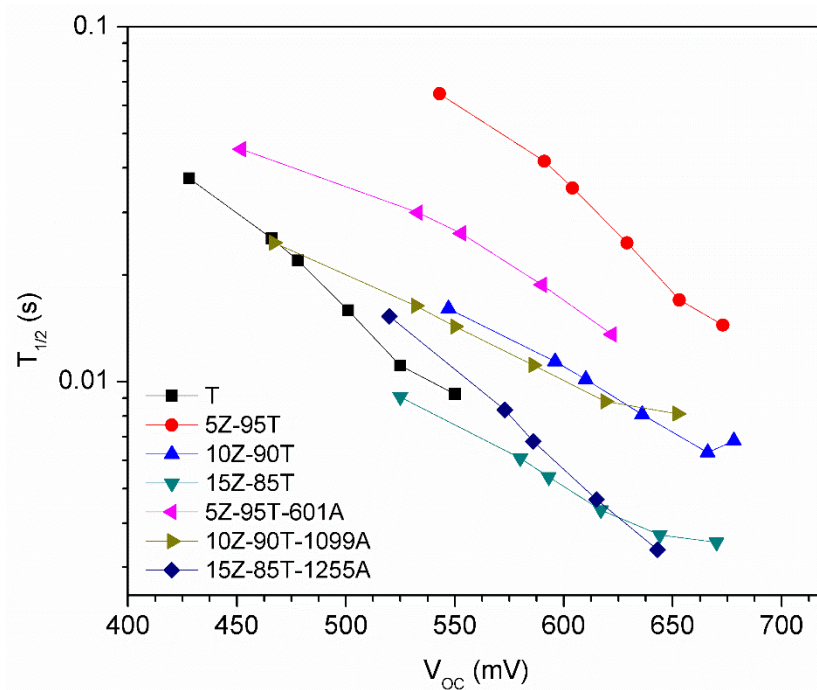
Figure 36. V$_{OC}$ vs $T_{1/2}$ curves obtained by IMVS for DSSC with different proportion of ZnO or ZnO/Au and TiO$_2$.

The same data processing and plotting done for IMVS was followed for IMPS. The obtained IMPS Nyquist type plots for sample T under different light filters are shown in Fig. 37.
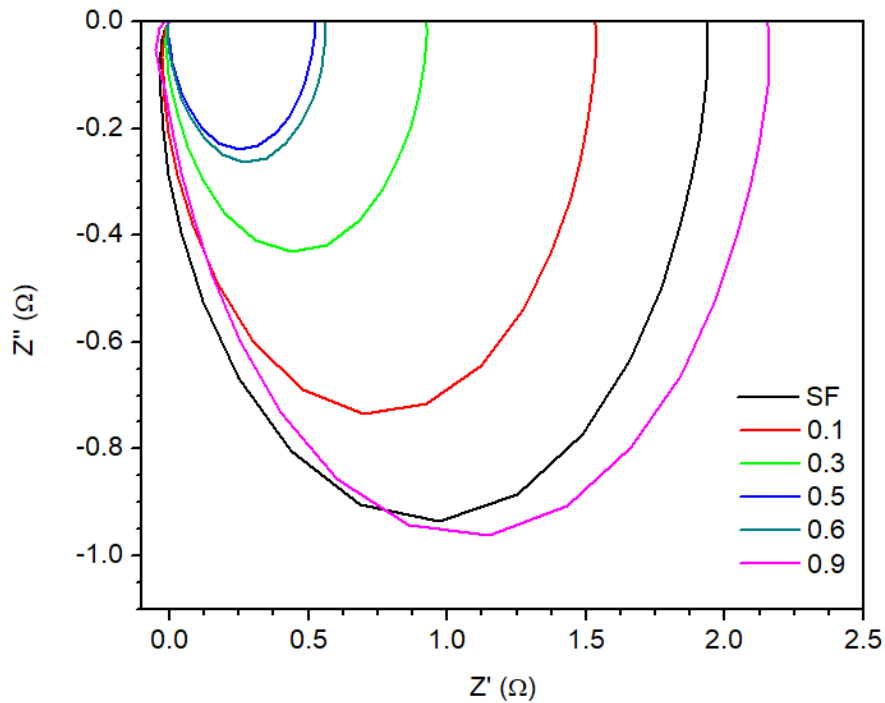
Figure 37. IMPS Nyquist type plots measured under different light filters of sample T.

After w_{max} is obtained in ZView software, the D_n is calculated with the Eq. 13 and the values are graphed against the light intensity. The light intensity values are given by the supplier of the LED used (625 nm) and are always the same for each light filter used. The values of w_{max} and D_n for the DSSC measured under different light filters are displayed on Table 7. Since the D_n obtained by IMVS is related to the electron transport, a larger value is preferred since it translates to an easier

movement. Unfortunately, in Fig. 38 no clear tendency is presented; however, T has one of the largest D_n values.

The larger D_n for sample T could be attributed to the fact that TiO$_2$ nanospheres, especially in anatase phase, favor the electron transport due to its morphology. Thus, when ZnO nanoflowers are incorporated it becomes more difficult for the electrons to travel due to the bigger size of the particles. Furthermore, when Au nanospheres are present the electrons travel with even more difficulty, as seen in the D_n values. This phenomenon could be attributed to the photocharging effect of the Au nanospheres, and since they are present in high quantity its effect is amplified.

Figure 38. Light intensity vs D_n curves for DSSC with different proportions of ZnO or ZnO/Au and TiO$_2$.

Table 7. Data obtained from the IMVS and IMPS spectra for sample T, 5Z-95T, 10Z-90T, 15Z-85T, 5Z-95T-601A, 10Z-90T-1099A and 15Z-85T-1255A.

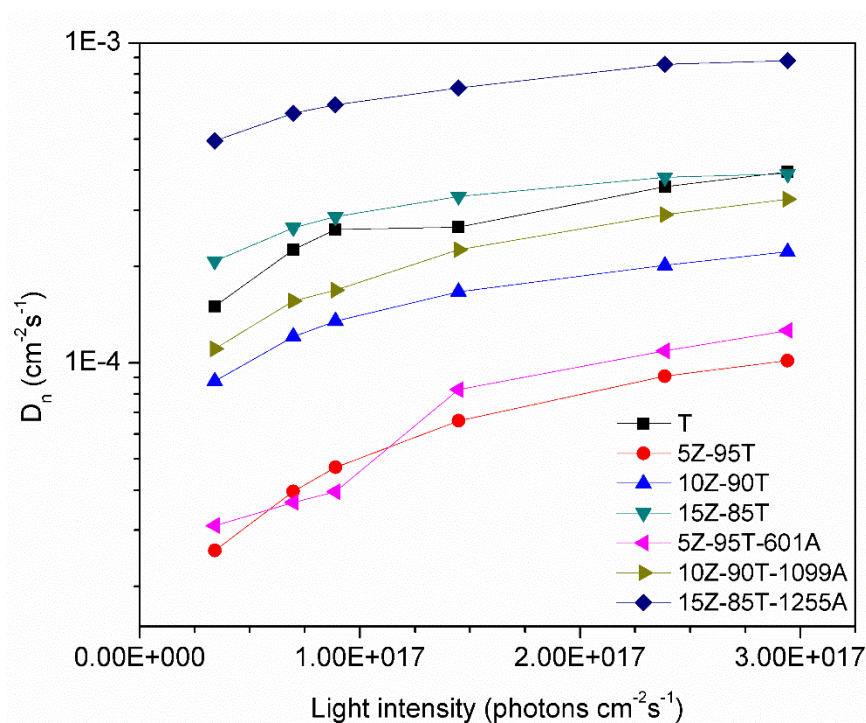| Sample	Filter	IMVS			IMPS	
		V_{OC} (mV)	w_{max} (Hz)	$T_{1/2}$ (s)	w_{max} (Hz)	D_n (cm^{-2} s^{-1})
T	NF	0.550	108.30	0.0092336	760.66	3.96E-04
	0.1	0.525	89.998	0.0111114	682.65	3.55E-04
	0.3	0.501	62.906	0.0158967	510.11	2.66E-04
	0.5	0.478	45.535	0.0219611	501.66	2.61E-04
	0.6	0.466	39.502	0.0253152	433.20	2.25E-04
	0.9	0.428	26.727	0.0374153	288.47	1.50E-04
5Z-95T	NF	0.696	47.595	0.0210106	195.35	1.02E-04
	0.1	0.669	36.554	0.0273568	174.53	9.08E-05
	0.3	0.631	25.460	0.0392773	126.64	6.59E-05
	0.5	0.602	18.311	0.0546120	90.621	4.72E-05
	0.6	0.589	15.856	0.0630676	76.130	3.96E-05
	0.9	0.536	10.661	0.0937998	49.773	2.59E-05
10Z-90T	NF	0.689	135.00	0.0074074	427.29	2.22E-04
	0.1	0.667	119.27	0.0083843	387.95	2.02E-04
	0.3	0.645	93.094	0.0107418	320.50	1.67E-04
	0.5	0.625	73.352	0.0136329	259.59	1.35E-04
	0.6	0.615	66.304	0.0150820	232.19	1.21E-04
	0.9	0.572	49.212	0.0203202	168.50	8.77E-05
15Z-85T	NF	0.670	267.66	0.0037361	748.1	3.89E-04
	0.1	0.644	251.84	0.0039708	730.68	3.80E-04
	0.3	0.617	206.63	0.0048396	636.72	3.31E-04
	0.5	0.593	165.67	0.0060361	550.39	2.86E-04
	0.6	0.580	144.22	0.0069339	508.61	2.65E-04
	0.9	0.525	93.301	0.010718	399.57	2.08E-04
5Z-95T-601A	NF	0.427	84.76	0.011798	242.68	1.26E-04
	0.1	0.622	73.518	0.0136021	209.34	1.09E-04
	0.3	0.590	53.309	0.0187586	158.56	8.25E-05
	0.5	0.553	38.200	0.0261780	76.095	3.96E-05
	0.6	0.533	33.379	0.0299590	70.412	3.67E-05
	0.9	0.452	22.117	0.0452141	59.562	3.10E-05
10Z-90T-1099A	NF	0.652	123.04	0.0081274	623.52	3.25E-04
	0.1	0.619	113.49	0.0088113	558.77	2.91E-04
	0.3	0.586	89.751	0.0111419	433.49	2.26E-04
	0.5	0.550	69.895	0.0143072	324.34	1.69E-04
	0.6	0.532	61.168	0.0163484	300.35	1.56E-04
	0.9	0.467	40.564	0.0246524	212.48	1.11E-04
15Z-85T-1255A	NF	0.632	642.99	0.0015552	1407.8	8.81E-04
	0.1	0.623	568.70	0.0017584	1365.3	8.58E-04
	0.3	0.606	463.58	0.0021571	1205.9	7.24E-04
	0.5	0.584	344.91	0.0028993	1048.5	6.41E-04
	0.6	0.576	278.34	0.0035927	977.91	6.03E-04
	0.9	0.536	166.79	0.0059956	821.89	4.94E-04

Given the results of the experiments, the proposed hypothesis was not accomplished, thus further experiments were performed based on the literature. It has been proven that the beneficial effect of the presence of plasmonic nanoparticles decays as the particles increase in size or in quantity [74]. Its adverse effect had been attributed to the fact that the plasmonic nanoparticles can perform as recombination centers, but recent researches suggest that this phenomenon does not completely explain the decay in performance [101].

4.5.2 Second set of experiments of DSSC

For the second set of experiments the amount of Au was reduced thus, the synthesized ZnO/Au nanoflowers 10A and 8A (Fig. 18 and 19) were used. Hence, in the following comparisons the only varying parameter is the Au content, while the ZnO remains to be 5% in the devices. The devices will be named 5Z-95T-550A and 5Z-95T-418A, being the last digits the quantity of ppm of Au in the electrode.

In the J-V curves shown in Fig. 39, whose data is in Table 8, it can be clearly seen that in samples 5Z-95T-550A and 5Z-95T-418A the presence of Au has a beneficial effect in the V_{OC} and the J_{SC}, both increasing as the amount of Au diminishes. These results agree with those previously reported in the literature [102].

The enhancement in V_{OC} is related to the photocharging effect propitiated by the Au nanospheres, as has been formerly reported [103]. The higher V_{OC} has been attributed to the increased electron density in the nanoparticles, which conducts the Fermi level of the semiconductor to negative potentials. As known, in DSSC

the V_{OC} is determined by the difference between the Fermi level of the semiconductor and the redox level of the electrolyte [15]. While the increase in the J_{SC} could be attributed to the enhanced photon absorption promoted by the plasmons of the Au nanoparticles which increases the dye excitation, as has been reported by some authors [55] [104].
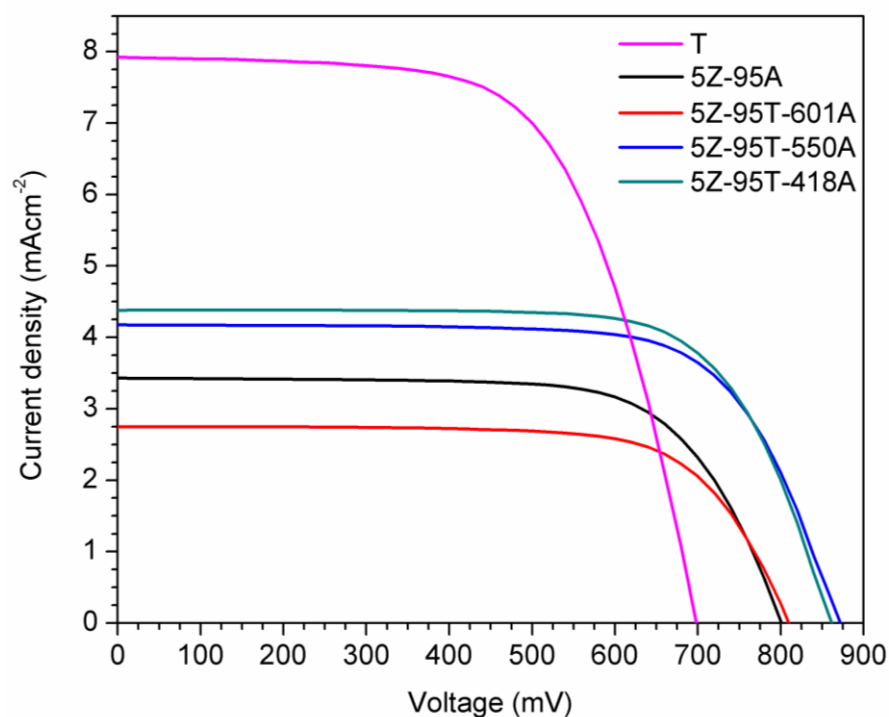
Figure 39. J-V curves for DSSC with 5% of ZnO and different amounts of Au.

Table 8. Photovoltaic parameters of DSSC with 5% of ZnO nanoflowers and different amounts of Au nanoparticles.

Sample	V_{OC} (mV)	J_{SC} (mA cm⁻²)	V_{max} (mV)	J_{max} (mA cm⁻²)	FF	Efficiency (%)
5Z-95T-601A	813.13 ± 11.51	2.91 ± 0.74	626.74 ± 41.52	2.61 ± 0.71	0.69 ± 0.03	1.62 ± 0.33
5Z-95T-550A	839.85 ± 0.03	4.02 ± 0.14	653.39 ± 30.49	3.64 ± 0.13	0.70 ± 0.03	2.38 ± 0.19
5Z-95T-418A	839.69 ± 0.23	4.55 ± 0.43	673.21 ± 11.40	4.15 ± 0.34	0.73 ± 0.01	2.79 ± 0.25

For the second set of DSSC, EIS, IMVS and IMPS were also performed. In Fig. 40 are shown the Nyquist plots for the DSSC with 5% of ZnO and different amounts of Au nanoparticles under no light filter. The Nyquist plots of all the samples collected under the different light filters are available in the Appendix. For IMVS and IMPS, the data obtained from the Nyquist type plots (w_{max}, V_{OC}, $T_{1/2}$ and D_n) are shown in Table 9, and the treatment of the data was the same as the explained in Section 4.5.1. Although the data from sample 5Z-95T and 5Z-95T-601A has been previously displayed, it is shown for comparison with samples 5Z-95T-550A and 5Z-95T-418A.
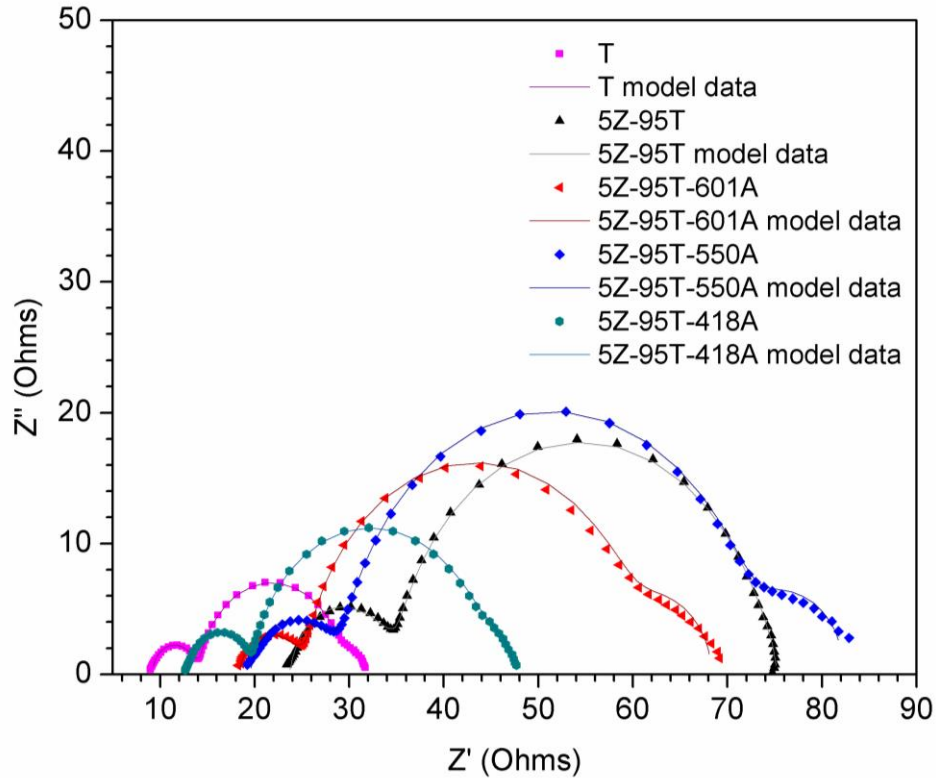
Figure 40. Nyquist plots of DSSC with 5% of ZnO and varying quantity of Au measured under no light filter.

The enhanced performance of the DSSC could also be related to the elimination of surface traps in the semiconductor due to the incorporation of the metallic nanoparticles, hence diminishing the charge recombination. This can be confirmed by the V_{OC} vs R_{CT} curves (Fig. 41) where it can be seen that the sample 5Z-95T-418A has the larger R_{CT} thus agreeing with the other performance results. In this case, the R_{CT} increases as the quantity of Au is reduced, so does the C_{μ} (Fig. 42). Herein, the increase in R_{CT} could be attributed to the presence of Au nanoparticles, if they acted as a recombination center as had been though in the past, no enhancement in the R_{CT} could be observed.

Table 9. Data obtained from the IMVS and IMPS spectra for sample 5Z-95T, 5Z-95T-601A, 5Z-95T-550A and 5Z-95T-418A.

| Sample | Filter | IMVS | | | IMPS | |
		V_{oc} (mV)	w_{max} (Hz)	$T_{1/2}$ (s)	w_{max} (Hz)	D_n (cm^{-2} s^{-1})
5Z-95T	NF	0.696	47.595	0.0210106	195.35	1.02E-04
	0.1	0.669	36.554	0.0273568	174.53	9.08E-05
	0.3	0.631	25.460	0.0392773	126.64	6.59E-05
	0.5	0.602	18.311	0.0546120	90.621	4.72E-05
	0.6	0.589	15.856	0.0630676	76.130	3.96E-05
	0.9	0.536	10.661	0.0937998	49.773	2.59E-05
5Z-95T-601A	NF	0.427	84.760	0.0117980	242.68	1.26E-04
	0.1	0.622	73.518	0.0136021	209.34	1.09E-04
	0.3	0.590	53.309	0.0187586	158.56	8.25E-05
	0.5	0.553	38.200	0.0261780	76.095	3.96E-05
	0.6	0.533	33.379	0.0299590	70.412	3.67E-05
	0.9	0.452	22.117	0.0452141	59.562	3.10E-05
5Z-95T-550A	NF	0.750	89.821	0.0111333	439.48	2.29E-04
	0.1	0.700	78.125	0.0128000	385.86	2.01E-04
	0.3	0.668	57.708	0.0173286	287.84	1.50E-04
	0.5	0.636	43.613	0.0229289	217.47	1.13E-04
	0.6	0.623	38.067	0.0262695	199.45	1.04E-04
	0.9	0.567	27.080	0.0369276	136.17	7.09E-05
5Z-95T-418A	NF	0.718	68.289	0.0146436	549.64	2.86E-04
	0.1	0.694	58.448	0.0171092	499.61	2.60E-04
	0.3	0.670	41.078	0.0243439	370.57	1.93E-04
	0.5	0.644	28.478	0.0351148	267.72	1.39E-04
	0.6	0.633	23.867	0.0418989	227.38	1.18E-04
	0.9	0.579	15.432	0.0648004	147.16	7.66E-05
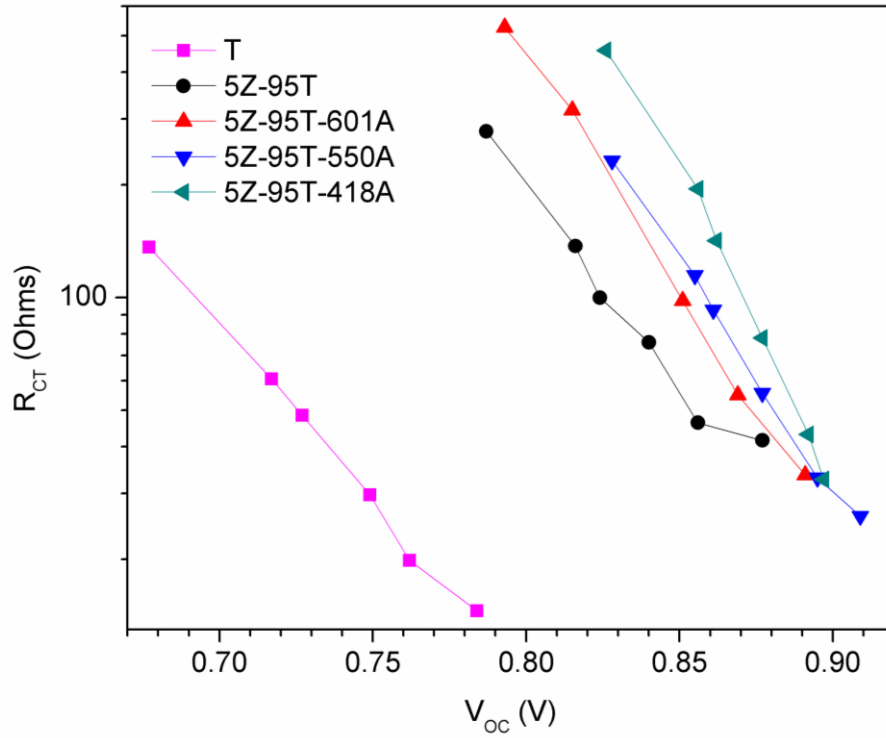
Figure 41. V$_{OC}$ vs R_{CT} curves for DSSC with 5% of ZnO and different amounts of Au.
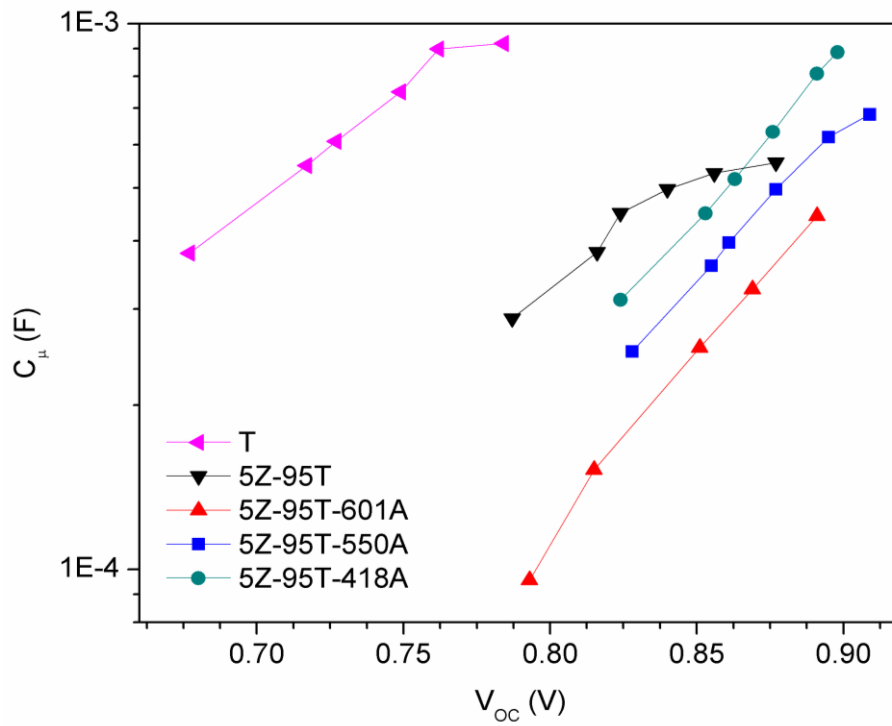
Figure 42. V$_{OC}$ vs C_{μ} curves for DSSC with 5% of ZnO and different amounts of Au nanoparticles.

The results of $T_{1/2}$ obtained by EIS (Fig. 43) and IMVS (Fig. 44) corroborate the results of the R_{CT}. As previously mentioned, a longer $T_{1/2}$ can be translated in a minor recombination rate, because the more the electrons live the more they travel before recombination. Thus, they are more likely to travel and reach the back contact instead of recombining with the oxidized dye or the electrolyte.
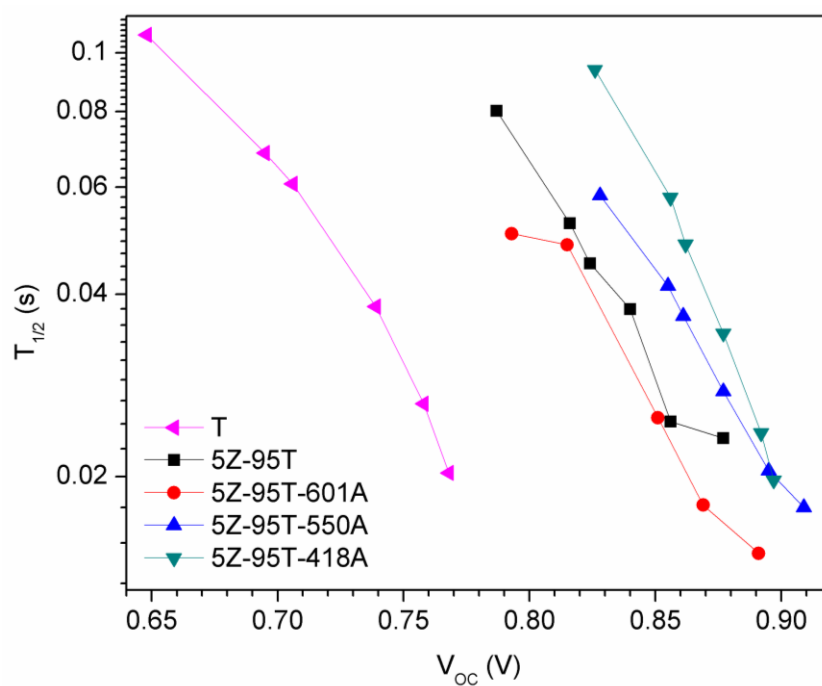
Figure 43. V_{OC} vs $T_{1/2}$ curves obtained by EIS for DSSC with 5% of ZnO and different amounts of Au.
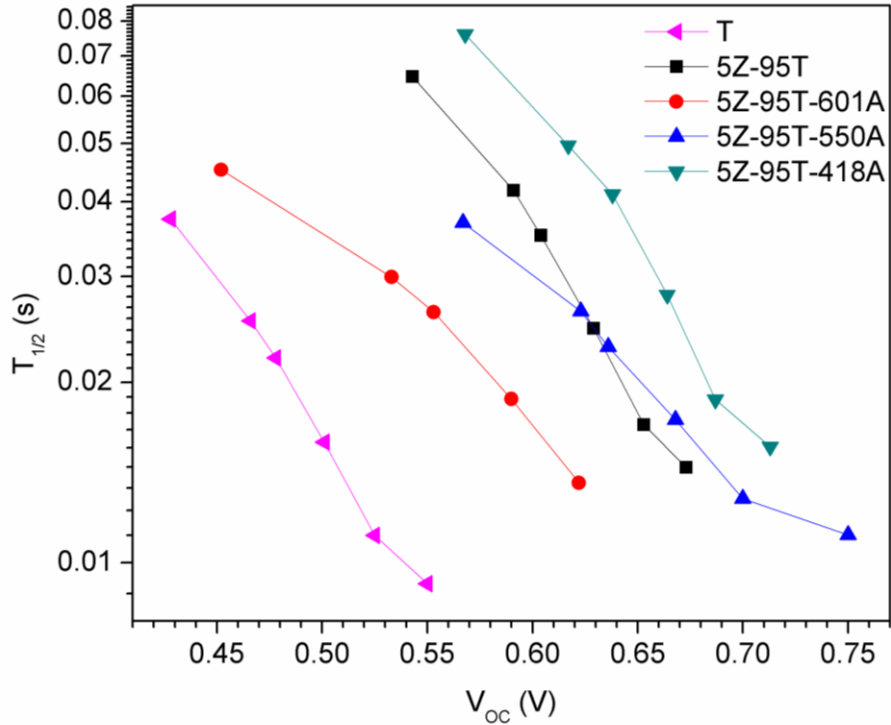
Figure 44. V_{OC} vs $T_{1/2}$ curves obtained by IMVS for DSSC with 5% of ZnO and different amounts of Au.

In Fig. 45 is shown that as the content of Au nanoparticles decreases, the D_n increases, thus agreeing with the efficiency results, R_{CT} and $T_{1/2}$, since a larger D_n is related to an easier electron transport. The enhanced D_n could be attributed to the higher electron density in the semiconductor due to the LSPR propitiated by the Au nanoparticles, since they store electrons (photocharging effect). The variation of D_n in the samples could be explained by the different size and quantity of the Au nanospheres, which alters its absorption wavelength. Therefore, the enhancement in the D_n is further increased as the metallic nanoparticles diminish in size and quantity. Even though, in the first experiments the presence of Au nanoparticles was damaging to the D_n, in these experiments is beneficial. This is

attributed to quantity and size of the particles. As the Au nanoparticles decay in size and quantity its photocharging effect is not as strong, thus they allow more electrons to flow through the semiconductor, instead of storing them.
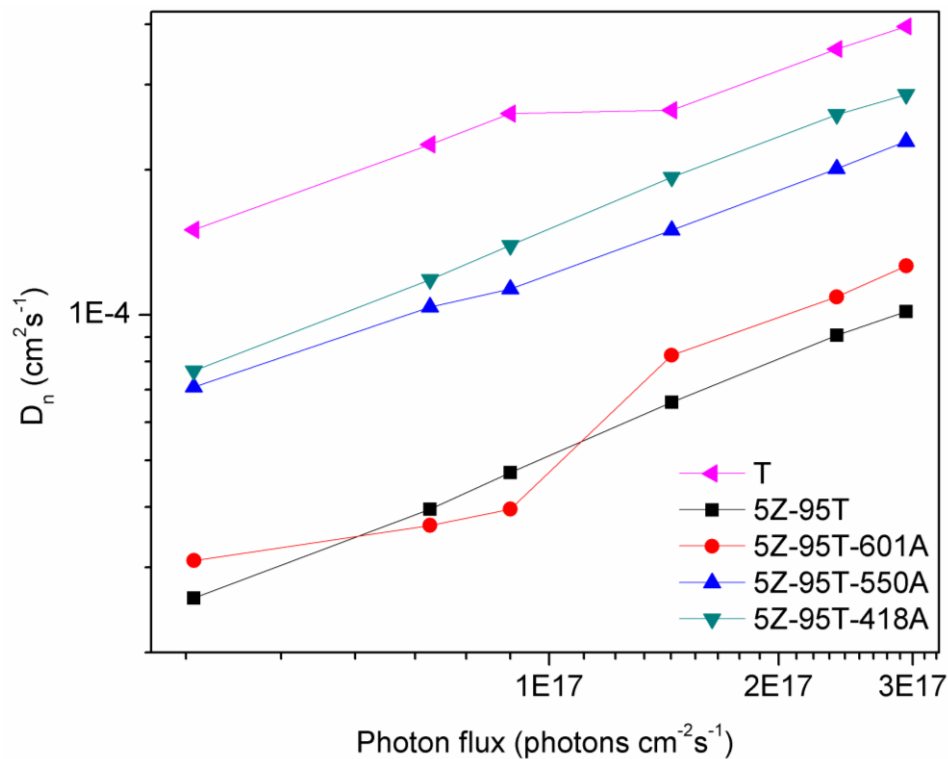
Figure 45. Light intensity vs D_n curves for DSSC with 5% of ZnO and different amounts of Au.

CHAPTER 5

CONCLUSIONS

1. It is possible to hydrothermally synthesize ZnO nanoflowers using a conductively heated sealed-vessel reactor without using additives in shorter times compared to traditional hydrothermal methods.

2. Well-defined ZnO nanoflowers are obtained within 5 min of reaction in a conductively heated sealed-vessel reactor and, as the reaction continues, the rods with pyramidal tips composing the nanostructures continue to grow.

3. The structural characterization demonstrated high crystallinity of hexagonal ZnO (wurtzite) in all the samples without impurities.

4. The electrical characterization results showed that the increase in reaction time allows to obtain a lower sheet resistance, which is a parameter whose desired values can vary according to the application of the material.

5. The coupling of ZnO nanoflowers and TiO_2 nanoparticles in a DSSC increases the V_{OC} in about 100 mV. The enhancement is due to the high

electron mobility in ZnO which facilitates the electron-hole transfer and improves the charge carrier separation, as the same time that increases the R_{CT}.

6. Even though the J_{SC} of the DSSC decreases when compared to a device of TiO$_2$, the most efficient incorporation percentage of ZnO nanoflowers is 5% with 1.96% of efficiency.

7. The enhancement in the devices with Au nanoparticles is due to the increased photon absorption and the photocharging effect promoted by the LSPR of the metallic nanoparticles. Nonetheless, the incorporation of Au nanoparticles is only beneficial in small proportions, the smaller its presence and size, the higher the R_{CT}, $T_{1/2}$ and D$_n$. This is attributed to the stronger photocharging effect that larger, and greater quantity, of Au nanoparticles produce.

8. The most efficient device has 5% of ZnO with 8,366 ppm of Au nanoparticles, obtaining an of efficiency 2.79%, with a J_{SC} of 4.55 mA cm^{-2}, and a V_{OC} of 840 mV. Even though the device does not surpass the performance of a TiO$_2$ DSSC, it is a promising alternative for systems where larger V_{OC} is needed.

9. An optimal dye, that is one that sensitizes ZnO and TiO$_2$ without compromising the chemical stability of none of them, will enhance the J_{SC}. Therefore, a more efficient DSSC would be obtained.

REFERENCES

[1]   J. Wu, Z. Lan, J. Lin, M. Huang, Y. Huang, L. Fan, and G. Luo, "Electrolytes in dye-sensitized solar cells," *Chem. Rev.*, vol. 115, no. 5, pp. 2136–2173, 2015.

[2]   E. Pérez-Denicia, F. Fernández-Lueño, D. Vilariño-Ayala, L. Manuel Montaño-Zetina, and L. Alfonso Maldonado-López, "Renewable energy sources for electricity generation in Mexico: A review," *Renew. Sustain. Energy Rev.*, vol. 78, pp. 597–613, 2017.

[3]   G. Calogero, A. Bartolotta, G. Di Marco, A. Di Carlo, and F. Bonaccorso, "Vegetable-based dye-sensitized solar cells," *Chem. Soc. Rev.*, vol. 44, no. 10, pp. 3244–3294, 2015.

[4]   K. Yoshikawa, H. Kawasaki, W. Yoshida, T. Irie, K. Konishi, K. Nakano, T. Uto, D. Adachi, M. Kanematsu, H. Uzu, and K. Yamamoto, "Silicon heterojunction solar cell with interdigitated back contacts for a photoconversion efficiency over 26%," *Nat. Energy*, vol. 2, no. 5, pp. 17032, 2017.

[5]   V. Fthenakis, "Sustainability of photovoltaics: The case for thin-film solar cells," *Renew. Sustain. Energy Rev.*, vol. 13, no. 9, pp. 2746–2750, 2009.

[6]   M. Ye, X. Wen, M. Wang, J. Iocozzia, N. Zhang, C. Lin, and Z. Ling "Recent advances in dye-sensitized solar cells: From photoanodes, sensitizers and electrolytes to counter electrodes," *Mater. Today*, vol. 18, no. 3, pp. 155–162, 2015.

[7]   S. Sharma, Bulkesh Siwach, S. K. Ghoshal, and D. Mohan, "Dye sensitized solar cells: From genesis to recent drifts," *Renew. Sustain. Energy Rev.*, vol. 70, no. December 2016, pp. 529–537, 2017.

[8]   G. Richhariya, A. Kumar, P. Tekasakul, and B. Gupta, "Natural dyes for dye sensitized solar cell: A review," *Renew. Sustain. Energy Rev.*, vol. 69, no. November 2016, pp. 705–718, 2017.

[9]   A. Shukla and A. Sharma, *Energy security and sustainability*. Taylor and Francis Group, 2017.

[10]   A. K. Chandiran, M. Abdi-Jalebi, M. K. Nazeeruddin, and M. Grätzel,

"Analysis of Electron Transfer Properties of ZnO and TiO$_2$ Photoanodes for Dye-Sensitized Solar Cells," *ACS Nano*, vol. 8, no. 3, pp. 2261–2268, 2014.

[11]   J. Sarkar and S. Bhattacharyya, "Novel improvements in the sensitizers of dye-sensitized solar cells for enhancement in efficiency—a review," *Arch. Thermodyn.*, vol. 33, no. 4, pp. 23–40, 2012.

[12]   C.-P. Lee, R. Y. Y. Lin, L. Y. Lin, C. T. Li, T. C. Chu, S. S. Sun, J. T. and Lin, K. C. Ho, "Recent progress in organic sensitizers for dye-sensitized solar cells," *RSC Adv.*, vol. 5, no. 30, pp. 23810–23825, 2015.

[13]   J. B. Yang, P. Ganesan, J. Teuscher, T. Moehl, Y. J. Kim, C. Y. Yi, P. Comte, K. Pei, T. W. Holcombe, M. K. Nazeeruddin, J. L. Hua, S. M. Zakeeruddin, H. Tian, and M. Gratzel, "Influence of the Donor Size in D-pi-A Organic Dyes for Dye-Sensitized Solar Cells," *J. Am. Chem. Soc.*, vol. 136, no. 15, pp. 5722–5730, 2014.

[14]   Z. Tang, J. Wu, M. Zheng, J. Huo, and Z. Lan, "A microporous platinum counter electrode used in dye-sensitized solar cells," *Nano Energy*, vol. 2, no. 5, pp. 622–627, 2013.

[15]   S. Thomas, T. G. Deepak, G. S. Anjusree, T. A. Arun, S. V. Nair, and A. S. Nair, "A review on counter electrode materials in dye-sensitized solar cells," *J. Mater. Chem. A*, vol. 2, no. 13, pp. 4474–4490, 2014.

[16]   N. Prabavathy, S. Shalini, R. Balasundaraprabhu, D. Velauthapillai, S. Prasanna, and N. Muthukumarasamy, "Enhancement in the photostability of natural dyes for dye-sensitized solar cell (DSSC) applications: a review," *Int. J. Energy Res.*, vol. 41, no. 10, pp. 1372–1396, 2017.

[17]   M. K. Nazeeruddin, E. Baranoff, and M. Grätzel, "Dye-sensitized solar cells: A brief overview," *Sol. Energy*, vol. 85, no. 6, pp. 1172–1178, 2011.

[18]   B. K. Meyer, A. Polity, D. Reppin, and M. Becker, "Binary copper oxide semiconductors: From materials towards devices," *Phys. status solidi*, vol. 249, no. 8, pp. 1487–1509, 2012.

[19]   S. M. Sze and K. K. Ng, *Physics of semiconductor devices*. Wiley-Interscience, 2007.

[20]   M. Grundmann, *Physics of semiconductors : an introduction including nanophysics and applications.* Springer International, 2018.

[21]   Peter T. Landsberg, *Basic properties of semiconductors. North Holland, 1992*.

[22]   K. W. (Karl W. Böer and U. W. Pohl, *Semiconductor physics.* Springer International Publishing, 2018.

[23]   Q. Zhang, C. S. Dandeneau, X. Zhou, and G. Cao, "ZnO Nanostructures ofr Dye-Sensitized Solar Cells," *Adv. Mater.*, vol. 21, no. 41, pp. 4087–

4108, 2009.

[24]   N. Karst, G. Rey, B. Doisneau, H. Roussel, R. Deshayes, V. Consonni, C. Ternon, and D. Bellet., "Fabrication and characterization of a composite ZnO semiconductor as electron transporting layer in dye-sensitized solar cells," *Mater. Sci. Eng. B Solid-State Mater. Adv. Technol.*, vol. 176, no. 8, pp. 653–659, 2011.

[25]   H. J. Snaith and C. Ducati, "SnO_2-Based dye-sensitized hybrid solar cells exhibiting near unity absorbed photon-to-electron conversion efficiency," *Nano Lett.*, vol. 10, no. 4, pp. 1259–1265, 2010.

[26]   J. Z. Ou, R. A. Rani, M. H. Ham, M. R. Field, Y. Zhang, H. Zheng, P. Reece, S. Sriram, M. Bhaskaran, R. B. Kaner, and K. Kalantar-Zadeh, "Elevated temperature anodized Nb_2O_5: A photoanode material with exceptionally large photoconversion efficiencies," *ACS Nano*, vol. 6, no. 5, pp. 4045–4053, 2012.

[27]   R. Vittal and K. C. Ho, "Zinc oxide based dye-sensitized solar cells: A review," *Renew. Sustain. Energy Rev.*, vol. 70, no. November 2016, pp. 920–935, 2017.

[28]   Ü. Özgür, Y. I. Alivov, C. Liu, A. Teke, M. A. Reshchikov, S. Dogan, V. Avrutin, S. J. Cho, and H. Morko, "A comprehensive review of ZnO materials and devices," *J. Appl. Phys.*, vol. 98, no. 4, pp. 1–103, 2005.

[29]   P. V Adhyapak, S. P. Meshram, I. S. Mulla, S. K. Pardeshi, and D. P. Amalnerkar, "Materials Science in Semiconductor Processing Controlled synthesis of zinc oxide nanoflowers by succinate-assisted hydrothermal route and their morphology-dependent photocatalytic performance," *Mater. Sci. Semicond. Process.*, vol. 27, pp. 197–206, 2014.

[30]   X. Zhang, Y. Liu, and Z. Kang, "3D branched ZnO nanowire arrays decorated with plasmonic Au nanoparticles for high-performance photoelectrochemical water splitting," *ACS Appl. Mater. Interfaces*, vol. 6, no. 6, pp. 4480–4489, 2014.

[31]   D. Y. Son, J. H. Im, H. S. Kim, and N. G. Park, "11% Efficient Perovskite Solar Cell Based on ZnO Nanorods: An Effective Charge Collection System," *J. Phys. Chem. C*, vol. 118, no. 30, SI, pp. 16567–16573, 2014.

[32]   S. Baruah and J. Dutta, "Hydrothermal growth of ZnO nanostructures," *Sci. Technol. Adv. Mater.*, vol. 10, no. 1, 2009.

[33]   D. M. Cunha and F. L. Souza, "Facile synthetic route for producing one-dimensional zinc oxide nanoflowers and characterization of their optical properties," *J. Alloys Compd.*, vol. 577, pp. 158–164, 2013.

[34]   S. Pearton and F. Ren, "Advances in ZnO-based materials for light emitting diodes," *Curr. Opin. Chem. Eng.*, vol. 3, pp. 51–55, 2014.

[35]   V. Galstyan, E. Comini, C. Baratto, G. Faglia, and G. Sberveglieri,

"Nanostructured ZnO chemical gas sensors," *Ceram. Int.*, vol. 41, no. 10, pp. 14239–14244, 2015.

[36] A. Tereshchenko, M. Bechelany, R. Viter, V. Khranovskyy, V. Smyntyna, N. Starodub, R. Yakimova, "Optical biosensors based on ZnO nanostructures: advantages and perspectives. A review," *Sensors Actuators B Chem.*, vol. 229, pp. 664–677, 2016.

[37] Y. Wang, X. Li, N. Wang, X. Quan, and Y. Chen, "Controllable synthesis of ZnO nanoflowers and their morphology-dependent photocatalytic activities," *Sep. Purif. Technol.*, vol. 62, no. 3, pp. 727–732, 2008.

[38] D. Yang, Y. Qiu, Q. Jiang, Z. Guo, W. Song, J. Xu, Y. Zong, Q. Feng, and X. Sun, "Patterned growth of ZnO nanowires on flexible substrates for enhanced performance of flexible piezoelectric nanogenerators," *Appl. Phys. Lett.*, vol. 110, no. 6, pp. 63901, 2017.

[39] L. Xu, Y. Guo, Q. Liao and J. Zhang, and D. Xu, "Morphological Control of ZnO Nanostructures by Electrodeposition," J. Phys. Chem. B, 109 (28), pp 13519–13522, 2005.

[40] F. S. Chien, C. R. Wang, Y. L. Chan, H. L. Lin, M. H. Chen, and R. J. Wu, "Fast-response ozone sensor with ZnO nanorods grown by chemical vapor deposition," *Sensors Actuators B Chem.*, vol. 144, no. 1, pp. 120–125, 2010.

[41] Q. Li, Y. Chen, L. Luo, L. Wang, Y. Yu, and L. Zhai, "Photoluminescence and wetting behavior of ZnO nanoparticles/nanorods array synthesized by thermal evaporation," *J. Alloys Compd.*, vol. 560, pp. 156–160, 2013.

[42] J. N. Hasnidawani, H. N. Azlina, H. Norita, N. N. Bonnia, S. Ratim, and E. S. Ali, "Synthesis of ZnO Nanostructures Using Sol-Gel Method," *Procedia Chem.*, vol. 19, pp. 211–216, 2016.

[43] S. Cho, S. H. Jung, and K. H. Lee, "Morphology-Controlled Growth of ZnO Nanostructures Using Microwave Irradiation: from Basic to Complex Structures," *J. Phys. Chem. C*, vol. 112, no. 33, pp. 12769–12776, 2008.

[44] A. Umar, M. S. Akhtar, A. Al-Hajry, M. S. Al-Assiri, and N. Y. Almehbad, "Hydrothermally grown ZnO nanoflowers for environmental remediation and clean energy applications," *Mater. Res. Bull.*, vol. 47, no. 9, pp. 2407–2414, 2012.

[45] B. Ludi and M. Niederberger, "Zinc oxide nanoparticles: chemical mechanisms and classical and non-classical crystallization," *Dalt. Trans.*, vol. 42, no. 35, pp. 12554, 2013.

[46] A. Hezam, K. Namratha, Q. A. Drmosh, B. N. Chandrashekar, K. K. Sadasivuni, Z. H. Yamani, C. Cheng, and K. Byrappa, "Heterogeneous growth mechanism of ZnO nanostructures and the effects of their morphology on optical and photocatalytic properties," *CrystEngComm*, vol.

19, no. 24, pp. 3299–3312, 2017.

[47] H. J. Zhai, W. H. Wu, F. Lu, H. S. Wang, and C. Wang, "Effects of ammonia and cetyltrimethylammonium bromide (CTAB) on morphologies of ZnO nano- and micromaterials under solvothermal process," *Mater. Chem. Phys.*, vol. 112, no. 3, pp. 1024–1028, 2008.

[48] P. Anastas and N. Eghbali, "Green Chemistry: Principles and Practice," *Chem. Soc. Rev.*, vol. 39, no. 1, pp. 301–312, 2010.

[49] D. Obermayer, D. Znidar, G. Glotz, A. Stadler, D. Dallinger, and C. Oliver Kappe, "Design and Performance Validation of a Conductively Heated Sealed-Vessel Reactor for Organic Synthesis," *J. Org. Chem.*, vol. 81, no. 23, pp. 11788–11801, 2016.

[50] F. I. Lizama-Tzec, R. Garcia-Rodriguez, G. Rodriguez-Gatorno, E. J. Canto-Aguilar, A. G. Vega-Poot, B .E. Heredia-Cervera, J. Villanueva-Cab, N. Morales-Flores, U. Pal, G. Oskam, "Influence of morphology on the performance of ZnO-based dye-sensitized solar cells," *RSC Adv.*, vol. 6, no. 44, pp. 37424–37433, 2016.

[51] A. Omar and H. Abdullah, "Electron transport analysis in zinc oxide-based dye-sensitized solar cells: A review," *Renew. Sustain. Energy Rev.*, vol. 31, pp. 149–157, 2014.

[52] R. P. Feynman, "There's plenty of room at the bottom [data storage]," *J. Microelectromechanical Syst.*, vol. 1, no. 1, pp. 60–66, Mar. 1992.

[53] B. Bhushan, *Springer handbook of nanotechnology*. Springer, 2004.

[54] C. Buzea, I. I. Pacheco, and K. Robbie, "Nanomaterials and nanoparticles: Sources and toxicity," *Biointerphases*, vol. 2, no. 4, pp. MR17-MR71, 2007.

[55] H. Elbohy, M. R. Kim, A. Dubey, K. M. Reza, D. L. Ma, J. T. Zai, X. F. Qian, Q. Q. Qiao, "Incorporation of plasmonic Au nanostars into photoanodes for high efficiency dye-sensitized solar cells," *J. Mater. Chem. A*, vol. 4, no. 2, pp. 545–551, 2016.

[56] B. O'Regan and M. Gratzel, "A Low-Cost, High-Efficiency Solar-Cell Based on Dye-Sensitized Colloidal TiO2 Films," *Nature*, vol. 353, no. 6346, pp. 737–740, 1991.

[57] C. Y. Jiang, X. W. Sun, G. Q. Lo, D. L. Kwong, and J. X. Wang, "Improved dye-sensitized solar cells with a ZnO-nanoflower photoanode," *Appl. Phys. Lett.*, vol. 90, no. 26, pp. 2005–2008, 2007.

[58] B. Kilic, T. Günes, I. Besirli, M. Sezginer, and S. Tuzemen, "Construction of 3-dimensional ZnO-nanoflower structures for high quantum and photocurrent efficiency in dye sensitized solar cell," *Appl. Surf. Sci.*, vol. 318, pp. 32–36, 2014.

[59] Y. Wang, Y. Z. Zheng, S. Lu, X. Tao, Y. Che, and J. F. Chen, "Visible-light-

responsive TiO$_2$-coated ZnO:I nanorod array films with enhanced photoelectrochemical and photocatalytic performance," *ACS Appl. Mater. Interfaces*, vol. 7, no. 11, pp. 6093–6101, 2015.

[60]   H. Cai, P. Liang, Z. Hu, L. Shi, X. Yang, J. Sun, N. Xu, and J. Wu, "Enhanced Photoelectrochemical Activity of ZnO-Coated TiO$_2$ Nanotubes and Its Dependence on ZnO Coating Thickness," *Nanoscale Res. Lett.*, vol. 11, no. 1, pp. 1–11, 2016.

[61]   S. Noor, S. Sajjad, S. A. K. Leghari, S. Shaheen, and A. Iqbal, "ZnO/TiO2nanocomposite photoanode as an effective UV-vis responsive dye sensitized solar cell," *Mater. Res. Express*, vol. 5, no. 9, 2018.

[62]   M. I. Khan, M. Saleem, S. U. Rehman, S. S. Ali, and M. U. Qadri, "Stacked Layer Effect of ZnO / TiO$_2$ on the Efficiency of Dye Sensitized Solar Cells," *J. Nanoelectron. Optoelectron*, vol. 13, pp. 1-6, 2018.

[63]   C. Karam, R. Habchi, S. Tingry, P. Miele, and M. Bechelany, "Design of Multilayers of Urchin-like ZnO Nanowires Coated with TiO$_2$ Nanostructures for Dye-Sensitized Solar Cells," *ACS Appl. Nano Mater.*, vol. 1, no. 7, pp. 3705–3714, 2018.

[64]   Z. Chamanzadeh, M. Noormohammadi, and M. Zahedifar, "Enhanced photovoltaic performance of dye sensitized solar cell using TiO$_2$ and ZnO nanoparticles on top of free standing TiO$_2$ nanotube arrays," *Mater. Sci. Semicond. Process.*, vol. 61, pp. 107–113, 2017.

[65]   M. Law, L. E. Greene, A. Radenovic, T. Kuykendall, J. Liphardt, and P. Yang, "ZnO−Al$_2$O$_3$ and ZnO−TiO$_2$ Core−Shell Nanowire Dye-Sensitized Solar Cells," *J. Phys. Chem. B.*, vol. 110, no. 45, pp. 22652-22663, 2006.

[66]   Y. L. Xie, Z. X. Li, Z. G. Xu, and H. L. Zhang, "Preparation of coaxial TiO2/ZnO nanotube arrays for high-efficiency photo-energy conversion applications," *Electrochem. commun.*, vol. 13, no. 8, pp. 788–791, 2011.

[67]   K. M. Lee, E. S. Lee, B. Yoo, and D. H. Shin, "Synthesis of ZnO-decorated TiO2 nanotubes for dye-sensitized solar cells," *Electrochim. Acta*, vol. 109, pp. 181–186, 2013.

[68]   C. S. Chou, F. C. Chou, and J. Y. Kang, "Preparation of ZnO-coated TiO$_2$ electrodes using dip coating and their applications in dye-sensitized solar cells," *Powder Technol.*, vol. 215–216, pp. 38–45, 2012.

[69]   F. Li, Y. Jiao, S. Xie, and J. Li, "Sponge-like porous TiO2/ZnO nanodonuts for high efficiency dye-sensitized solar cells," *J. Power Sources*, vol. 280, pp. 373–378, 2015.

[70]   K. Prabakar, M. Son, W. Y. Kim, and H. Kim, "TiO$_2$ thin film encapsulated ZnO nanorod and nanoflower dye sensitized solar cells," *Mater. Chem. Phys.*, vol. 125, no. 1–2, pp. 12–14, 2011.

[71]   L. Zhao, C. Zhong, Y. Wang, S. Wang, B. Dong, and L. Wan, "Ag

nanoparticle-decorated 3D flower-like TiO_2 hierarchical microstructures composed of ultrathin nanosheets and enhanced photoelectrical conversion properties in dye-sensitized solar cells," *J. Power Sources*, vol. 292, pp. 49–57, 2015.

[72] Q. Xu, F. Liu, Y. Liu, W. Meng, K. Cui, X. Feng, W. Zhang, and Y. Huang, "Aluminum plasmonic nanoparticles enhanced dye sensitized solar cells," *Opt. Express*, vol. 22, no. S2, p. A301, 2014.

[73] S. Muduli, O. Game, V. Dhas, K. Vijayamohanan, K. A. Bogle, N. Valanoor, and S. B. Ogale, "TiO_2-Au plasmonic nanocomposite for enhanced dye-sensitized solar cell (DSSC) performance," *Sol. Energy*, vol. 86, no. 5, pp. 1428–1434, 2012.

[74] N. Chander, A. F. Khan, E. Thouti, S. K. Sardana, P. S. Chandrasekhar, V. Dutta, and V. K. Komarala, "Size and concentration effects of au-nanoparticles on optical and electrical properties of plasmonic dye sensitized solar cells," *Sol. Energy*, vol. 109, pp. 11–23, 2014.

[75] S. P. Lim, A. Pandikumar, N. M. Huang, and H. N. Lim, "Enhanced photovoltaic performance of silver@titania plasmonic photoanode in dye-sensitized solar cells," *RSC Adv.*, vol. 4, no. 72, pp. 38111–38118, 2014.

[76] V. Dhas, S. Muduli, W. Lee, S. H. Han, and S. Ogale, "Enhanced conversion efficiency in dye-sensitized solar cells based on ZnO bifunctional nanoflowers loaded with gold nanoparticles," *Appl. Phys. Lett.*, vol. 93, no. 2008, p. 243108, 2008.

[77] P. Fageria, S. Gangopadhyay, and S. Pande, "Synthesis of ZnO/Au and ZnO/Ag nanoparticles and their photocatalytic application using UV and visible light," *RSC Adv.*, vol. 4, no. 48, pp. 24962–24972, 2014.

[78] S. T. Kochuveedu, J. H. Oh, Y. R. Do, and D. H. Kim, "Surface-plasmon-enhanced band emission of ZnO nanoflowers decorated with Au nanoparticles," *Chem. - A Eur. J.*, vol. 18, no. 24, pp. 7467–7472, 2012.

[79] S. A. Patil, H. J. Hwang, M. Y. Yu, N. K. Shrestha, and H. K. Kim, "Photonic sintering of a ZnO nanosheet photoanode using fl ash white light combined with deep UV," *RSC Advances*, vol. 7, pp. 6565–6573, 2017

[80] K. Sahu and V. V. S. Murty, "Novel sol gel method of synthesis of pure and Aluminium doped TiO_2 nanoparticles useful for dye sensitized solar cell applications," vol. 2, pp. 567–571, 2015.

[81] A. Hagfeldt, G. Boschloo, L. Sun, L. Kloo, and H. Pettersson, "Dye-Sensitized Solar Cells," *J. Photochem. Photobiol. C Photochem. Rev.*, vol. 4, no. 2, pp. 145–153, 2003.

[82] J. Bisquert, F. Fabregat-santiago, I. Mora-Sero, G. Garcia-Belmonte, and S. Gimenez, "Electron Lifetime in Dye sensitized Solar Cells: Theory and Interpretation of Measurements," *J. Phys. Chem. C*, vol. 113, no. 40, pp.

17278–17290, 2009.

[83] F. Fabregat-Santiago, G. Garcia-Belmonte, I. Mora-Seró, and J. Bisquert, "Characterization of nanostructured hybrid and organic solar cells by impedance spectroscopy," *Phys. Chem. Chem. Phys.*, vol. 13, no. 20, pp. 9083–9118, 2011.

[84] R. Gao, Y. Cui, X. Liu, L. Wang, and G. Cao, "A ZnO nanorod/nanoparticle hierarchical structure synthesized through a facile in situ method for dye-sensitized solar cells," *J. Mater. Chem. A*, vol. 2, no. 13, pp. 4765–4770, 2014.

[85] R. Wahab, S.G. Ansari, Y. S. Kim, H. K. Seo, G. S. Kim, G. Khang, and H. S. Shin, "Low temperature solution synthesis and characterization of ZnO nano-flowers," *Mater. Res. Bull.*, vol. 42, no. 9, pp. 1640–1648, 2007.

[86] R. Vinod, P. Sajan, S. R. Achary, C. M. Tomas, V. Muñoz-Sanjosé, and M. J. Bushiri, "Enhanced UV emission from ZnO nanoflowers synthesized by the hydrothermal process," *J. Phys. D. Appl. Phys.*, vol. 45, no. 42, p. 425103, 2012.

[87] J. Fan, T. Li, and H. Heng, "Hydrothermal growth and optical properties of ZnO nanoflowers," *Mater. Res. Express*, vol. 1, no. 4, p. 45024, 2014.

[88] Q. Ahsanulhaq, S. H. Kim, J. H. Kim, and Y. B. Hahn, "Structural properties and growth mechanism of flower-like ZnO structures obtained by simple solution method," *Mater. Res. Bull.*, vol. 43, no. 12, pp. 3483–3489, 2008.

[89] H. Zhang, D. Yang, X. Ma, Y. Ji, J. Xu, and D. Que, "Synthesis of flower-like ZnO nanostructures by an organic-free hydrothermal process," *Nanotechnology*, vol. 15, no. 5, pp. 622–626, 2004.

[90] J. Qiu, X. Li, W. He, S. J. Park, H. K. Kim, Y. H. Hwang, J. H. Lee, and Y. D. Kim, "The growth mechanism and optical properties of ultralong ZnO nanorod arrays with a high aspect ratio by a preheating hydrothermal method," *Nanotechnology*, vol. 20, no. 15, p. 155603, 2009.

[91] S. Borbon, S. Lugo, and I. Lopez, "Fast synthesis of ZnO nanoflowers using a conductively heated sealed-vessel reactor without additives," *Mater. Sci. Semicond. Process.*, vol. 91, pp. 310–315, 2018.

[92] X. Zeng, J. Zhang, and F. Huang, "Optical and magnetic properties of Cr-doped ZnS nanocrystallites," *J. Appl. Phys.*, vol. 111, no. 12, 2012.

[93] A. Janotti and C. G. Van De Walle, "Fundamentals of zinc oxide as a semiconductor," *Reports Prog. Phys.*, vol. 72, no. 12, 2009.

[94] A. Hezam, K. Namratha, Q. A. Drmosh, T. R. Lakshmeesha, S. Srikantaswamy, and K. Byrappa, "The correlation among morphology, oxygen vacancies and properties of ZnO nanoflowers," *J. Mater. Sci. Mater. Electron.*, vol. 29, no. 16, pp. 13551–13560, 2018.

[95] U. Manzoor, M. Islam, L. Tabassam, and S. Ur, "Quantum confinement effect in ZnO nanoparticles synthesized by co- precipitate method," *Phys. E Low-dimensional Syst. Nanostructures*, vol. 41, no. 9, pp. 1669–1672, 2009.

[96] P. N. Njoki, I. S. Lim, D. Mott, H. Y. Park, B. Khan, S. Mishra, R. Sujakumar, J. Luo, and C. J. Zhong, "Size Correlation of Optical and Spectroscopic Properties for Gold Nanoparticles," *J. Phys. Chem. C.*, no. 111, vol. 40, pp. 14664-14669, 2007.

[97] J. Luo, M. M. Maye, L. Han, N. Kariuki, V. W. Jones, Y. Lin, M. H. Engelhard, and C. J. Zhong, "Spectroscopic Characterizations of Molecularly Linked Gold Nanoparticle Assemblies upon Thermal Treatment," *Langmuir*, vol. 20, no. 10, pp. 4254-4260, 2004.

[98] M. Rodríguez-Pérez, E. Canto, R. García-Rodríguez, A. T. De Denko, G. Oskam, and F. E. Osterloh, "Surface Photovoltage Spectroscopy Resolves Interfacial Charge Separation Efficiencies in ZnO Dye-Sensitized Solar Cells," *J. Phys. Chem. C*, vol. 122, no. 5, pp. 2582-2588, 2018.

[99] J. Patwari, S. Shyamal, T. Khan, H. Ghadi, C. Bhattachatya, S. Chakrabarti, and S. K. Pal, "Inversion of activity in DSSC for TiO_2 and ZnO photo-anodes depending on the choice of sensitizer and carrier dynamics," *J. Lumin.*, vol. 207, pp. 169-176, 2018.

[100] J. Halme, "Linking optical and electrical small amplitude perturbation techniques for dynamic performance characterization of dye solar cells," *Phys. Chem. Chem. Phys.*, vol. 13, no. 27, pp. 12435–12446, 2011.

[101] J. Villanueva-Cab, P. Olalde-Velasco, A. Romero-Contreras, Z. Zhuo, F. Pan, S. E. Rodil, W. Yang, and U. Pal. "Photocharging and Band Gap Narrowing Effects on the Performance of Plasmonic Photoelectrodes in Dye-Sensitized Solar Cells," *ACS Appl. Mater. Interfaces*, vol. 10, no. 37, pp. 31374–31383, 2018.

[102] S. P. Ng, X. Lu, N. Ding, C. M. L. Wu, and C. S. Lee, "Plasmonic enhanced dye-sensitized solar cells with self-assembly gold-TiO_2@core-shell nanoislands," *Sol. Energy*, vol. 99, pp. 115–125, 2014.

[103] W. R. Erwin, H. F. Zarick, E. M. Talbert, and R. Bardhan, "Light trapping in mesoporous solar cells with plasmonic nanostructures," *Energy Environ. Sci.*, vol. 9, no. 5, pp. 1577–1601, 2016.

[104] Y. H. Jang, Y. J. Jang, S. T. Kochuveedu, M. Byun, Z. Lin, and D. H. Kim, "Plasmonic dye-sensitized solar cells incorporated with Au-TiO_2 nanostructures with tailored configurations.," *Nanoscale*, vol. 6, no. 3, pp. 1823–32, 2014.

APPENDIX
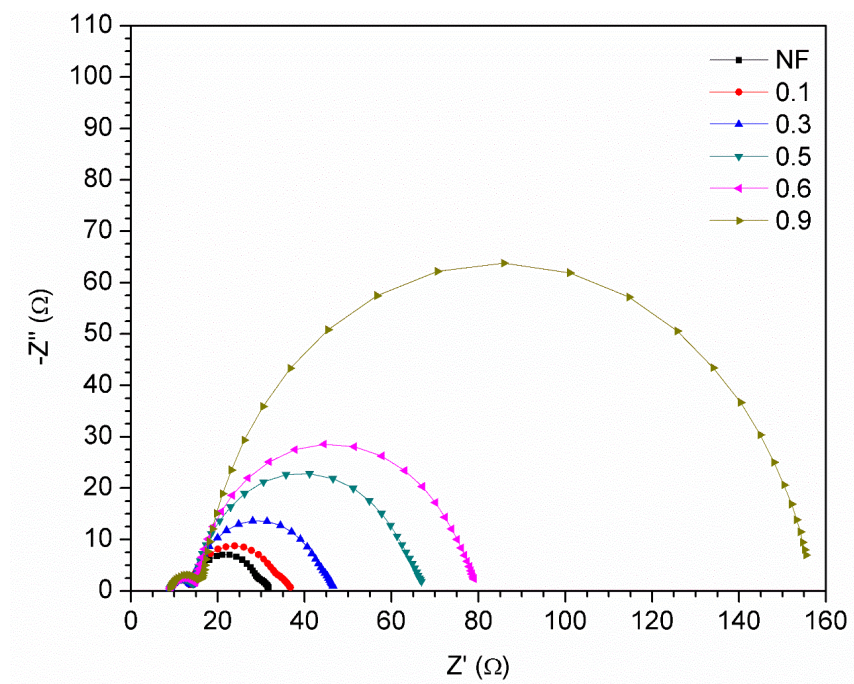
Nyquist plots

APPENDIX

Nyquist plots

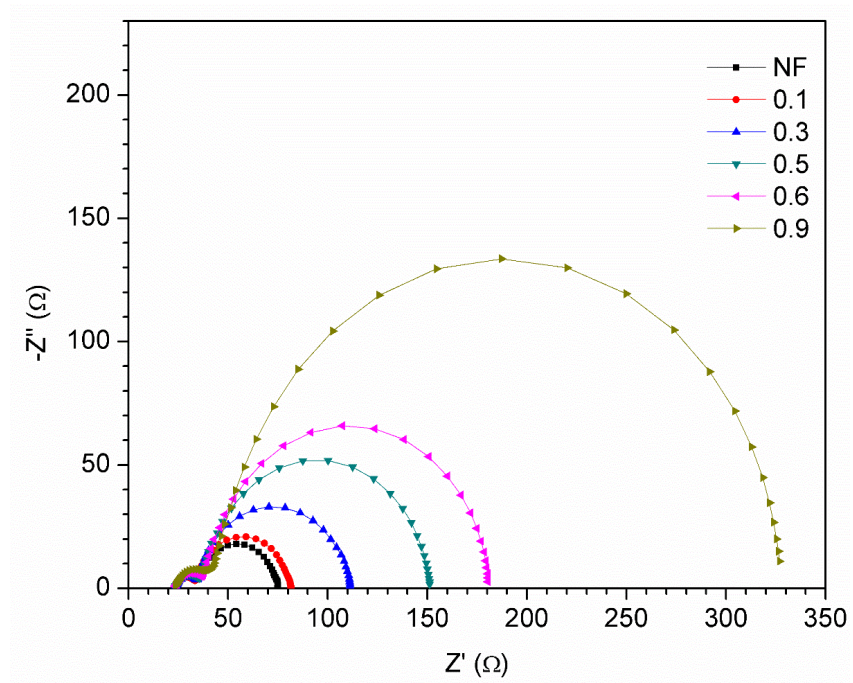Figure 46. Nyquist plots of sample T measured under different light intensities.

Figure 47. Nyquist plots of sample 5Z measured under different light intensities.
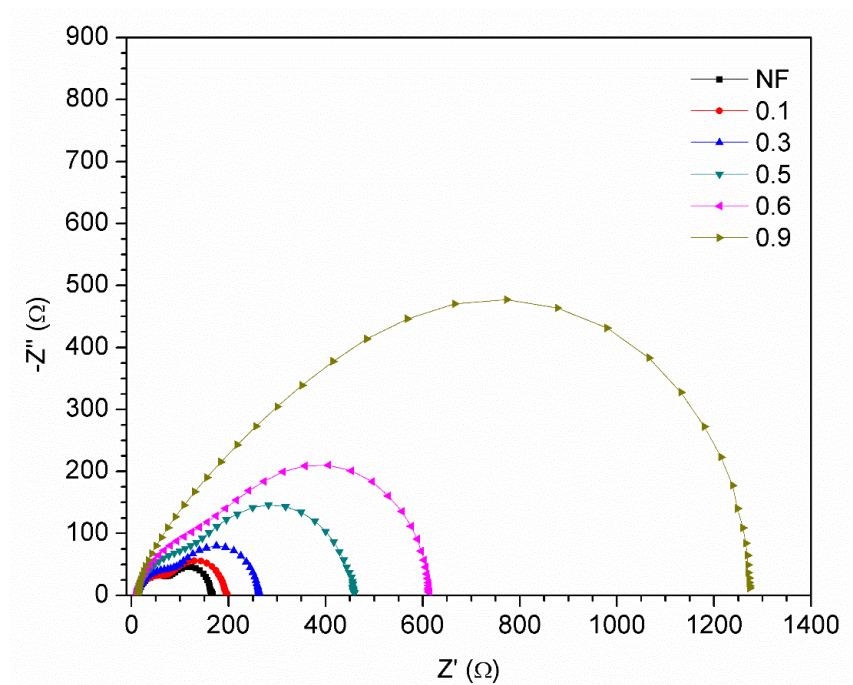

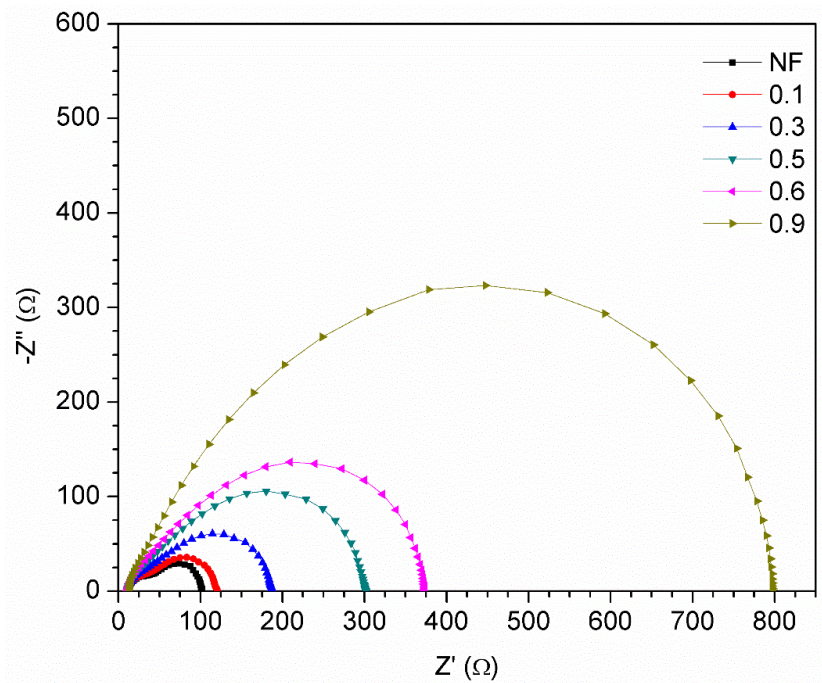Figure 48. Nyquist plots of sample 10Z measured under different light intensities.

98

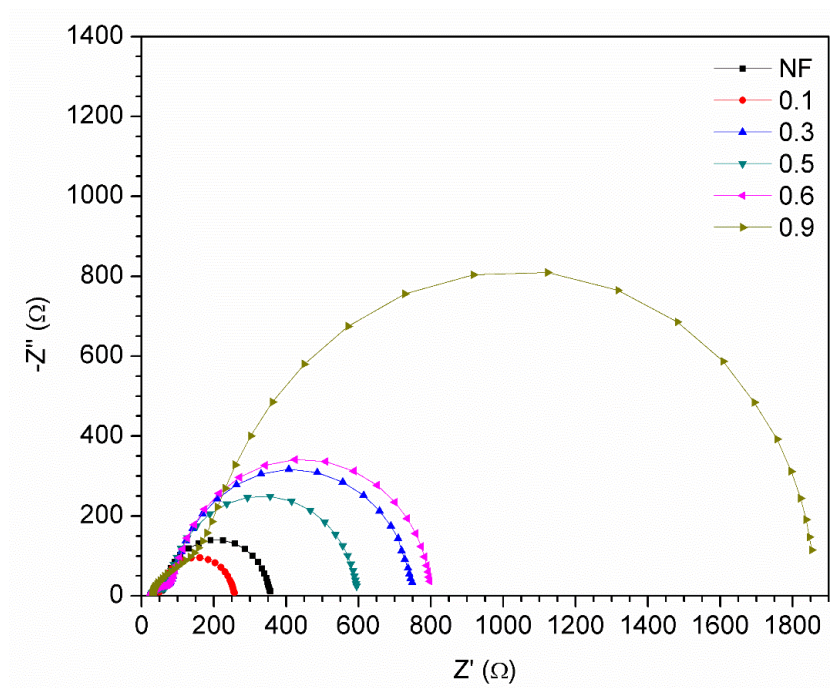Figure 49. Nyquist plots of sample 15Z measured under different light intensities.
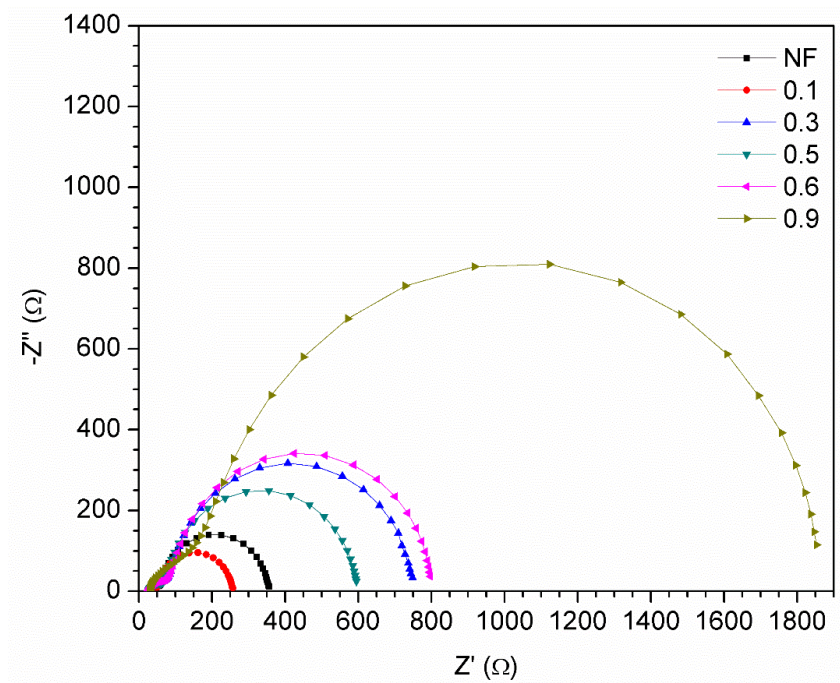

Figure 50. Nyquist plots of sample 5Z-12A measured under different light intensities.

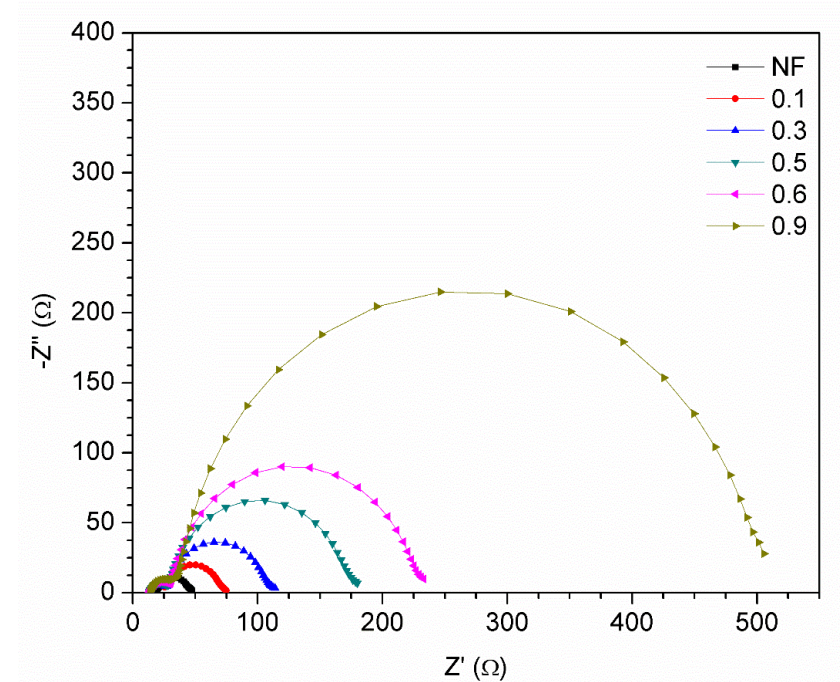Figure 51. Nyquist plots of sample 5Z-10A measured under different light intensities.

Figure 52. Nyquist plots of sample 5Z-8A measured under different light intensities.
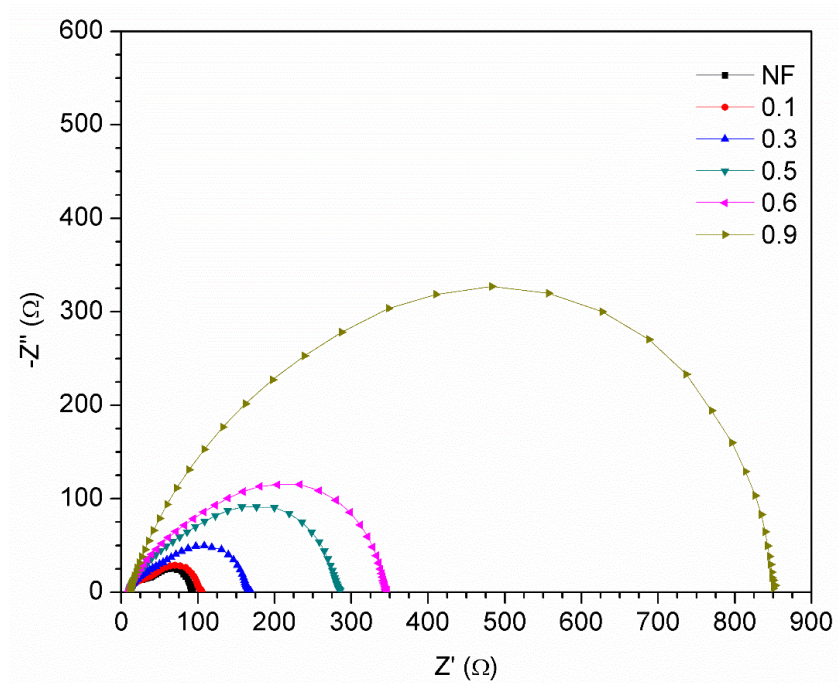
Figure 53. Nyquist plots of sample 10Z-10A measured under different light intensities.
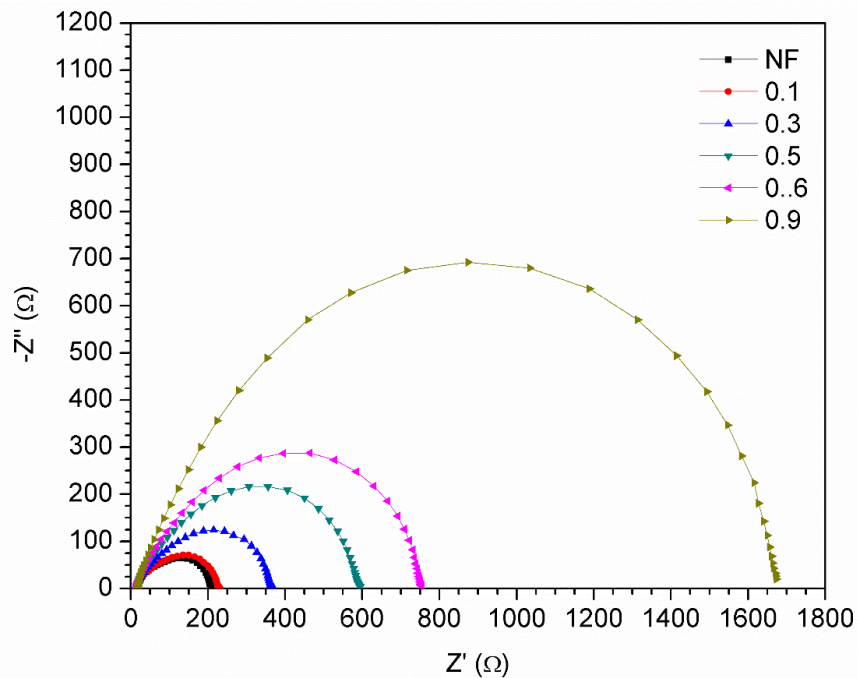

Figure 54. Nyquist plots of sample 15Z-8A measured under different light intensities.